TURUN YLIOPISTON JULKAISUJA
ANNALES UNIVERSITATIS TURKUENSIS

SARJA - SER. A I OSA - TOM. 428

ASTRONOMICA - CHEMICA - PHYSICA - MATHEMATICA

Modeling and Analysis of Noise and Interconnects for On-Chip Communication Link Design

by

Sampo Tuuna

TURUN YLIOPISTO
UNIVERSITY OF TURKU
Turku 2011

From the Department of Information Technology
University of Turku
Turku, Finland

Supervised by

Professor Jouni Isoaho
Department of Information Technology
University of Turku

and

Professor Hannu Tenhunen
Department of Information Technology
University of Turku

Reviewed by

Professor Kjell Jeppson
Department of Microtechnology and Nanoscience
Chalmers University of Technology
Göteborg, Sweden

and

Professor Etienne Sicard
Department of Electrical and Computer Engineering
National Institute for Applied Sciences (INSA)
Toulouse, France

Opponent

Distinguished Professor Eby Friedman
Department of Electrical and Computer Engineering
University of Rochester
Rochester, New York, USA

ISBN 978-951-29-4766-9 (PRINT)
ISBN 978-951-29-4767-6 (PDF)
ISSN 0082-7002
Painosalama Oy – Turku, Finland 2011

Abstract

This thesis considers modeling and analysis of noise and interconnects in on-chip communication. Besides transistor count and speed, the capabilities of a modern design are often limited by on-chip communication links. These links typically consist of multiple interconnects that run parallel to each other for long distances between functional or memory blocks. Due to the scaling of technology, the interconnects have considerable electrical parasitics that affect their performance, power dissipation and signal integrity. Furthermore, because of electromagnetic coupling, the interconnects in the link need to be considered as an interacting group instead of as isolated signal paths. There is a need for accurate and computationally effective models in the early stages of the chip design process to assess or optimize issues affecting these interconnects. For this purpose, a set of analytical models is developed for on-chip data links in this thesis.

First, a model is proposed for modeling crosstalk and intersymbol interference. The model takes into account the effects of inductance, initial states and bit sequences. Intersymbol interference is shown to affect crosstalk voltage and propagation delay depending on bus throughput and the amount of inductance.

Next, a model is proposed for the switching current of a coupled bus. The model is combined with an existing model to evaluate power supply noise. The model is then applied to reduce both functional crosstalk and power supply noise caused by a bus as a trade-off with time. The proposed reduction method is shown to be effective in reducing long-range crosstalk noise.

The effects of process variation on encoded signaling are then modeled. In encoded signaling, the input signals to a bus are encoded using additional signaling circuitry. The proposed model includes variation in both the signaling circuitry and in the wires to calculate the total delay variation of a bus. The model is applied to study level-encoded dual-rail and 1-of-4 signaling.

In addition to regular voltage-mode and encoded voltage-mode signaling, current-mode signaling is a promising technique for global communication. A model for energy dissipation in RLC current-mode signaling is proposed in the thesis. The energy is derived separately for the driver, wire and receiver termination. The location where the energy is dissipated in current-mode signaling is shown to vary as a function of wire width. All proposed models in the thesis include inductive effects and they are verified with SPICE simulations.

Acknowledgements

This work was carried out at the Department of Information Technology, University of Turku. I want to express my sincere gratitude to the individuals and institutions who have supported and enabled the research in this doctoral thesis. First and foremost, I am grateful to my supervisor, Professor Jouni Isoaho, for his continuous support and encouragement during the work leading to this thesis. I am also grateful to Professor Hannu Tenhunen for his support and many helpful discussions. I also wish to thank Professor Kjell Jeppson and Professor Etienne Sicard for their time and effort in reviewing this thesis.

I also appreciate the good company of the people at the Department of Information Technology. Especially, I want to acknowledge all the current and former fellow doctoral students with whom I shared many interesting discussions relating to science and other topics as well.

I am grateful to everyone who have co-authored papers with me. In particular, I wish to thank D. Sc. Ethiopia Nigussie for fruitful co-operation.

I gratefully acknowledge the funding from the Graduate School in Electronics, Telecommunications and Automation (GETA) and the Academy of Finland research project. In addition, I wish to express my gratitude to the Nokia Foundation for their financial support.

Turku, September 2011

Sampo Tuuna

Contents

1 Introduction **7**
1.1 On-Chip Global Communication 8
1.2 Major On-Chip Noise Sources 10
1.3 Thesis Objectives 11
1.4 Thesis Organization and Contribution 12

2 On-Chip Interconnect Modeling Methods **13**
2.1 Interconnect Approximations in Physical Design 14
2.2 Model Order Reduction 15
2.3 Decoupling Method 16
2.4 Driver Modeling 20

3 Modeling of Crosstalk and Intersymbol Interference **23**
3.1 Noise Model Derivation 24
3.1.1 Determination of Maximum Noise and Propagation Delay 28
3.2 Model Verification 30
3.3 Case Study 36
3.3.1 Switching Patterns 36
3.3.2 Signal Phases and Rise Time 38
3.3.3 Intersymbol Interference 39
3.3.4 Implications of the Case Study 40
3.4 Chapter Summary 42

4 Modeling of Switching Current and Its Impact on Power Grid Noise **43**
4.1 Modeling of Bus Switching Current 44
4.2 Modeling of Power Supply Network 47
4.3 Verification 48
4.4 Noise Reduction by Skewing 51
4.5 Chapter Summary 51

5 Reduction of Functional Crosstalk and Power Supply Noise **53**
5.1 Reduction of Crosstalk and Power Supply Noise 54
5.2 Bus and Power Supply Noise Modeling 55

5.2.1 Crosstalk Noise and Delay under Bus Skewing 55
5.2.2 Power Supply Noise under Bus Skewing 58
5.3 Model Verification 58
5.4 Case Study and Implementation 59
5.4.1 Reduction of Inductive Crosstalk Noise 59
5.4.2 Reduction of Power Supply Noise using Different Methods 61
5.4.3 Implementation and Reduction of Crosstalk using Different Methods 62
5.4.4 Influence of the Number of Skewing Times 66
5.5 Chapter Summary 68

6 Modeling of Process Variation Effects in Encoded Signaling 71
6.1 Bus Model 72
6.2 Signaling Techniques 75
6.3 Verification and Case Study 77
6.4 Chapter Summary 82

7 Energy Modeling in RLC Current-Mode Signaling 85
7.1 Current-Mode Driving Point Impedance 86
7.2 Modeling of Energy Dissipation 88
7.3 Verification 91
7.3.1 Single-Ended Current-Mode Signaling 91
7.3.2 Differential Current-Mode Signaling 94
7.4 Case Study 94
7.5 Chapter Summary 98

8 Conclusions 99

Bibliography 101

Appendices 115

A Coefficients for Equations in Chapter 3 115

B Coefficients for Equations in Chapter 4 118

Chapter 1

Introduction

Due to continuous advances in technology scaling, modern integrated circuits consist of billions of transistors [1]. Traditionally, the operating speed of an integrated circuit had been assumed proportional to the speed of a logic gate. The interconnects between the gates were considered as ideal conductors that propagated signals instantaneously and had little effect on circuit operation. Such approximations are however no longer adequate, since the physical dimensions of interconnects have been greatly reduced while the operating speeds have increased. For example, in a modern 32 nm technology [2] the width and thickness of local wires are measured in only tens of nanometers, while the clock frequency is in the range of several GHz. Due to this scaling, the performance of interconnects is increasingly affected by their electrical parasitics, i.e. resistance, capacitance and inductance. These parasitics may result in long propagation delays for signals traveling on interconnects or in signals that have been distorted by noise. The transmission of such a signal requires charging or discharging the wire capacitances which in turn consumes energy. This energy dissipated in the interconnect structure is projected to grow dramatically due to higher frequencies and increases in the number of metal layers [3]. For example, in [4] over 50% of the dynamic power consumption of a microprocessor was determined to be consumed by interconnects. In addition to transmitting data signals, on-chip wires are also used to distribute an operating voltage and the clock signal. The wires need to provide a constant operating voltage across the chip despite the increasing switching speeds and device count. The design of digital systems is further complicated by the fact that both wires and devices also suffer from process variations, i.e. their manufactured properties differ from the ideal designed values. Overall, due to these growing delay, signal integrity and energy issues in interconnects, there has been a shift of focus from devices to wires, or from computation to communication. This has resulted in a need for novel design tools and models that can be used to analyze and optimize on-chip interconnects.

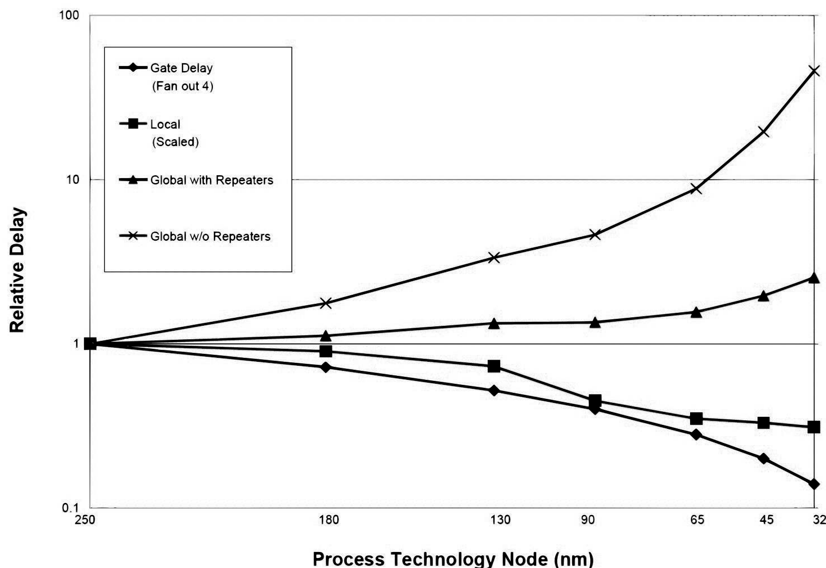

Figure 1.1: Delay for local (Metal 1) and global wiring versus feature size [3].

1.1 On-Chip Global Communication

The interconnects in an integrated circuit can be loosely divided into local, intermediate and global interconnects depending on their length, size and metal layer. An integrated circuit today often contains several large intellectual property (IP) blocks, such as memory, processing elements and interfaces. These IP blocks need to communicate with each other over long distances and they are linked by wide global interconnects that span at least one block or at most the length of the chip edge. While these global interconnects are routed in the top metal layers, the lower metal layers in turn are used by local narrow interconnects that connect neighboring gates.

The aforementioned scaling issues do not affect all interconnect types in an equal manner, as illustrated in Fig. 1.1. Unlike gate delays which are reduced as their dimensions become smaller, the delay of a fixed-length wire increases when its dimensions are scaled [5]. For local wires this delay increase is alleviated by the fact that their length is reduced with scaling since they need to connect nearby gates whose sizes diminish with scaling. However, the length of global wires is not scaled with technology since they may need to run across the chip. This has resulted in a growing delay gap between gates and global interconnects. Despite such efforts as increased aspect ratios, low-resistivity wire materials like copper, and low-κ (permittivity) dielectric, global signaling often remains a major bottleneck in modern integrated circuits.

In order to provide a high bandwidth, on-chip communication links are normally constructed of multiple wires. Among common communication architec-

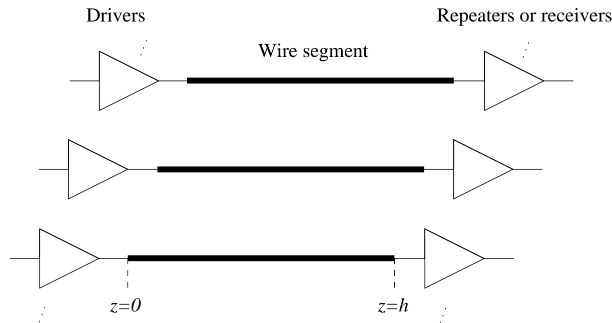

Figure 1.2: An on-chip communication link consisting of multiple parallel wires.

tures are point-to-point links, buses and a network-on-chip (NoC) [6, 7, 8]. In practice, buses are often implemented using techniques such as bus splitting [9] to reduce the total wire load. NoC links on the other hand are typically modular and structured interconnects running between routers. In addition, because of delay and signal integrity issues interconnects are commonly broken with repeaters [10] into segments. Therefore, in the physical level the communication often reduces to multiple wires running in parallel. In this thesis, the focus is on long, multiple parallel wires that typically form a part of a communication link as depicted in Fig. 1.2.

A common way to implement a long on-chip communication link is by using voltage-mode signaling with buffering. The delay of an RC interconnect increases quadratically with length since both resistance and capacitance increase linearly with wire length. The basic principle behind buffering is to reduce this delay increase to linear by inserting repeaters along the wire. The total delay then becomes equal to the number of wire segments multiplied by the individual segment delay. In addition to delay reduction, buffering can be used to reduce noise. In order to achieve the desired objective, the repeaters need to be both spaced and sized appropriately.

In addition to the common voltage mode signaling, other signaling techniques for global on-chip communication have also been proposed. These include e.g. encoded, current-mode, and differential signaling. The objective is typically to enhance signaling speed, power dissipation, signal integrity or a combination of these. Bus encoding uses additional bus wires and encoding and decoding logic to alter the signals to be transmitted on a bus. The encoding is used to avoid certain bit patterns that would result in high noise, delay or power. On the other hand, in differential signaling, a signal is transmitted over a pair of wires where the second wire is carrying the complement of the original signal. A differential signal acts as its own receiver reference and offers improved noise immunity by rejecting common mode noise. The signal swing is also effectively doubled, thus increasing noise margins and improving speed as the rise and fall times at the receiver are reduced [11]. In voltage-mode signaling, the interconnects need to be fully charged to propagate a signal. This is avoided in current-mode

signaling, where the interconnects are terminated with a resistor. Because of the resistive termination, there is a current flow that the receiver detects to determine the transmitted logic value. It has been shown that for high data rates current sensing can be very speed and power efficient in comparison to voltage sensing [12]. In addition to the above-mentioned signaling techniques addressed in this thesis, there are also emerging on-chip interconnect paradigms such as carbon nanotubes [13, 14], optical [15] and RF communications [16]. These interconnects however have several issues that need to be resolved before they can be used in on-chip communication, and they are not evaluated in this thesis.

1.2 Major On-Chip Noise Sources

Noise can be defined as the deviation of a signal from its intended or ideal value. In digital systems, most noise is generated by the system itself [11]. Crosstalk is noise that is caused by one signal interfering with another signal. The interference is caused by unwanted coupling between a wire and its neighbor. In integrated circuits, this coupling can be both capacitive and inductive. Mutual capacitance is the coupling of two or more conductors via an electric field between them, while mutual inductance is coupling by means of a magnetic field. A change in the voltage on one wire will inject a current onto another coupled wire. The affected wire is often referred to as the victim, while the switching wire is referred to as an aggressor. The induced current for capacitive and inductive coupling is proportional to the rate of change of the aggressor voltage. This effect increases the importance of crosstalk as the operating speed of circuits increases. Additionally, the scaling of technology increases the significance of coupling capacitance since wire height is not scaled as much as the distance between the wires. The adverse effects of crosstalk include increased delay and delay variation, voltage peaks on quiet wires and increased energy dissipation due to coupling capacitance. Signals may also be affected by intersymbol interference. Unlike crosstalk, where the source of interference is a signal traveling on another wire, intersymbol interference is caused by successive signals. A signal can be distorted if the wire does not reach steady state between transitions.

Another major issue in nanoscale integrated circuits is process variation. Deviations in wire and device parameters affect issues such as timing, signal integrity and performance [17, 18, 19]. For future technology nodes, a similar or larger amount of process variation is expected. Also, in addition to the amount of variations, the sensitivity of transistor performance on process variations becomes more significant in the nanometer regime [20]. Traditionally, process variation has been taken into account by using corner based analysis based on best-case, nominal, and worst-case parameters. The design is required to meet the specifications at all process corners. While this type of corner analysis has been successfully employed to model variations between dies (i.e. in inter-die variation), it is not able to accurately model variations within a single die (i.e. in intra-die variation). Using a worst-case analysis for within-die variations leads

to very pessimistic analysis results since it assumes that all devices on a die have worst-case characteristics, ignoring their inherent statistical variation [21]. To overcome these limitations, statistical methods have been proposed for parasitic extraction, static timing and signal integrity analysis.

A stable operating voltage is required by on-chip devices. Delivering and maintaining this voltage has however become increasingly difficult as the number of devices and their operating speeds have increased. The two major components of on-chip power supply noise are RI and Ldi/dt noise. The RI drop is caused by voltage losses due to the resistive component of the power distribution network, while Ldi/dt noise is caused by rapid current changes and the inductive component of the power distribution network. The amount of power supply noise is determined by the properties of the power distribution network, such as the amount of bypass capacitance and the size of power wires, and by the properties of the load current, such as its magnitude and shape.

1.3 Thesis Objectives

The aim of this thesis is to analyze and provide analytical models for on-chip communication links for use in the early stages of a design flow. While SPICE-like circuit simulators offer excellent accuracy, their computational cost is too high to be used in automated design tools for today's complex integrated circuits. Model order reduction methods [22, 23] provide a speed improvement over circuit simulators at the cost of a slightly reduced accuracy, but their computational cost is still high for the iterative optimization loops during physical design. During the physical design stages such as floorplanning and global routing, interconnect area, delay, power and noise need to be quickly estimated and optimized. For this task, another type of analytical models have been proposed [24] that provide a high simulation speed at the cost of a somewhat reduced accuracy or other limitations to their applicability. Such analytical models need to be developed for multiple issues affecting interconnects, such as crosstalk noise, process variation, and energy dissipation. Further, the models need to be developed for communication links consisting of multiple parallel wires, such as the links between routers in NoCs. Because of electromagnetic coupling, the models also need to consider the interconnects in the link as an interacting group instead of as isolated signal paths. In addition, the models need to take into account alternative signaling techniques such as encoded or current-mode signaling that are promising approaches to global communication links. Inclusion of inductance in the models is also desirable since wires in the upper metal layers are wide and they can exhibit significant inductive effects [25]. All such novel models have to be verified by a comparison to a circuit simulator. These analytical models can also be applied to case studies to rapidly evaluate the influence of different design or circuit parameters. Furthermore, reduction or optimization of issues such as noise is an application for a developed model.

1.4 Thesis Organization and Contribution

This thesis addresses signaling in long on-chip interconnects. More specifically, the focus is on multiple parallel coupled interconnects that are a commonly a part of a communication link. This structure is referred to as a bus in this thesis and several issues relating to it are addressed as described below. The models developed in this thesis are intended for the early stages of a design flow, where high speed and analytical equations are preferred in order to use the models e.g. in iterative optimization loops. All models in the thesis are derived for RLC signaling. The thesis is organized into eight chapters. In Chapter 2, an overview of different on-chip interconnect modeling methods is provided. Emphasis is given to the decoupling method that is the approach used in this thesis. In Chapter 3, an analytical model that for the first time evaluates both crosstalk and intersymbol interference in buses is proposed. The model takes into account aspects that have not been included in a single previous analytical model such as inductive coupling, phases, initial states and bit sequences. The model is then verified and applied to study crosstalk and intersymbol interference in a bus under different switching patterns and operating speeds. Intersymbol interference is shown to affect crosstalk voltage and propagation delay depending on bus throughput and the amount of inductance. In Chapter 4, a model for the switching current of a coupled on-chip bus is proposed. While models for the simultaneous switching noise of a gate with a simple capacitive load have previously been presented, the proposed model includes the effects of long coupled interconnects. This coupling is shown to affect the switching current. The influence of skewed inputs is included and the model is combined with an existing power grid model to evaluate induced power supply noise in different locations of the power grid. In Chapter 5, intentional skewing of bus inputs is used to reduce functional crosstalk noise and power supply noise. Unlike in previously existing methods, the reduction is achieved as a trade-off with time or timing slack. Models proposed in the previous chapters are used to demonstrate that the method can be used to reduce long-range inductive crosstalk. The skewing method is implemented and compared to other crosstalk and power supply reduction methods. In Chapter 6, a model for analyzing the effects of process variation on an encoded bus is proposed. The proposed model includes variation in both the signaling circuitry and in the wires to calculate the total delay variation of a bus. Characterization of encoding circuitry is used together with analytical interconnect modeling to rapidly analyze level-encoded dual-rail (LEDR) and 1-of-4 signaling. Wire width variation is demonstrated with the model to affect LEDR signaling more than 1-of-4 or regular signaling. In Chapter 7, a model for energy dissipation in RLC current-mode signaling is proposed. A realizable driving point Π model is presented for an RLC current-mode transmission line. The energy dissipation is derived separately for the driver, wire and receiver termination. The model is applied to differential current-mode signaling. The location where energy is dissipated in current-mode signaling is shown to depend on wire width. Finally, in Chapter 8, the thesis is concluded.

Chapter 2

On-Chip Interconnect Modeling Methods

In general, an interconnect behaves as a waveguide that can be analyzed using Maxwell's equations. An interconnect can also be analyzed using transmission line equations, if it is assumed that the waves on the line propagate in the transverse electromagnetic (TEM) mode [26, 27]. In TEM mode, both electric field and magnetic field vectors lie in a plane perpendicular to the axis of propagation as shown in Fig. 2.1.

Conductors that have electrically large cross-sectional dimensions have in addition to the TEM mode also other modes of propagation [28]. Also, if the conductor is lossy, i.e. it has a non-zero resistance, the assumption of solely TEM mode is invalidated since the current flowing through the conductor creates a an electric field in the direction of propagation. However, if the conductor losses are small, lossy transmission lines are still assumed to represent the situation. An inhomogeneous surrounding medium also invalidates the TEM mode assumption, because a TEM field structure must have only one velocity of wave propagation. Transmission lines can nonetheless be used assuming that the velocities are not substantially different. The usage of transmission lines to represent lossy conductors and/or conductors having an electrically large cross-section and/or inhomogeneous surrounding medium is generally referred to as the quasi-TEM assumption. In addition to transmission lines, simpler lumped segments can also be used to represent interconnects, although the accuracy may be reduced depending on wire length and signal frequency. A complete solution that does not assume a TEM mode can be obtained with so-called full-wave solutions of Maxwell's equations [29]. These solutions generally require numerical methods that are very time-consuming and therefore impractical in the design of integrated circuits. Interconnect models based on transmission lines or lumped RC or RLC segments are thus normally used in on-chip interconnect analysis.

In the following, an overview of different approaches to on-chip interconnect modeling is given. First, various approximations to interconnect structures dur-

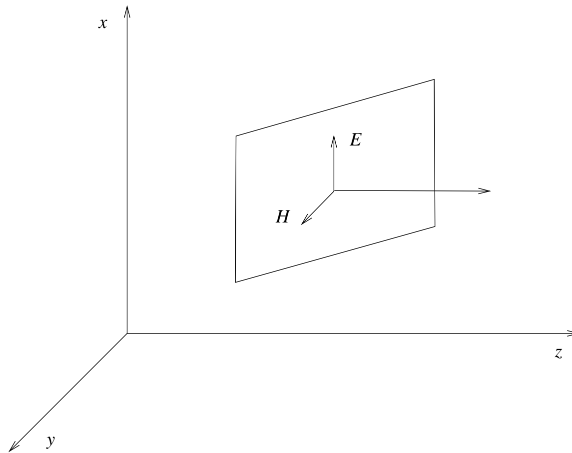

Figure 2.1: Electromagnetic field structure of TEM propagation. Electric field E and magnetic field intensity H lie in a plane perpendicular to the axis of propagation z.

ing the physical design are presented. Second, model-order reduction methods are reviewed. Third, an overview for the decoupling method that is the modeling approach taken in this thesis is presented. Finally, the characterization and modeling of drivers is also discussed.

2.1 Interconnect Approximations in Physical Design

Accurate interconnect modeling is an issue in post-layout verification, where high accuracy is needed. However, in deep-submicron design there is also a need for another class of interconnect modeling tools for the early stages of the design flow, where high simulation speed is needed for design optimization. During the physical design, interconnect area, delay, power and noise are estimated and optimized as a trade-off between different design parameters. For example, in floorplanning the major functional blocks of a chip are tentatively placed using criteria such as chip area and interconnect length. Optimizations during this process include the insertion of buffers into interconnects to reduce delay and crosstalk noise [30, 31], and reduction of peak temperatures due to interconnects [32].

Since there is little physical information available during floorplanning, the optimization possibilities are limited, and the optimization therefore continues in other design stages when more physical information is available. For example, after routing, the routes, layers and relative positions of nets are known. During global routing, where the approximate path of each net is planned, crosstalk noise reduction can be achieved with shield insertion and buffering [33]. In-

terconnect process variation such as dishing and erosion can also be reduced during global routing [34]. After routing, techniques such as buffer insertion or wire perturbation are not desirable since they may require rerouting. Instead, techniques such as gate sizing can be applied to reduce crosstalk [35] and interconnect delay [36]. Spacing of the wires can also be applied to reduce interconnect power and delay [37].

In order to achieve a high simulation speed in the iterative optimization loops during these design stages, analytical interconnect models are required. These models are often derived by employing different approximations to an interconnect topology in order to obtain a simpler circuit that is then analytically modeled. For example, in [38], two coupled RC interconnects are reduced to a lumped two-node circuit that is then analyzed for crosstalk noise. The coupling is included with a single capacitor. In [24], RC interconnects are reduced to a six-node lumped template circuit instead. In addition to the wire structure, also the input signals to the wires can be approximated. Buffering and shielding are performed in [33] based on a crosstalk metric that approximates the input signal as an infinite ramp, while in [34] delay based on a RC step response is used for global routing. Besides lumped circuits, transmission line structures can also be used as in [39] where two parallel RLC transmission lines are used to calculate crosstalk noise.

2.2 Model Order Reduction

Model order reduction algorithms provide a speed improvement over circuit simulators while preserving good accuracy, and they are useful for post-layout verification where accuracy is a key requirement [24]. In this section, the fundamentals of model order reduction of interconnects are reviewed.

Any interconnect structure consisting of resistors, capacitors and inductors is a linear time-invariant (LTI) system. Continuous-time, LTI systems are often described using a state-space realization. The state-space model of a multi-input multi-output system is

$$\begin{aligned} \tfrac{d\mathbf{x}(t)}{dt} &= \mathbf{A}\mathbf{x}(t) + \mathbf{B}\mathbf{u}(t) \\ \mathbf{y}(t) &= \mathbf{C}\mathbf{x}(t) + \mathbf{D}\mathbf{u}(t) \end{aligned} \tag{2.1}$$

where $\mathbf{x}$ is the state vector, $\mathbf{u}$ is the input vector, $\mathbf{y}$ is the output vector and $\mathbf{A}$, $\mathbf{B}$, $\mathbf{C}$ and $\mathbf{D}$ are matrices.

In linear circuit simulation Modified Nodal Analysis (MNA) [40] is widely used to form the circuit equations in the form of [41]

$$\begin{aligned} \mathbf{C}\tfrac{d\mathbf{x}(t)}{dt} &= -\mathbf{G}\mathbf{x}(t) + \mathbf{B}\mathbf{u}(t) \\ \mathbf{y}(t) &= \mathbf{L}^T\mathbf{x}(t) \end{aligned} \tag{2.2}$$

where $\mathbf{G}$ and $\mathbf{C}$ represent conductance and energy storage matrices, respectively, vector $\mathbf{x}$ includes MNA variables, and $\mathbf{B}$ and $\mathbf{L}$ are mapping matrices. Taking a Laplace transform of (2.2) gives the matrix transfer function $\mathbf{H}(s)$ as

$$\mathbf{H}(s) = \frac{\mathbf{y}(s)}{\mathbf{u}(s)} = \mathbf{L}^T(\mathbf{G} + s\mathbf{C})^{-1}\mathbf{B}. \tag{2.3}$$

The entries of $\mathbf{H}(s)$ can be shown to be in the form of rational polynomials of s

$$H_{ij}(s) = \frac{b_{ij1} + b_{ij2}s + \ldots + b_{ijm}s^m}{1 + a_1 s + \ldots + a_n s^n}. \tag{2.4}$$

For many interconnect circuits, the number of poles of $H(s)$ can be very large. Some of these poles have an insignificant contribution to circuit performance, and the circuit can be adequately described with a group of dominant poles. In model order reduction, the objective is to reduce the complexity with a lower-order state-space system while preserving, or approximating the original input-output behavior. Asymptotic Waveform Evaluation (AWE) [22] approximates the behavior of a linear circuit by generating moments, or Taylor series coefficients of $H(s)$, and matching them to form a lower order transfer function. To overcome the numerical problems of AWE, several other model order reduction methods have been presented, such as Complex Frequency Hopping (CFH) [42], Padé-via-Lanczos (PVL) [43], PRIMA [23], Truncated Balanced Realization (TBR) [44] and parameterized model order reduction [45].

Model order reduction has become an established part of interconnect analysis. It has been used e.g. for power grid verification [46], interconnect power consumption [47] and static timing analysis [48]. Model order reduction has however also some drawbacks. The efficiency of model order reduction reduces as the number of circuit input-output terminals is increased [49, 50], complicating the analysis of e.g. power distribution networks and large data buses. Many model order reduction algorithms are not adapted to handle more than a few tens of terminals [51]. Numerical problems also remain an issue in many model order reduction methods [52]. Furthermore, the generation of moments requires successive analyses of an equivalent dc circuit of an interconnect tree or the application of MNA.

2.3 Decoupling Method

The electrical properties of multiple coupled parallel wires, as in a bus, are often represented in a concise form using transmission line matrices. The capacitance matrix is defined as

$$\mathbf{C} = \begin{pmatrix} C_{11} & -C_{12} & \ldots & -C_{1n} \\ -C_{21} & C_{22} & & \\ \vdots & & \ddots & \\ -C_{n1} & & & C_{nn} \end{pmatrix}$$

where C_{nn} is the total capacitance seen by the line n and C_{mn} is the coupling capacitance between lines m and n. The inductance matrix takes the form of

$$\mathbf{L} = \begin{pmatrix} L_{11} & L_{12} & \dots & L_{1n} \\ L_{21} & L_{22} & & \\ \vdots & & \ddots & \\ L_{n1} & & & L_{nn} \end{pmatrix}$$

where L_{nn} is the self-inductance for line n and L_{mn} is the mutual inductance between lines m and n. Unlike in the capacitance matrix, L_{nn} is not the sum of the self-inductance and mutual inductance. The resistance matrix is

$$\mathbf{R} = \begin{pmatrix} R_{11} & R_{12} & \dots & R_{1n} \\ R_{21} & R_{22} & & \\ \vdots & & \ddots & \\ R_{n1} & & & R_{nn} \end{pmatrix}$$

where R_{mm} define the resistive losses of each conductor and R_{mn} are due to the current return path. For a return path with a large area, R_{mn} will be close to zero. For high frequencies, the return current will flow near the signal line to reduce the impedance of the loop and the non-diagonal terms of the resistance matrix will be non-zero [53].

The voltage and current vectors on n parallel lines can be defined as

$$\mathbf{V}(z,t) = \begin{pmatrix} V_1(z,t) \\ V_2(z,t) \\ \vdots \\ V_n(z,t) \end{pmatrix} \tag{2.5}$$

$$\mathbf{I}(z,t) = \begin{pmatrix} I_1(z,t) \\ I_2(z,t) \\ \vdots \\ I_n(z,t) \end{pmatrix} \tag{2.6}$$

where $V_i(z,t)$ is the voltage at point z of the ith transmission line and $I_i(z,t)$ is the current through parallel elements.

The transmission line equations for n lines are

$$\begin{aligned} \tfrac{\partial}{\partial z}\mathbf{V}(z,t) &= -\mathbf{R}\mathbf{I}(z,t) - \mathbf{L}\tfrac{\partial}{\partial t}\mathbf{I}(z,t) \\ \tfrac{\partial}{\partial z}\mathbf{I}(z,t) &= -\mathbf{G}\mathbf{V}(z,t) - \mathbf{C}\tfrac{\partial}{\partial t}\mathbf{V}(z,t). \end{aligned} \tag{2.7}$$

The problem of solving multiple coupled lines can be reduced to solving a number of equations for isolated lines by using a matrix transformation. The coupling represented by non-diagonal elements can be eliminated by diagonalizing the transmission line matrices. This can be achieved by using a congruence

transformation [54] or by using a similarity transformation with improved efficiency and numerical stability [55]. The similarity transformation of matrix $\mathbf{A}$ to matrix $\mathbf{\Lambda}$ is

$$\mathbf{M}^{-1}\mathbf{A}\mathbf{M} = \mathbf{\Lambda}. \tag{2.8}$$

If the $n \times n$ matrix $\mathbf{A}$ has n linearly independent eigenvectors, $\mathbf{\Lambda}$ is a diagonal matrix whose entries are the eigenvalues of $\mathbf{A}$ [56]. $\mathbf{M}$ is a square matrix whose n columns are the eigenvectors of $\mathbf{A}$.

In the decoupling method the mode voltages and currents $\mathbf{V}_m$ and $\mathbf{I}_m$ are defined as

$$\mathbf{V}(z,t) = \mathbf{M}_V \mathbf{V}_m(z,t) \tag{2.9}$$

and

$$\mathbf{I}(z,t) = \mathbf{M}_I \mathbf{I}_m(z,t) \tag{2.10}$$

where $\mathbf{M}_V$ and $\mathbf{M}_I$ are $n \times n$ transformation matrices. $\mathbf{L}$ and $\mathbf{C}$ are diagonalizable since they are real, symmetric and positive definite [26]. The diagonalized inductance and capacitance matrices $\hat{\mathbf{L}}$ and $\hat{\mathbf{C}}$ are

$$\hat{\mathbf{L}} = \mathbf{M}_V^{-1}\mathbf{L}\mathbf{M}_I \tag{2.11}$$

$$\hat{\mathbf{C}} = \mathbf{M}_I^{-1}\mathbf{C}\mathbf{M}_V. \tag{2.12}$$

In Fig. 2.2 is shown a typical cross-section of a microprocessor with wire and dielectric layers. Of the global layers, the topmost one is normally used for power distribution, while the others are used for global signaling. The surrounding of these wires has the same relative permittivity, except for the vias and the thin etch stop and dielectric capping layers. The surrounding dielectric is therefore approximated as homogeneous, in which case [26]

$$\mathbf{M}_I = \mathbf{M} \tag{2.13}$$

$$\mathbf{M}_V = \mathbf{M} \tag{2.14}$$

$$\mathbf{M}_V^{-1} = \mathbf{M}_I^{-1} = \mathbf{M}^T \tag{2.15}$$

where T denotes a transpose. If the relative permittivity is not constant, as in the case of an inhomogeneous embedded low-κ dielectric, an effective relative permittivity can be used instead. The effective relative permittivity is determined so that if the inhomogeneous surrounding medium were replaced by a homogeneous medium having an effective relative relativity none of the properties of the line would be changed [57]. The diagonalized inductance and capacitance matrices are then

$$\hat{\mathbf{L}} = \mathbf{M}^T\mathbf{L}\mathbf{M} \tag{2.16}$$

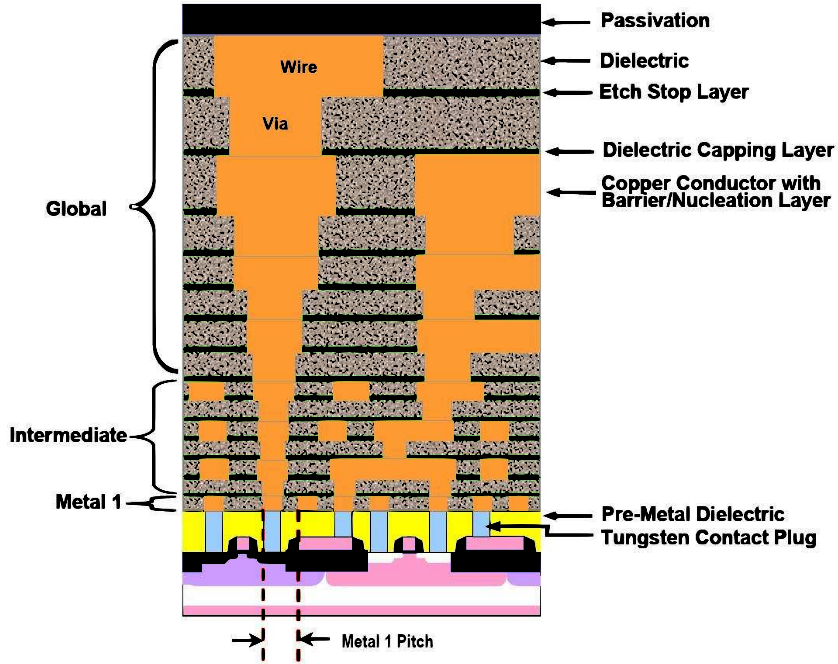

Figure 2.2: Typical cross-section of a microprocessor [3].

$$\hat{\mathbf{C}} = \mathbf{M}^T\mathbf{C}\mathbf{M}. \tag{2.17}$$

Assuming lines with same source and load impedance, and per-unit-length resistance, the boundary conditions can be included as [58]

$$\hat{\mathbf{R}}_S = \mathbf{R}_S \tag{2.18}$$

$$\hat{\mathbf{C}}_L = \mathbf{C}_L \tag{2.19}$$

$$\hat{\mathbf{V}}_S = \mathbf{M}\mathbf{V}_S \tag{2.20}$$

where R_S is the driver source resistance, C_L is the receiver load capacitance and V_S is the driver voltage source. The resistance matrix is assumed to be diagonal in the first place, i.e.

$$\hat{\mathbf{R}} = \mathbf{R}. \tag{2.21}$$

The calculated responses of the decoupled lines can then be combined into the response of the coupled system using (2.13) and (2.14).

Decoupling method, or modal analysis, has been used in different variations in recent years for on-chip interconnect analysis, e.g. for analysis of periodic signals [59], modeling of multi-walled carbon nanotubes [60] and signal integrity

verification of inductively dominated lines [61]. The method is chosen as the modeling approach taken in this thesis since it is applicable to more wires and more complex interconnect topologies than straightforward template circuits. There is also a trend towards network-on-chip architectures with structured parallel links between routers that are suitable for modeling with the decoupling method. The method also enables analytical models and requires no moment generation and is therefore suitable for analysis early in the design flow.

2.4 Driver Modeling

In addition to modeling the wires themselves, it is necessary to include the influence of the gates driving the wires. Common approaches to including these nonlinear devices in the interconnect models are described in this section.

The first gate models characterized the gate simply as a fixed delay. Later single-parameter models obtained this delay based on the capacitive load driven by the gate. Then, because of technology scaling, it became necessary to record also the rise time or slew of the gate output in addition to the gate delay. This data was needed to accurately model gate properties since the rise time of a gate input signal and the gate load determine the gate delay and output rise time. These two-parameter gate models represent the gate delay and output rise time as a function of input rise time and output load capacitance. The characterization of a gate where these parameters are collected is performed using a circuit simulator such as SPICE. The characterization data can be stored in a look-up table or more compactly in the form of k-factor equations fitted to the characterization data [62].

The concept of effective capacitance was introduced in [63] since a driver sees only a part of the total interconnect capacitance due to resistive shielding. The connection between the driver and the interconnect is gained iteratively by calculating the effective capacitance and then applying the two-parameter model to obtain the gate delay and output slew. The effective capacitance is calculated by equating the mean current into an interconnect with the mean current into a single capacitor.

To capture the combined effect of a gate and an interconnect, switch-resistor models can also be used. The switch-resistor model consists of a voltage source and a linear resistor that represent a gate. The connection between the driver and the interconnect is easily modeled by including the driver resistance in the interconnect RLC circuit. Although this facilitates the analysis of the combined gate and interconnect, the accuracy is limited by the need to map a gate on-resistance to a linear resistor.

In order to improve model accuracy, extensions of the two-parameter models have been proposed. A two-ramp model based on two effective capacitances was proposed in [64], while in [65] the effective capacitance was matched for both 50% delay and 80% transition time. Also, models that store the gate output waveform have been adopted. For example, the effective current source model (ECSM) by Cadence stores the driving point voltage waveforms of each

input slew and load capacitance combination, while the composite current source (CCS) model by Synopsys stores the characterization data as currents.

Recently, current-source models (CSM) have been proposed [66, 67, 68] to further improve accuracy by addressing issues such as complex interconnect loads and non-linear input waveforms. These models are based on a nonlinear voltage-controlled current source that approximates the current drawn by a gate for a certain value of input voltage, time, output voltage, etc [69]. A CSM is a major departure from the previous models, since to determine delay and slew (or voltage response) a circuit simulation must be performed. Instead of propagating only the delay and slew, CSM propagates the whole voltage waveform. The high accuracy of CSMs makes them attractive for employment inside a sign-off timing analysis tool [70].

Chapter 3

Modeling of Crosstalk and Intersymbol Interference

A major source of on-chip noise is crosstalk, which is caused by capacitive and inductive coupling between wires. Crosstalk noise avoidance is especially important for on-chip buses, since in buses several interconnects run parallel to each other for long distances. Signals traveling on buses may also corrupt later ones if the bus does not reach steady state between signals. This intersymbol interference is caused by stored energy in reflections, circuit ringing and charge storage [11]. Ringing and temporary charge storage in interconnects are problematic in buses, where interconnects are wide resulting in a large capacitive load and inductive noise. The amount of crosstalk noise and intersymbol interference depends not only on the electrical properties of interconnects, but also on the signal transitions. Capacitive coupling causes an increase in propagation delay when coupled interconnects are switching in the opposite direction, and a decrease when they are switching in the same direction. Also the induced crosstalk voltage on a quiet interconnect depends on the transition activity of neighboring interconnects. Intersymbol interference, on the other hand, is dependent on successive transitions. Certain bit sequences can cause an interconnect not to reach steady state. Signals may also arrive at different phases due to unbalanced signal paths, or because of deliberate timing intervals to reduce crosstalk noise or peak current draw [71]. The relative input timing of aggressor and victim nets influences strongly the coupling noise on a victim net [72, 73].

Over the last decade several analytical models have been proposed for the estimation of crosstalk noise in coupled interconnects. In [74] a model for up to five coupled lines has been presented. However, the model is based on a single L-segment and does not consider inductance. In [75, 76] a Π-model is used, but inductance is neglected. A model for a bus consisting of distributed RC lines has been suggested in [77], but signal rise times and inductance are not included. It has also been assumed that every other wire in the bus carries the same signal. A propagation delay model for a bus has been presented in [78],

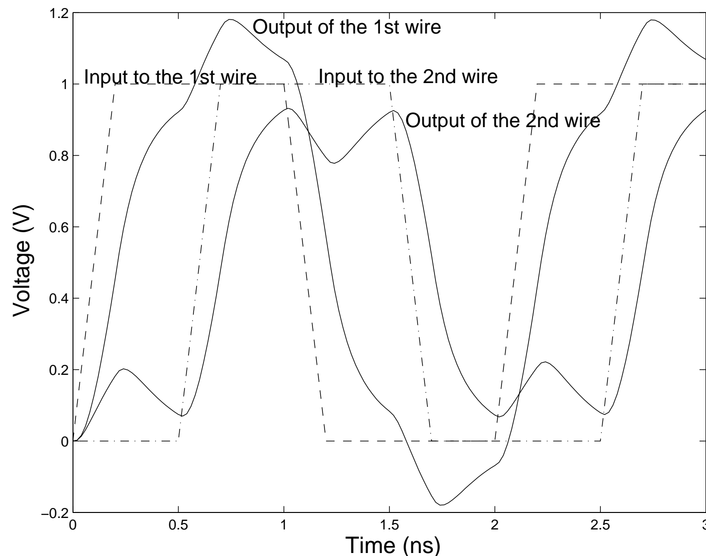

Figure 3.1: Two coupled 2 mm long interconnects with initial states.

but the model does not consider inductance and is also based on switch factor analysis. In [79] a model for two distributed RLC wires has been presented, but inductive coupling has been ignored. It has been shown that the effects of inductive coupling can be significant for long interconnects [80]. The accuracy of RC models in crosstalk evaluation is also no longer sufficient for deep sub-micron circuits [81].

None of the mentioned models take into account both crosstalk and intersymbol interference. In this chapter, an analytical RLC Π-model for crosstalk and intersymbol interference is proposed [82]. The model includes different phases, signal rise times, initial conditions and bit sequences. The model also considers both capacitive and inductive coupling between interconnects.

3.1 Noise Model Derivation

The input and output voltages of two coupled interconnects are represented in Fig. 3.1 to demonstrate the impact of intersymbol interference. Initially both wires are at quiescent state. In this case the 50% propagation delay of the first wire is 112 ps. However, when the wire switches up the second time, it has not reached steady state, and the delay is increased to 120 ps. Additionally, in the first upwards transition, the crosstalk noise peak on the other line is 202 mV. Because of the initial state, the second noise peak, at about 2.2 ns, reaches 222 mV. The differences in percentage points are 7.1 % and 9.9 %, respectively.

For any lumped linear time-invariant (LTI) circuit its output can be written in the following form [83]

$$Y(s) = \sum_{m=1}^{M} H_{em}(s) X_m(s) + \sum_{n=1}^{N} H_{in}(s) \frac{\lambda_n(0)}{s} \tag{3.1}$$

where $Y(s)$ is the Laplace transform of the circuit output, $X_m(s)$ is the Laplace transform of the mth independent external voltage or current source, M is the number of external sources, $\frac{\lambda_n(0)}{s}$ is the Laplace transform of the source describing the effect of the value $\lambda_n(0)$ of the nth state variable at $t = 0$, N is the order of the system and $H_{em}(s)$ and $H_{in}(s)$ are functions that relate each external source or initial condition source to the output. If it is assumed that the circuit is initially in quiescent state, the transfer function $H_{em}(s)$ relates the output to the input. In the modeling of crosstalk the initial state of the interconnects is generally ignored to enable the usage of transfer function and thus facilitate the calculations.

In the following an analytical model for a coupled bus including the initial conditions is derived. The bus is assumed to consist of interconnects that have the same per-unit-length resistance. The spacing between interconnects does not need to be uniform. The receivers are assumed to have the same load capacitance. The source resistances of the drivers need to be similar. However, the driver rise times can be different. This makes it possible to model the influence of different driver resistances, since from the perspective of a downstream wire, a slow input driven into a source resistor is almost indistinguishable from a fast input driven into a larger source resistor [5]. For example, with suitably selected rise times the aggressor driver resistance can increased while the victim resistance is maintained. To obtain a closed-form time-domain solution and include initial states in the model, the interconnect is modeled as a Π-segment.

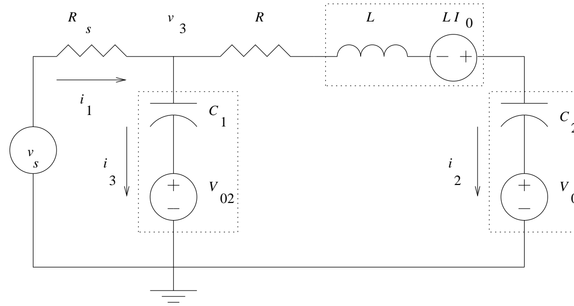

Figure 3.2: Equivalent circuit for an interconnect considering initial conditions.

The driver is modeled as a linear voltage source with source resistance R_s. The receiver is modeled as a capacitive load. In Fig. 3.2, R and L are the total resistance and inductance of the interconnect while C_1 is half of the total capacitance of the interconnect and C_2 is the sum of the receiver capacitance and half of the total interconnect capacitance. The possible initial charges in the capacitors and the initial current in the inductor are included in the model by

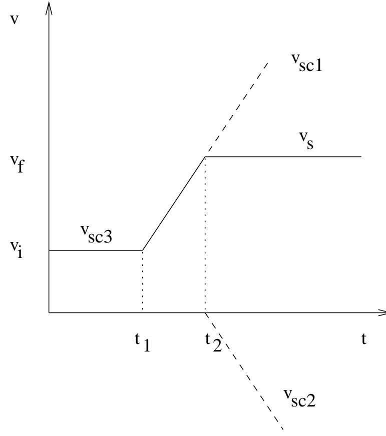

Figure 3.3: The voltage source v_s and its components.

using their s-domain equivalent circuits, which have been marked in the figure with dotted lines. The voltage source v_s is modeled as a superposition of three components v_{sc1}, v_{sc2} and v_{sc3} as shown in Fig. 3.3. The components are used to obtain different input phases for interconnects as well as an input signal with a non-zero rise time.

The equations for the components of the voltage source can be written as

$$v_{sc1}(t) = \left[\frac{v_f - v_i}{t_2 - t_1}(t - t_1) + v_i\right] u(t - t_1) \tag{3.2}$$

$$v_{sc2}(t) = \left[-\frac{v_f - v_i}{t_2 - t_1}(t - t_2)\right] u(t - t_2) \tag{3.3}$$

$$v_{sc3}(t) = v_i \left[u(t) - u(t - t_1)\right] \tag{3.4}$$

where $t_2 - t_1$ is the rise time and v_i and v_f are the initial and final values of the input signal. t_1 is the phase of the input signal and $u(t)$ is the unit step function. The response of the circuit in Fig. 3.2 to the voltage source v_s can be solved with the following s-domain nodal equations.

$$V_s - I_1 R_s - \frac{I_3}{sC_1} - \frac{V_{02}}{s} = 0 \tag{3.5}$$

$$\frac{I_3}{sC_1} + \frac{V_{02}}{s} - I_2 R - sLI_2 + LI_0 - \frac{I_2}{sC_2} - \frac{V_0}{s} = 0 \tag{3.6}$$

$$I_1 = I_2 + I_3 \tag{3.7}$$

In the equations above V_0 is the initial voltage at the end of the line and V_{02} is the initial voltage of capacitor C_1. I_0 is the initial current flowing through the inductor. The equations can be used to derive an expression for current I_2. The voltage source components in s-domain are

$$V_{sc1} = \left(\frac{k}{s^2} + \frac{v_i}{s} \right) e^{-t_1 s} \tag{3.8}$$

$$V_{sc2} = -\frac{k}{s^2} e^{-t_2 s} \tag{3.9}$$

$$V_{sc3} = v_i \left(\frac{1}{s} - \frac{1}{s} e^{-t_1 s} \right) \tag{3.10}$$

where

$$k = \frac{v_f - v_i}{t_2 - t_1}. \tag{3.11}$$

By substituting them into the expression for I_2 and using partial fractions and inverse Laplace transform the time-domain equation for the current $\hat{i}_2$ of a decoupled line can be written as

$$\begin{aligned} \hat{i}_2(t) = & \left[a_1 e^{s_1 t} + a_2 e^{s_2 t} + a_3 e^{s_3 t} \right] u(t) \\ & + \Big[a_4 + a_5 e^{s_1 (t - t_1)} + a_6 e^{s_2 (t - t_1)} \\ & + a_7 e^{s_3 (t - t_1)} \Big] u(t - t_1) \\ & + \Big[a_8 + a_9 e^{s_1 (t - t_2)} + a_{10} e^{s_2 (t - t_2)} \\ & + a_{11} e^{s_3 (t - t_2)} \Big] u(t - t_2) \ . \end{aligned} \tag{3.12}$$

The voltage $\hat{v}_3(t)$ can be obtained in a similar manner and written as

$$\begin{aligned} \hat{v}_3(t) = & \hat{i}_2(t) R + \hat{v}_{out}(t) \\ & + \left[b_1 e^{s_1 t} + b_2 e^{s_2 t} + b_3 e^{s_3 t} \right] u(t) \\ & + \Big[b_4 e^{s_1 (t - t_1)} + b_5 e^{s_2 (t - t_1)} \\ & + b_6 e^{s_3 (t - t_1)} \Big] u(t - t_1) + \Big[b_7 e^{s_1 (t - t_2)} \\ & + b_8 e^{s_2 (t - t_2)} + b_9 e^{s_3 (t - t_2)} \Big] u(t - t_2) \end{aligned} \tag{3.13}$$

where $\hat{v}_{out}(t)$ is the response of the decoupled line to input v_s. It can be written as

$$\begin{aligned} \hat{v}_{out}(t) = & V_0 + \left[c_1 + c_2 e^{s_1 t} + c_3 e^{s_2 t} + c_4 e^{s_3 t} \right] u(t) \\ & + \left[c_5 + c_6 (t - t_1) + c_7 e^{s_1 (t - t_1)} \right. \\ & \left. + c_8 e^{s_2 (t - t_1)} + c_9 e^{s_3 (t - t_1)} \right] u(t - t_1) \\ & + \left[c_{10} + c_{11} (t - t_2) + c_{12} e^{s_1 (t - t_2)} \right. \\ & \left. + c_{13} e^{s_2 (t - t_2)} + c_{14} e^{s_3 (t - t_2)} \right] u(t - t_2) \ . \end{aligned} \tag{3.14}$$

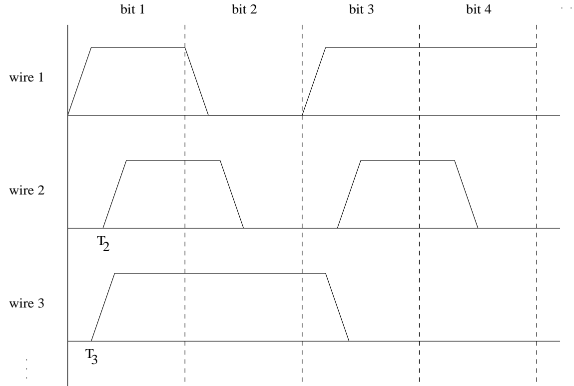

Figure 3.4: Use of bit sequences and phases in the model.

The expressions a_i, b_i and c_i are composed of the variables that are obtained from (3.5)-(3.7) during the derivation, and they are presented in the Appendix. Eq. (3.12)-(3.14) are the response of a decoupled interconnect to a single voltage source v_s. The total response of the decoupled interconnect is calculated using superposition since its input $\hat{v}_{si}$ is a combination of the original voltage sources $v_{s1}, \ldots, v_{sn}$, as shown in (2.20). The voltages $v_3(t)$ and $v_{out}(t)$ and current $i_2(t)$ of a coupled interconnect can then be calculated by using (2.9) and (2.10), respectively.

To model bit sequences, the state of each coupled wire at the end of a clock cycle is passed onto the next calculation by setting the final values of $v_{out}(t)$, $i_2(t)$ and $v_3(t)$ of an interconnect as its initial values V_0, I_0 and V_{02}, respectively. A voltage different from zero (or V_{dd}) or a non-zero current in these variables also indicates the presence of intersymbol interference. The usage of bit sequences is demonstrated in Fig. 3.4, where solid lines represent input signals $v_{s1}, \ldots, v_{sn}$ to the wires. The wire that is switching the earliest is used as a reference wire that determines the start and end of bits. In Fig. 3.4, wire 1 is the reference wire and T_2 and T_3 are the phases of wires 2 and 3, respectively. The dotted lines in the figure mark the instant when the final values of $v_{out}(t)$, $i_2(t)$ and $v_3(t)$ are evaluated. Two successive similar input bits are obtained by setting the initial voltage v_i and final voltage v_f equal to each other.

3.1.1 Determination of Maximum Noise and Propagation Delay

The resulting voltage waveforms can have multiple peaks at various times because of inductive ringing and different phases. This complicates the task for finding the maximum induced crosstalk noise, since there can be several local maxima in the voltage waveform. The global maximum must also be discovered in as few iterations as possible to obtain a necessary efficiency for VLSI design tools. It is not possible to construct an algorithm that will find the global max-

imum for an arbitrary function, but in this case the physical properties of the system can be analyzed to alleviate the task. The noise peak on a victim occurs approximately at the same time as the aggressor voltage reaches maximum. A method to evaluate the propagation delay t_{pd} of a single RLC line has been proposed in [84]. The propagation delay t_{pd} can be written as

$$t_{pd} = \frac{e^{-2.9\zeta^{1.35}}}{\omega_n} + 0.74R_tC_t(R_T + C_T + R_TC_T + 0.5) \tag{3.15}$$

where

$$\zeta = \frac{R_t}{2}\sqrt{\frac{C_t}{L_t}}\frac{R_T + C_T + R_TC_T + 0.5}{\sqrt{1 + C_T}} \tag{3.16}$$

$$\omega_n = \frac{1}{\sqrt{L_t(C_t + C_{load})}} \tag{3.17}$$

$$R_T = \frac{R_s}{R_t} \tag{3.18}$$

$$C_T = \frac{C_{load}}{C_t} \tag{3.19}$$

and where R_t, L_t and C_t are the total resistance, inductance and capacitance, respectively. The time t_{pd} is not accurate when there is crosstalk noise and/or intersymbol interference present, but it can nevertheless be used as a starting point for a search. Newton's method is an efficient method to find a local maximum since the method converges quadratically. Unfortunately, its stability is very dependent on the starting point. Therefore, simulated annealing is used to further improve the initial starting point t_{pd}, and to avoid nearby local maxima. This way the number of necessary iterations could be kept low. The probability for taking a downhill step in annealing was calculated using Boltzmann probability distribution.

The suitable parameters for simulated annealing were found empirically. A fast cooling was used since the starting point was already close to the maximum. The equation for cooling was $T = T * 0.2$ where T is the system temperature. The temperature was reduced twice and for each temperature four random moves were calculated. After that, two iterations of Newton's method were performed, resulting in a total of ten iterations to obtain the maximum noise induced by an aggressor. The phase of an aggressor was taken into account by adding it to t_{pd}. The error of this method was compared to an exhaustive sweep of the complete waveform for maximum voltage. The comparison was performed for 5000 randomly generated 8-bit buses where electrical parameters and signal rise times and phases were varied. The wire resistances were 5-780 Ω; capacitances were 25-4100 fF; inductances were 0.03-9.8 nH; source resistances were 50-750 Ω; load capacitances were 50-500 fF; rise times were 1-300 ps; and the phases were 0-300 ps. The switching activity of the bus consisted of random rising transitions. The results are shown as a histogram in logarithmic scale in

Fig. 3.5. The error was under 2% in 93% of test buses. As it can be seen the error remained very small in the vast majority of cases, except that in some cases the error was about 100 percent. This happened when the annealing algorithm was stuck at zero voltage. However, these cases are easily spotted and can be corrected by rerunning the algorithm with more iterations.

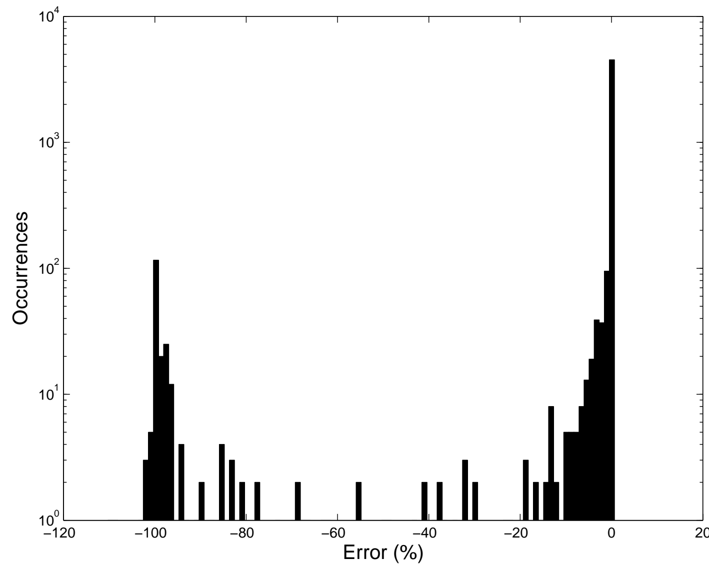

Figure 3.5: Error caused by the search for global maximum for 5000 random buses.

To find the 50% propagation delay of an interconnect, a combination of bisection method and Newton's method was used. Bisection method was used to find a suitable initial point for Newton's method. The search interval for the bisection method was the time between the input phase of the interconnect under study and the end of the clock cycle. An initial point between 20% and 70% percent of the operating voltage was found to result in good convergence for the Newton's method. An average of three iterations of bisection method was required to reach this interval. After this, Newton's method was run twice. A histogram for the error of this method for 5000 random 8-bit buses is shown in Fig. 3.6. The electrical parameters were the same as in peak crosstalk noise evaluation, with both rising and falling transitions on the bus. The error was within 2% in 96% of test buses. Both proposed methods have thus a good accuracy and require a small number of iterations.

3.2 Model Verification

The accuracy of the model was verified by comparing it to HSPICE and previous RC crosstalk models [24, 85, 86]. The HSPICE model consisted of 100 segments.

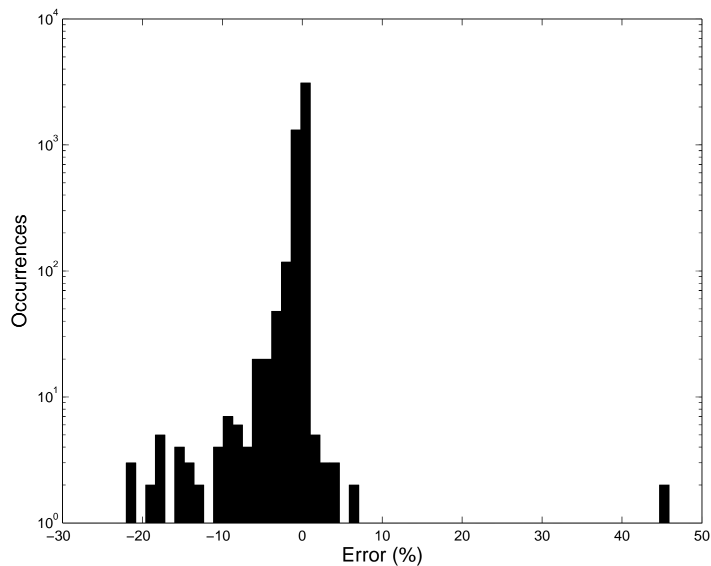

Figure 3.6: Error caused by the search for propgation delay for 5000 random buses.

Fig. 3.7 shows the crosstalk voltage on the victim line when one wire is switching and the other is quiet. The 2 mm long wires were modeled using an RC model. The self and coupling capacitances of the two wires were 52.77 fF/mm and 71.33 fF/mm, respectively. Resistance was 23.61 Ω/mm. The input signal was assumed to be a step input. As can be seen, the model is in close agreement with HSPICE. The induced noise for a 5 mm long interconnect with the same parameters is depicted in Fig. 3.8. The waveforms from the model and HSPICE were again nearly identical.

The case when two wires are switching in opposite direction was also verified. This situation is presented in Fig. 3.9. The RC wires were 2 mm long and had a rise time of 50 ps. The phase difference was 100 ps. The model was again in close agreement with HSPICE.

The model was further verified by comparing it to HSPICE using RLC modeling. The self and mutual inductance were 5.15 nH/mm and 3.46 nH/mm, respectively. The resistance and capacitance values remained the same. Fig. 3.10 shows the voltage waveforms when both wires are switching in the same direction with a rise time of 100 ps. The length of the wires was 2 mm. The induced crosstalk voltage on a quiet RLC interconnect is depicted in Fig. 3.11. The rise time of the aggressor was 100 ps.

The capability of the model to represent successive transitions was also verified. Fig. 3.12 shows the results when a square pulse is applied to two coupled RLC interconnects. The phase difference between the interconnects was 500 ps and rise time was 100 ps.

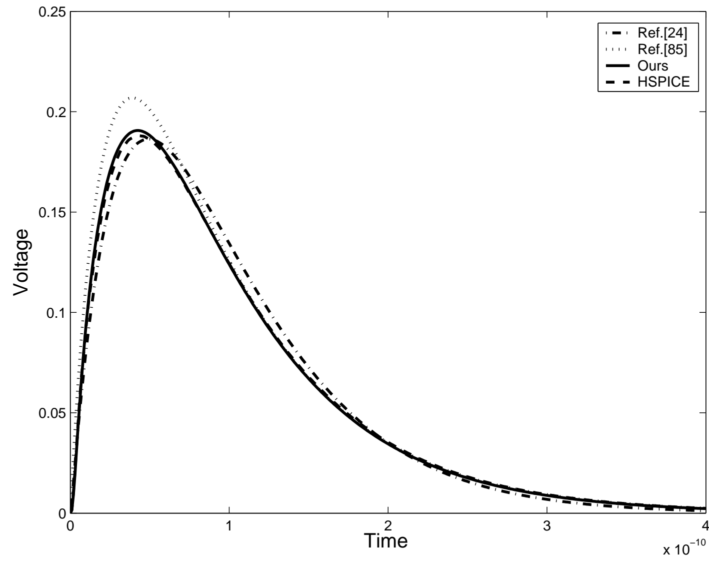

Figure 3.7: Crosstalk noise waveform on a 2 mm interconnect by different models.

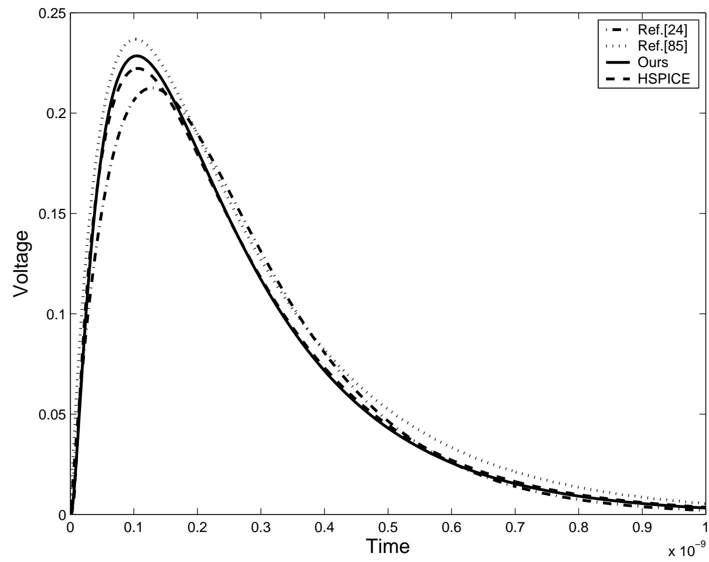

Figure 3.8: Crosstalk noise waveform on a 5 mm interconnect by different models.

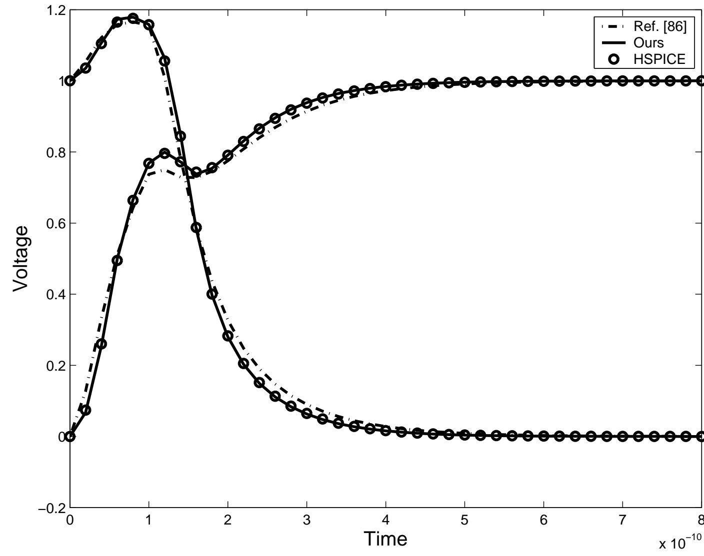

Figure 3.9: Voltage waveforms on two 2 mm interconnects switching in opposite directions.

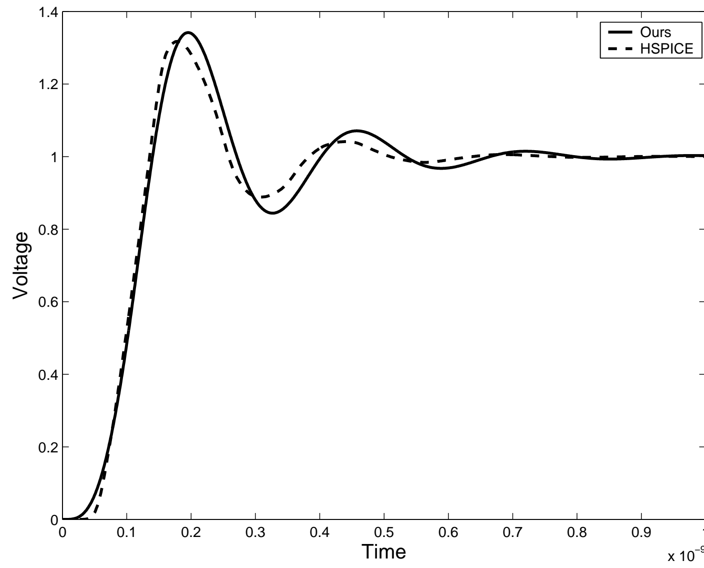

Figure 3.10: Voltage waveform on a 2 mm RLC interconnect.

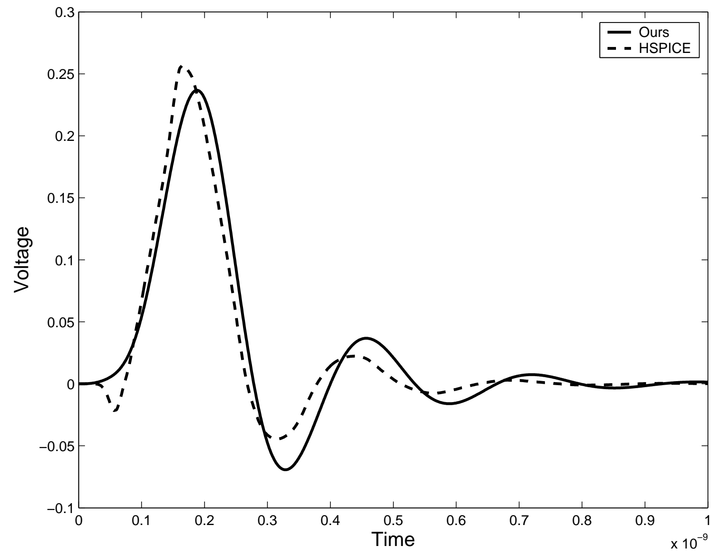

Figure 3.11: Crosstalk noise waveform on a 2 mm RLC interconnect.

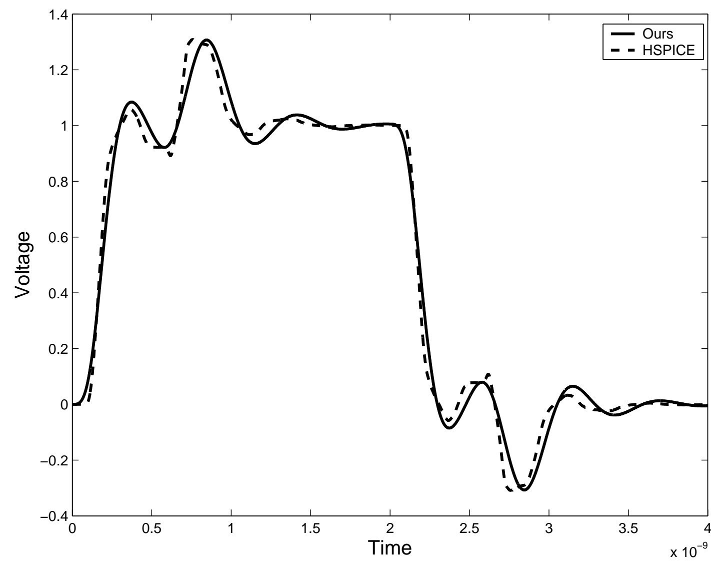

Figure 3.12: Square pulse on two 5 mm RLC interconnects with a 500 ps phase difference.

Transmission line behavior becomes significant when the rise time of a signal is less than or comparable to the time-of-flight delay of the line [87]. This can be seen from Table 3.1 where the model and HSPICE are compared. The table shows the peak crosstalk voltages that have been induced by an aggressor onto a quiet victim line at different wire lengths and rise times. The coupling capacitance and self capacitance of the interconnects were 120 fF/mm and 80 fF/mm, while the mutual inductance and self inductance were 1.5 nH/mm and 4 nH/mm, respectively. The wire resistance was 60 Ω/mm, and source resistance and load capacitance were 300 Ω and 150 fF, respectively. The error of the Π-model increased as aggressor rise time became shorter and wire lengths increased. This was caused by the inability of lumped circuits to model wave reflections. However, wide global interconnects present a large load to the driver that slows down the signal rise time. Furthermore, on-chip global interconnects with a length of more than 1-2 mm are usually divided with buffers into shorter segments. The accuracy of an RLC π-circuit in global interconnect modeling has been verified also in [88].

Table 3.1: Comparison of peak crosstalk voltages on a quiet wire. The values are normalized to the V_{dd}

Rise time [ps]	Length [mm]	Model	HSPICE	Error [%]
5	0.5	0.099	0.097	2.1%
	1	0.142	0.149	-4.7%
	4	0.231	0.220	5.0%
50	0.5	0.093	0.093	0%
	1	0.140	0.141	0.7%
	4	0.230	0.220	4.5%
100	0.5	0.088	0.088	0%
	1	0.134	0.134	0%
	4	0.229	0.219	4.6%
300	0.5	0.057	0.057	0%
	1	0.102	0.102	0%
	4	0.219	0.212	3.3%

The accuracy of the proposed model in different operating speeds and wire lengths was further assessed by comparing the calculated results and HSPICE simulations for four coupled copper interconnects. The global interconnects were sized at 0.6 μm $\times$ 1.2 μm. The clock frequency was varied between 100 MHz and 2 GHz while the length of the interconnects was between 0.5 mm and 10 mm. The simulation was run for seven clock cycles with the wires switching in opposite directions. The rise time of the interconnects was set to 10 percent of the clock cycle, i.e. from 50 ps to 1000 ps. The results are illustrated in Fig. 3.13. The error was calculated as the average of the difference between the waveforms from the model and HSPICE. The error of the proposed model increased with operating speed and wire length. This was again due to the

limited accuracy of the lumped Π-model. However, the error remained below four percent. The run time to obtain the data for Fig. 3.13 was 50 minutes for HSPICE, while the run time for the model was 70 seconds using a 2.8 GHz Pentium 4.

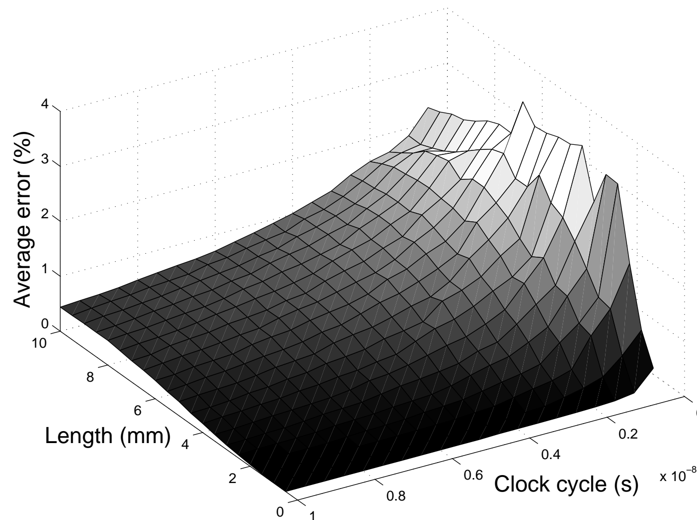

Figure 3.13: Difference between the proposed model and HSPICE simulations for four coupled interconnects.

3.3 Case Study

In high-speed data transmission the amount of noise is affected by multiple factors. Crosstalk noise and propagation delay are dependent on both the physical properties of interconnects and the switching activity on them. In this section, the model is applied to evaluate the influence of factors such as switching activity and phases on crosstalk noise and propagation delay in an 8-bit bus. The influence of intersymbol interference is also considered. The voltages are evaluated at the far-end of the parallel interconnects.

3.3.1 Switching Patterns

The amount of crosstalk noise and delay variation depends on the switching activity of coupled interconnects. The model was used to study the influence of switching activity on crosstalk noise on a bus consisting of eight 2.5 mm long parallel wires. The wires were sized at 0.6 μm × 1.2 μm and separated by 1.5 μm. The 8 × 8 transmission line matrices for the interconnects were extracted using Linpar [89] and FastHenry [90]. The total capacitance and self inductance of

a single interconnect were 84 fF/mm and 7.6 nH/mm, respectively. Resistance was 17.7 Ω/mm. The wires were numbered from one to eight starting from the left. The fourth wire was used as a reference wire in the measurements, since it was most susceptible to crosstalk noise. The simulation results for propagation delay and crosstalk noise are shown in Tables 3.2 and 3.3. In these tables, the first eight columns describe the switching status of the wires. The symbols '↑' and '↓' in the tables represent upward and downward transitions, respectively, while the symbol '-' represents no transition on the wire. In all cases the wires switched simultaneously with a rise time of 100 ps. The results are given for both RLC and RC models of the interconnect. The RC model was obtained from the original by reducing the amount of inductance by two orders of magnitude.

As it can be seen from patterns one and two in the Table 3.2, the propagation delay for the RC wire varied between 60 ps and 217 ps. The minimum delay was obtained when all wires were switching in the same direction. On the other hand, the maximum delay was obtained when the other wires were switching in opposite direction to the fourth wire. However, for the RLC wire the delay varied between 82 ps and 201 ps. The minimum delay was attained when wires 3 and 5 were switching in the same direction as wire 4 to maximize the delay enhancement of capacitive coupling, while the other wires were switching in the opposite direction to optimize the speed improvement by long-range inductive coupling.

Table 3.2: Propagation delay of the 4th wire in an 8-bit bus for different switching patterns

	Wire								Propagation delay	
	1	2	3	4	5	6	7	8	RLC model	RC model
Pattern 1	↑	↑	↑	↑	↑	↑	↑	↑	154 ps	60 ps
Pattern 2	↓	↓	↓	↑	↓	↓	↓	↓	90 ps	217 ps
Pattern 3	↑	↑	↓	↑	↓	↑	↑	↑	201 ps	149 ps
Pattern 4	↓	↓	↑	↑	↑	↓	↓	↓	82 ps	96 ps
Pattern 5	-	-	-	↑	-	-	-	-	133 ps	116 ps
Pattern 6	↑	-	-	↑	-	-	↑	↑	167 ps	103 ps
Pattern 7	↓	-	-	↑	-	-	↓	↓	98 ps	130 ps
Pattern 8	-	-	↑	↑	↓	-	-	-	131 ps	115 ps

The long-range effects of inductive coupling were also seen in propagation delay variation caused by interconnects further away. The propagation delay of a single switching interconnect was 133 ps and 116 ps for RLC and RC models, respectively. As shown in patterns 6 and 7 in the table, switching activity by wires 1, 7 and 8 caused the delay to vary between 98 ps and 167 ps for the RLC model and between 103 ps and 130 ps for the RC model. Wires can also cancel the effects of other wires on propagation delay variation. This situation is shown in pattern 8, where wires 3 and 5 cancel each other's influence on the

propagation delay of the 4th wire.

The crosstalk voltage induced on the fourth wire when others are switching is shown in Table 3.3. The maximum induced noise was 0.42 and 0.27 by RLC and RC models, respectively. The influence of distant wires was more prominent in RLC modeling, due to the long-distance effects of inductive coupling. The influence of distant wires can be used to determine a suitable number of wires to include in the model and thus further increase the efficiency of modeling of wide buses. Also in crosstalk noise modeling wires can cancel the influence of other wires. This is depicted in patterns 4 and 5.

Table 3.3: Crosstalk noise on the 4th wire in an 8-bit bus for different switching patterns. The values are normalized to the V_{dd}

	Wire								Crosstalk noise	
	1	2	3	4	5	6	7	8	RLC model	RC model
Pattern 1	↑	↑	↑	-	↑	↑	↑	↑	0.42	0.27
Pattern 2	-	-	↑	-	↑	-	-	-	0.20	0.17
Pattern 3	-	↑	↑	-	↑	↑	-	-	0.29	0.23
Pattern 4	-	-	↓	-	↑	-	-	-	<0.01	<0.01
Pattern 5	-	↓	↓	-	↑	↑	-	-	<0.01	< 0.01

3.3.2 Signal Phases and Rise Time

Crosstalk noise and propagation delay depend not only on the switching patterns of interconnects, but also on the relative arrival time of signals. The influence of timing was studied by increasing the phase of the fourth interconnect in an 8-bit bus consisting of global interconnects. The other wires switched simultaneously with upward or downward transitions. All wires had a rise time of 100 ps. The minimum and maximum propagation delays of the fourth wire for RC and RLC models are shown in Fig. 3.14. The delay values include the phase of the fourth wire. The minimum and maximum propagation delays were calculated from all possible upward and downward transitions of the 8-bit bus. The delay variation for the RC modeling was greatest when there was no phase difference between interconnects. As the phase of the fourth wire was increased, the variation in delay was reduced. However, the reduced delay variation was achieved at the cost of increased total propagation delay.

The delay variation was much greater when the RLC model was used. This was due to the ringing crosstalk voltage on the fourth wire that both increased or decreased delay variation depending on the phase of the fourth wire. For both RC and RLC models the maximum and minimum propagation delay of the fourth wire approach each other as the phase is increased. This is due to the fact that a crosstalk noise pulse has a finite duration.

The amount of induced noise on a quiet victim interconnect is heavily dependent on the rise time of aggressors. In Fig. 3.15 is shown the amount of

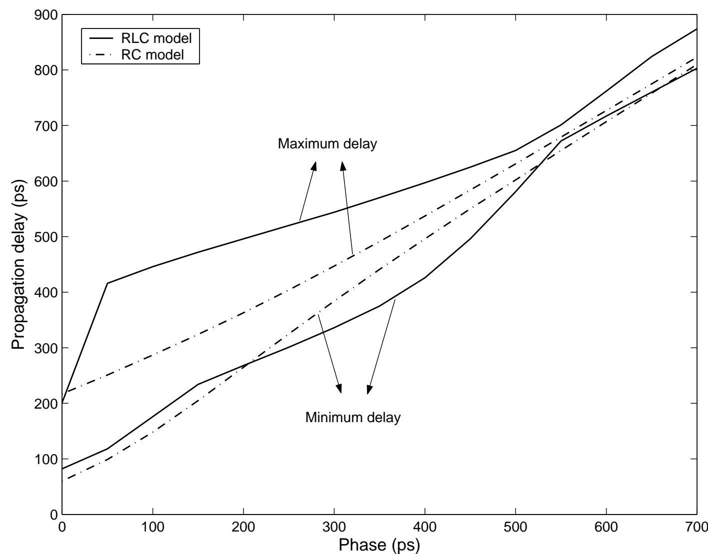

Figure 3.14: Influence of phase on the propagation delay of the fourth wire.

crosstalk noise at different rise times on the fourth wire when all other wires are switching. As it can be seen from the figure, an assumption of a step input at the driver can result in clear overestimation of noise.

3.3.3 Intersymbol Interference

Two noise forms, such as crosstalk noise and intersymbol interference, can be cumulative. The initial state of an interconnect affects its propagation delay and the amount of crosstalk noise induced into it. The influence of intersymbol interference on propagation delay variation was evaluated by simulating the bus for two cycles. The initial voltage on all wires of the bus was zero. The bit sequence on wires 2, 3, 5 and 6 was '10', and '01' on the fourth wire. Other wires were quiet. This caused a voltage peak to be induced on the fourth wire during the first clock cycle. This situation is depicted in Fig. 3.16. To increase the throughput of the bus, the clock cycle of the bus was shortened, while keeping all other parameters, such as rise time and bus length, constant. At a throughput of 250 MB/s, the bus was able to return to steady state between cycles, leading to a propagation delay of 145 ps at the fourth wire. However, at higher operating speeds intersymbol interference caused variation in propagation delay, as shown in Table 3.4. The propagation delay was both increased and decreased at different operating speeds, depending on whether there was overshoot or undershoot on the fourth wire at the beginning of the next cycle. However, the RC model induced a positive voltage peak on the fourth wire that did not oscillate, thus causing a steady decrease in the propagation delay.

Intersymbol interference also influenced the amount of crosstalk voltage in-

duced on a quiet wire. The induced voltage was measured at different operating speeds as in the delay variation measurements. The bit sequence on wires 2 and 3 was '11', and '01' on wires 5 and 6. Other wires were quiet. The induced crosstalk voltage on the fourth wire during the second cycle was therefore influenced by whether the previous voltage peak had already vanished. The results are shown in Table 3.5. As it can be seen, the induced voltage peak was both increased and decreased for the RLC model at different operating speeds, due to the oscillation at the previous cycle. However, the induced voltage peak only increased with operating speed when using the RC model.

Table 3.4: Propagation delay variation caused by intersymbol interference

Bus throughput (MB/s)	RLC delay (ps)	RC delay (ps)
250	145	206
500	142	206
750	140	206
1000	133	205
1250	176	203
1500	201	201
1750	166	198
2000	87	195

Table 3.5: Peak crosstalk noise (normalized to V_{dd}) variation caused by intersymbol interference

Bus throughput (MB/s)	RLC noise	RC noise
250	0.15	0.11
500	0.15	0.11
750	0.14	0.11
1000	0.16	0.11
1250	0.16	0.12
1500	0.15	0.12
1750	0.13	0.12
2000	0.13	0.13

3.3.4 Implications of the Case Study

Crosstalk noise and propagation delay variation in an 8-bit bus were studied. Simultaneous switching patterns strongly influenced the amount of noise induced on a quiet victim and the propagation delay of coupled interconnects.

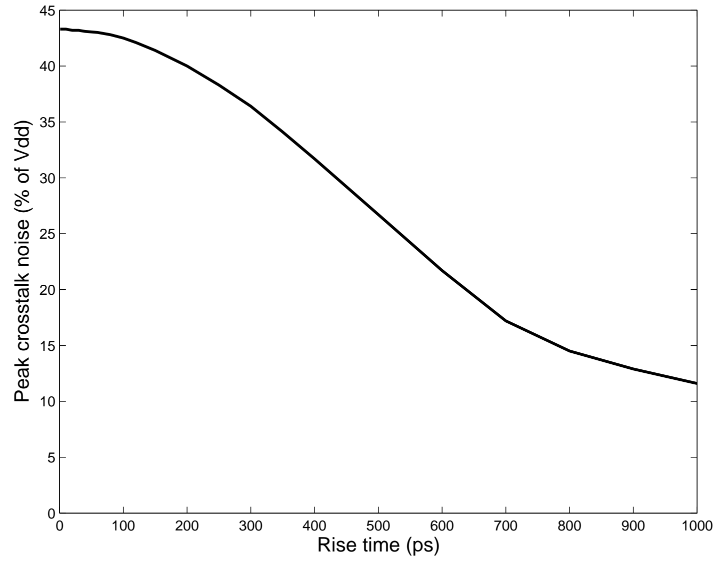

Figure 3.15: Influence of rise time on peak crosstalk noise.

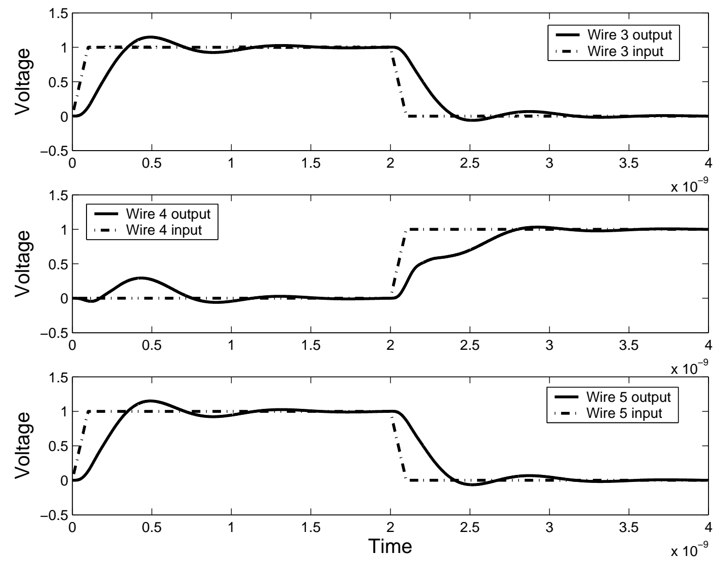

Figure 3.16: Voltage waveforms for three coupled RLC interconnects.

Rise times and and phases also contributed to crosstalk noise and propagation delay variation.

Certain bit sequences on the other hand caused intersymbol interference that further increased propagation delay variation and summed up with crosstalk noise. Propagation delay and crosstalk noise variation became more pronounced at high operating speeds. These variations need to be considered in the verification and optimization of high speed on-chip communication. Inductance modeling is also required since ringing and the long-range effects of inductive coupling made interconnects especially vulnerable to crosstalk noise and intersymbol interference.

3.4 Chapter Summary

In this chapter, an analytical time-domain model to evaluate crosstalk and intersymbol interference in capacitively and inductively coupled buses was proposed. The model can be used in design tools for high-performance buses since it takes into account the effects of inductance, initial states, and bit sequences. Signal rise times and phases were also included in the model. It was also shown that the model achieves good accuracy when compared to previous models and HSPICE. The model was applied to an 8-bit bus to study the amount of crosstalk noise and intersymbol interference in different switching and timing conditions. Intersymbol interference was shown to affect crosstalk noise and propagation delay depending on bus throughput and the amount of inductance.

Chapter 4

Modeling of Switching Current and Its Impact on Power Grid Noise

A stable supply voltage is a necessity for the correct operation of an integrated circuit. Maintaining this operating voltage has become increasingly difficult as the integration density and the number of devices on a chip increase. Rigorous models for the simultaneous switching noise caused by a CMOS logic gate have been proposed [91, 92]. An increasing portion of power is however consumed by interconnects. Over 50% of the dynamic power consumption of a 130 nm microprocessor was consumed by interconnects and about half of this interconnect-power was consumed by global wires [4]. These long wires can not be accurately modeled as a single load capacitor to the driver. The modeling of the power supply grid is also needed since the amount of noise varies in different locations of the power supply grid. The on-chip power supply network and global communication design starts early in the design flow. The current draw of the on-chip buses needs to be known in order to specify the power supply network. The current draw of the buses in turn depends on their design properties such as width, length and switching activity. Rapid modeling and exploration of power supply network and bus design parameters is therefore very beneficial for system level optimization.

In the previous chapter, models and analysis for crosstalk and intersymbol interference in a bus were presented. In this chapter, power supply noise caused by a bus is modeled [93]. The switching current of a coupled bus is derived and the bus model is combined with a power supply network model. The bus is represented by an analytical RLC transmission line model. The model also takes into account different switching patterns and coupling between wires that can both have a considerable effect on the current draw of the bus. A method to reduce the power supply noise by adjusting the relative timing of bus drivers is demonstrated.

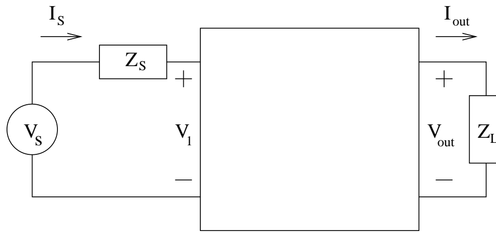

Figure 4.1: Two-port model for an interconnect with source and load impedances.

4.1 Modeling of Bus Switching Current

In addition to modeling the power distribution network, it is necessary to model or approximate the load on the network. Switching events cause current spikes, whose shape and magnitude affect the amount of noise on the power distribution network. Large current spikes are caused by on-chip communication, since buses are often driven with large drivers and buffered heavily. In buses, coupling also becomes pronounced since the wires run parallel to each other over long distances. This necessitates the inclusion of coupling in wire models. Simulation of power distribution noise in a chip is typically done in two steps: first, the switching currents of active devices are simulated separately assuming a perfect supply voltage. Second, the noise in the power distribution network is simulated using as loads piecewise-linear current sources that approximate the switching currents. This method helps to keep the analysis computationally feasible. In this section, transmission line analysis in s-domain is used to derive the switching current of a coupled on-chip bus under different switching conditions.

A transmission line with a source impedance Z_S and load impedance Z_L can be modeled as a two-port circuit as in Fig. 4.1. The terminal equations of the two-port network are

$$V_1 = a_{11}V_{out} + a_{12}I_{out} \tag{4.1}$$

$$I_s = a_{21}V_{out} + a_{22}I_{out} \tag{4.2}$$

$$V_s = V_1 + I_s Z_S \tag{4.3}$$

$$V_{out} = I_{out}Z_L. \tag{4.4}$$

The relation between the voltage V_{out} at the end of the interconnect and the voltage source V_s can be derived from the equations above

$$\frac{V_{out}}{V_s} = \frac{Z_L}{(a_{11} + Z_S a_{21})Z_L + a_{12} + Z_S a_{22}}. \tag{4.5}$$

A transmission line can be thought to consist of numerous infinitesimally small RLC segments. A cascade connection of these segments is conveniently analyzed using ABCD parameters, since the ABCD matrix of the cascade system

is simply the matrix product of the individual matrices. As the number of the RLC segments approaches infinity, the ABCD parameter matrix of a single distributed RLC interconnect becomes [28]:

$$\begin{pmatrix} a_{11} & a_{12} \\ a_{21} & a_{22} \end{pmatrix} = \begin{pmatrix} \cosh(\theta h) & Z_0 \sinh(\theta h) \\ Z_0^{-1} \sinh(\theta h) & \cosh(\theta h) \end{pmatrix} \tag{4.6}$$

where $Z_0 = \sqrt{(r+sl)/(sc)}$ and $\theta = \sqrt{(r+sl)sc}$ and where r,l,c are the per-unit-length resistance, capacitance and inductance, respectively, of the interconnect of length h. The driver is modeled as an exponential voltage source with a series impedance Z_s. The input voltage V_s is

$$V_s(t) = \left(1 - e^{-\frac{t-\tau}{t_r}}\right) u(t-\tau) \tag{4.7}$$

where t_r is the exponential signal rise time and $u(t)$ is the unit step function. τ is the time when the driver starts switching. The voltage source in s-domain is

$$V_s(s) = \left[\frac{1}{s} - \frac{1}{s + \frac{1}{t_r}}\right] e^{-\tau s}. \tag{4.8}$$

The current drawn from the power supply network is equal to the current at the driver end of the interconnect. The current pulse at the receiver end of the interconnect is smaller since a part of the current is lost charging the intrinsic capacitance of the interconnect. The current I_s entering the interconnect can be derived by substituting $I_{out} = V_{out}/Z_L$ into (4.2) and writing it as

$$I_s = (a_{21} + \frac{a_{22}}{Z_L})V_{out}. \tag{4.9}$$

By substituting (4.5) into (4.9), the relation between the current and voltage source is obtained as

$$\frac{I_s}{V_s} = \frac{Z_L a_{21} + a_{22}}{(a_{11} + Z_S a_{21})Z_L + a_{12} + Z_S a_{22}}. \tag{4.10}$$

For a distributed transmission line with source resistance and inductance and receiver load capacitance, the equation can be written as

$$\frac{I_s}{V_s} = \frac{Z_0^{-1} \sinh(\theta h) + sC_L \cosh(\theta h)}{(Z_S s C_L + 1)\cosh(\theta h) + \left(Z_0 s C_L + Z_0^{-1} Z_S\right)\sinh(\theta h)} \tag{4.11}$$

where $Z_S = R_S + sL_S$. The current can not be solved from the equation analytically, but it can be approximated using a series expansion. The hyperbolic functions can be written in series form as

$$\cosh(\theta h) = 1 + \frac{(r+sl)sch^2}{2!} + \frac{(r+sl)^2 s^2 c^2 h^4}{4!} + \frac{(r+sl)^3 s^3 c^3 h^6}{6!} + \ldots \tag{4.12}$$

$$Z_0 \sinh(\theta h) = (r+sl)h + \frac{(r+sl)^2 sch^3}{3!} + \frac{(r+sl)^3 s^2c^2h^5}{5!} + \dots \tag{4.13}$$

and

$$Z_0^{-1} \sinh(\theta h) = sch + \frac{(r+sl)s^2c^2h^3}{3!} + \frac{(r+sl)^2 s^3c^3h^5}{5!} + \dots \tag{4.14}$$

The accuracy of a series expansion depends in general on the number of terms. A fourth degree approximation was used since the fourth degree polynomials are the highest that can be solved analytically. A fourth degree approximation can be written in series form as

$$\frac{I_s}{V_s} \approx \frac{n_3 s^4 + n_2 s^3 + n_1 s^2 + n_0 s}{b_4 s^4 + b_3 s^3 + b_2 s^2 + b_1 s + 1}. \tag{4.15}$$

By substituting (4.8) into (4.15) the current is obtained as

$$I_s = \frac{(n_3 s^3 + n_2 s^2 + n_1 s + n_0)e^{-\tau s}}{d_4 s^4 + d_3 s^3 + d_2 s^2 + d_1 s + d_0}. \tag{4.16}$$

The coefficients n_i and d_i are presented in the Appendix. By applying partial fraction expansion and taking an inverse Laplace transform the current in time domain becomes

$$I_s(t) = \sum_{p=1}^{4} A_p e^{s_p(t-\tau)} u(t-\tau) \tag{4.17}$$

where s_p are the roots of the denominator of (4.16).

In order to model the current draw of a bus, the equations are now extended to multiple coupled interconnects. The bus was modeled as capacitively and inductively coupled RLC transmission lines. The circuit model of the bus is shown in Fig. 4.2.

As can be seen from (2.10), the current on a coupled interconnect is a sum of the currents of decoupled interconnects. The inputs of these decoupled interconnects are in turn a sum of the original inputs of coupled interconnects. By combining these equations, the total current draw of the bus can be derived as a sum of the n interconnect currents

$$I_{tot} = \sum_{k=1}^{n} \sum_{i=1}^{n} \mathbf{M}_{ki} \sum_{j=1}^{n} \mathbf{M}_{ij}^{T} I_i(t, \tau_j) \tag{4.18}$$

where $\mathbf{M}_{ki}$ and $\mathbf{M}_{ij}^{T}$ are the value of the eigenvalue matrix and its transpose at the indexes k,i and i,j, respectively. $I_i(t, \tau_j)$ is the input current of a single decoupled interconnect (4.17). τ_j is the time when the jth driver starts switching. The current I_i is calculated using the diagonalized resistance, capacitance and

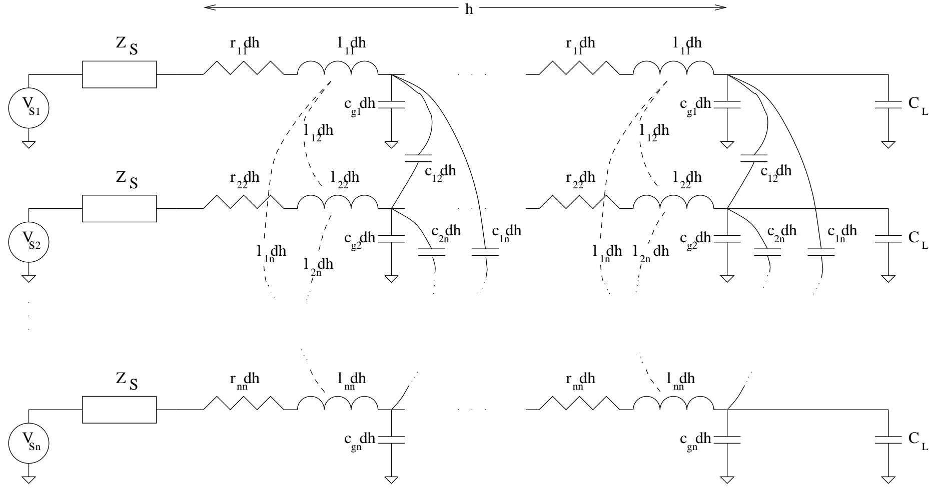

Figure 4.2: Circuit model for a distributed RLC bus consisting of n interconnects.

inductance values of $\hat{R}_{ii}$, $\hat{C}_{ii}$, and $\hat{L}_{ii}$, respectively. In summing the currents, their direction needs to be taken into account, i.e. whether the driver is switching up or down. A downward transition is included in the sum with a minus sign. Also, due to coupling there can be a small current pulse on a non-switching wire. This current flows either into the power distribution network or ground depending on the state of the driver.

4.2 Modeling of Power Supply Network

Many existing power grid models focus on post-layout verification. In [94], a model for evaluating the RLC power grid noise in the early stages of the design flow has been presented. This model was therefore chosen to be used with the derived switching current model. The models were combined as follows. The worst case operating voltage at an arbitrary power grid node j was derived in [94] as

$$V_j^{min} = \frac{1}{\lambda_j}\left(\sum_{i=1,i\neq j}^{k} \chi_{i,j} V_i^{min} + \frac{1}{2}\sum_{i=1,i\neq j}^{k} C_{i,j} V_{dd}\right) \tag{4.19}$$

where $\lambda_j = \sum_{i=1,i\neq j}^{k} \chi_{i,j} + (1/2)\sum_{i=1,i\neq j}^{k} C_{i,j} + C_j^{load}$ and $\chi_{i,j} = t_s^2/(6L_{i,j} + 3R_{i,j}t_s)$. C_j^{load} is the load capacitance at node j and t_s is the switching time of node.

The charge transferred from the power supply network when an on-chip bus is switching can be obtained by integrating (4.18). If all drivers are switching

simultaneously the total charge is

$$Q_{tot} = \int_0^\infty I_{tot}(t)\ dt = \sum_{k=1}^{n} \sum_{i=1}^{n} \mathbf{M}_{ki} \sum_{j=1}^{n} \mathbf{M}_{ij}^T \sum_{p=1}^{4} \frac{-A_p}{s_p}. \tag{4.20}$$

If there are drivers switching at different times the integration is performed for the corresponding time intervals to take into account the direction of currents as discussed above. The load capacitance corresponding to this charge was then obtained as $C^{load} = Q_{tot}/V_{dd}$.

4.3 Verification

The bus model was verified by comparing it to HSPICE. The wire properties were set according to ITRS 65 nm technology node for global wiring. The width and separation distance of the wires were 145 nm. The resistance and inductance values were extracted using the field solver FastHenry [90], while the capacitance values were extracted using Linpar [89]. The driver rise time was 100 ps.

Fig. 4.3 shows the switching current of a 1 mm long 8-bit bus. Every other driver is switching up while the others are switching down in order to maximize the load caused by capacitive coupling. The downward switching drivers start switching 200 ps after the upward ones. The influence of coupling between the wires is seen as a jump in the current drawn from the power supply network. As can be seen, the model and HSPICE were close to each other. In Fig. 4.4 is shown the current draw of a 3 mm long 32-bit bus when all drivers are switching up simultaneously. The wire sizes remained the same. The model and HSPICE were again in good agreement with each other.

The simulation runtimes for the calculation of a bus current draw are shown in Table 4.1. The simulations were run on a 2.8 GHz Pentium 4. The model was implemented with Matlab 6 while the HSPICE simulations were performed using the W-element lossy transmission line model. The runtimes were measured for three different bus widths, i.e. 8-bit, 32-bit and 64-bit. As can be seen, there is a clear speed-up over HSPICE, especially for the wide 64-bit bus where the speed-up is over 100. Further speed increases can likely be obtained with a compiled executable instead of source code interpreted at run-time in Matlab.

Table 4.1: Simulation times for the calculation of current draw curves for different bus widths

Bus width	Model (sec)	HSPICE (sec)
8-bit	0.07	0.19
32-bit	0.12	3.80
64-bit	0.20	24

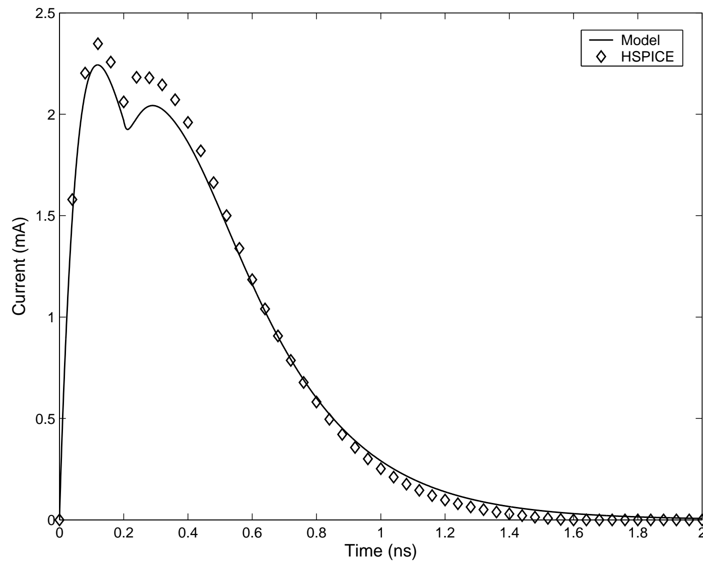

Figure 4.3: Current draw of a 1 mm long 8-bit bus. Half of the drivers are switching up while the others start switching down at 200 ps.

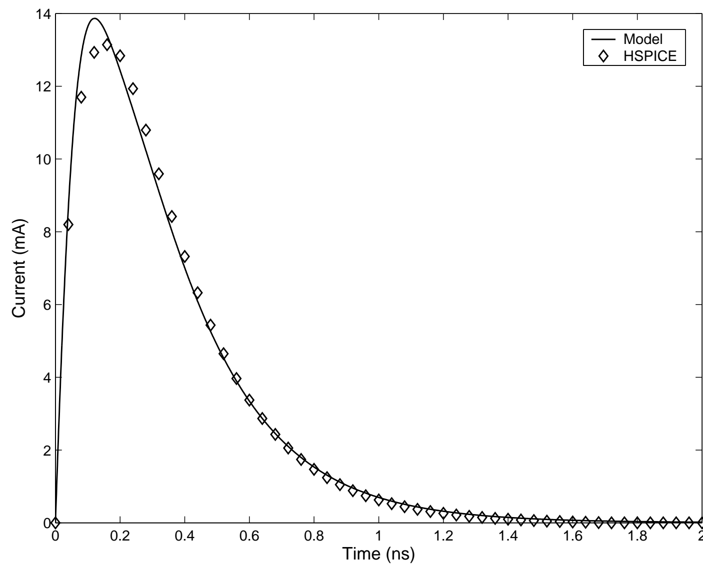

Figure 4.4: Current draw of a 3 mm long 32-bit bus. All drivers are switching up simultaneously.

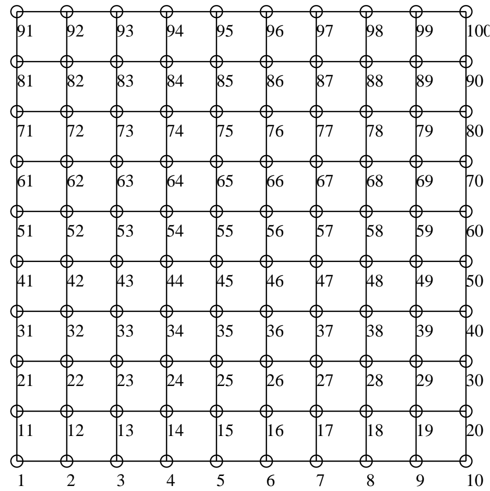

Figure 4.5: A 10× 10 power supply grid. Each segment is 100μm.

The bus model was also verified together with the power supply grid model. The power grid was modeled as a square grid as shown in Fig. 4.5. Each 100 μm long segment was modeled as an RLC circuit. The nodes 1, 10, 91 and 100 were modeled as package pins with a constant operating voltage. The power grid wires were 2 μm wide and 0.319 μm thick. The 3 mm long 32-bit bus whose current draw is shown in Fig. 4.4 was placed at node 55. The worst case operating voltage in each node is shown in Fig. 4.6. The maximum difference in noise voltages between the model and HSPICE was below 8%.

The runtimes for the simulation of a power supply grid are shown in Table 4.2. In HSPICE simulations the load on the supply grid was a piecewise linear current source representing the current draw curve of a bus. The power grid simulation was approximately 30 times faster than HSPICE. For larger grid sizes sparse matrix solvers may be utilized as discussed in [94].

Table 4.2: Simulation times for different power supply grid sizes

Grid size	Model (sec)	HSPICE (sec)
100	0.01	0.02
400	0.03	0.99
900	0.14	3.5
2500	0.98	34

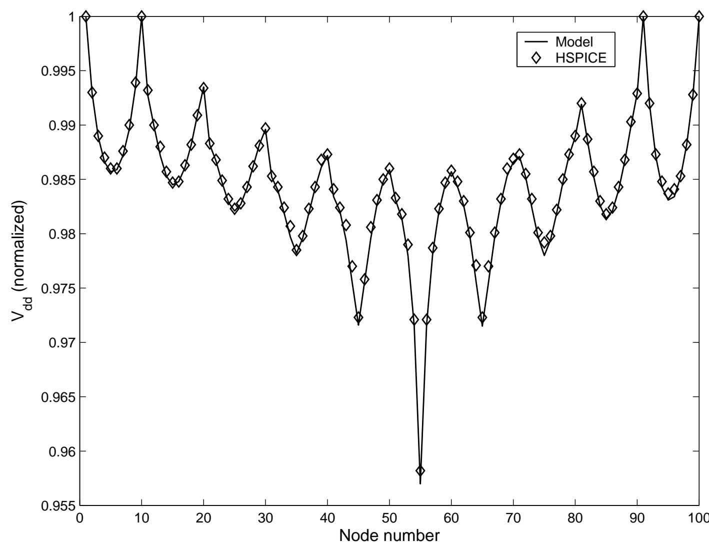

Figure 4.6: Worst case node voltages on the power supply grid.

4.4 Noise Reduction by Skewing

The bus model can be used to analyze the influence of different timing conditions. The current peaks caused by switching buses can be reduced by skewing the relative switching time of drivers [71]. In Fig. 4.7 is shown the worst case operating voltage when half of the drivers of the 3 mm long 32-bit bus switch 0 ps, 200 ps, or 400 ps after the other drivers. When there was no skewing, the maximum noise at node 55 was 4.3% of V_{dd}. With a skewing time of 200 ps the maximum noise was reduced by 16% to 3.6% of V_{dd}. A 400 ps skew further reduced the noise to 3% of V_{dd} resulting in a total reduction of 30% in the power supply noise. The maximum noise was reduced also in the other nodes. Further increases in skew no longer reduced the noise due to the loss of correlation between the switching drivers. In this way the power supply noise can be reduced as a trade-off between noise and skewing delay. The maximum possible skewing time depends on how much slack there is available for a particular bus when compared to the system level operating frequency.

4.5 Chapter Summary

In this chapter, an analytical model for the switching current of an on-chip coupled bus was proposed. The model was combined with a power supply grid model in order to be able to model the worst case power supply noise in different parts of the power supply grid. The model was verified by comparing it to HSPICE. The maximum error was below 8%. The reduction in power supply

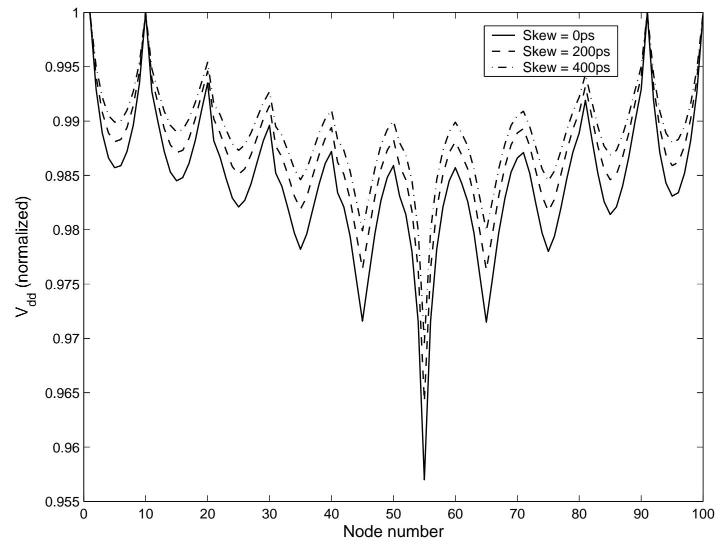

Figure 4.7: Node voltages on the power supply grid with different bus driver skewing times.

noise caused by skewing of the drivers was demonstrated. In the case study the maximum power supply noise caused by a 32-bit bus was reduced by 30% with a 400 ps skewing time. In the next chapter, the derived switching current model is applied with a novel trade-off method to reduce both power supply noise and functional crosstalk.

Chapter 5

Reduction of Functional Crosstalk and Power Supply Noise

In digital circuits a large number of logic elements and drivers switch nearly simultaneously at the clock edge. This switching places a burden on maintaining a stable operating voltage. Significant switching currents are caused by global on-chip communication, since buses are driven with large drivers. Current peaks in turn cause resistive RI drop and inductive Ldi/dt noise in the power distribution network. On-chip decoupling capacitors help to reduce the burden on the power distribution network by acting as temporary charge storage. However, these capacitors may occupy a considerable area on the chip. In [95, 96, 97] alternative methods for peak current or power reduction in buses have therefore been proposed. The reduction is achieved with additional encoding circuits or wires. The impact on noise in the surrounding power supply network is also not modeled. In addition to peak current reduction, crosstalk reduction is an important part of bus design. The adverse effects of crosstalk include increased delay or delay variation, voltage peaks on quiet wires and increased energy consumption. Methods for reducing the effects of crosstalk include bus encoding [98, 99, 100], wire spacing adjustments [101], buffer insertion [33], shielding [102, 103] and gate sizing [35, 104].

Wire spacing and shielding may dramatically increase the area of a bus. Buffer insertion in turn increases power consumption and area. Bus encoding requires a smaller area than simple shielding but also additional logic. In principle, the reduction in crosstalk in these methods is achieved as a trade-off between noise and circuit area or power. On the other hand, gate sizing, i.e. altering of driver strengths, is problematic in buses since in a typical bus the wires have the same size and separation distance, which causes them to act equally as both an aggressor and a victim.

In this chapter, both functional crosstalk and power supply noise are si-

multaneously reduced using primarily another system resource, i.e. time. In the previous chapters, the crosstalk noise on a bus and the power supply noise caused by a bus have been modeled and analyzed. In this chapter, the models are applied to reduce these two noises. Time, or timing slack, has been previously used in buses for other purposes such as in [105, 106] where the delay of a coupled bus was reduced by intentionally skewing the timing of adjacent wires. Skewing was again applied in [107] to reduce the energy dissipation of a coupled bus and in [108] where it was used to reduce bus peak power. It should be noted that while intentional skewing has previously been used to reduce such crosstalk effects as crosstalk induced delay increase [105] and crosstalk energy dissipation [107] in buses, in this chapter crosstalk voltage induced on quiet victim wires is reduced as first proposed in [71, 109]. Both inductive and capacitive crosstalk are also analyzed with an analytical RLC bus model instead of an RC model. In addition, the power supply noise caused by an on-chip bus is simultaneously reduced. Unlike many other methods [95, 96, 108] that have reduced the peak current or power of a switching on-chip bus, the actual impact of the peak current reduction on noise in the power supply grid is included in the model. Since the method is primarily based on a trade-off between noise and delay instead of circuit area or power, it is well suited for area limited cases, where wire shielding or additional encoding wires are often not available. Another problematic issue for crosstalk reduction is inductive coupling due to its long range effects that reduce the effectiveness of wire shielding and spacing. The proposed method, however, is demonstrated to be effective also for reducing inductive noise.

5.1 Reduction of Crosstalk and Power Supply Noise

Skewing can be applied in several ways to a bus. For example, in [105] the skewing to reduce the delay of a coupled bus was performed by adding a relative static delay between adjacent wires. In effect, the bus was divided into two parts: every other wire switched normally at the clock edge and the others after an imposed delay. This division is however not necessarily effective in reducing functional crosstalk noise, since the two closest aggressors of a victim wire that cause the majority of capacitive noise are still switching simultaneously. This problem can however be avoided by dividing the wires into several groups as depicted in Fig. 5.1. The relative switching times of the bus drivers are skewed by inserting a static delay to part of the wires. This also eases the burden on the power supply network, since there are fewer drivers switching simultaneously.

The skewing time of each driver is a multiple of the interval time T_{int}. On the left hand side of the figure, the wires are divided into two groups with two different skewing times, namely, 0 and T_{int}. On the right, there are five different skewing times; 0, T_{int}, $2T_{int}$, $3T_{int}$ and $4T_{int}$. Three and four skewing times are shown in the middle of the figure. Due to the different skewing times, the

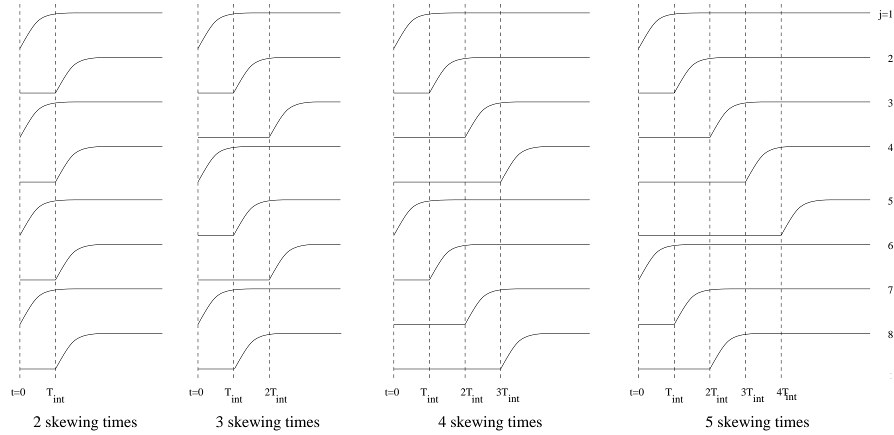

Figure 5.1: Skewed inputs to a bus using 2-5 different skewing times.

two closest aggressors on both sides of of any victim wire do not switch at the same time when there are three or more different skewing times. The crosstalk pulse induced on a quiet interconnect is thus lowered. This is demonstrated in Fig. 5.2. The figure shows the noise waveform induced on the quiet 4th wire in the middle of an 8-bit bus when all other wires are switching. There were four different skewing times as demonstrated in Fig. 5.1. The wires were 2 mm long and had a rise time of 100 ps. The noise was calculated using three different interval times T_{int}. With a zero interval time, all wires switch simultaneously. In this case, the maximum crosstalk noise on the quiet interconnect was 35% of V_{dd}. With an interval time of 250 ps, the maximum noise was reduced to 27% of V_{dd}. By increasing the interval time to 500 ps, the maximum noise was further reduced to 19% of V_{dd}.

Fig. 5.3 shows the switching current of the same 8-bit bus. When all interconnects switched simultaneously, the peak current was 3.6 mA. With an interval time of 250 ps, the peak current was reduced to 1.8 mA, while an interval time of 500 ps reduced the peak current further to 1.4 mA. The current waveform formed four distinct peaks, since there were four different skewing times.

5.2 Bus and Power Supply Noise Modeling

5.2.1 Crosstalk Noise and Delay under Bus Skewing

To be able to determine a suitable skewing time, the crosstalk noise and power supply noise need to be evaluated efficiently and accurately. The skewing time should be selected as small as possible to avoid excessive delays, while still fulfilling signal integrity and power supply noise requirements. In the previous

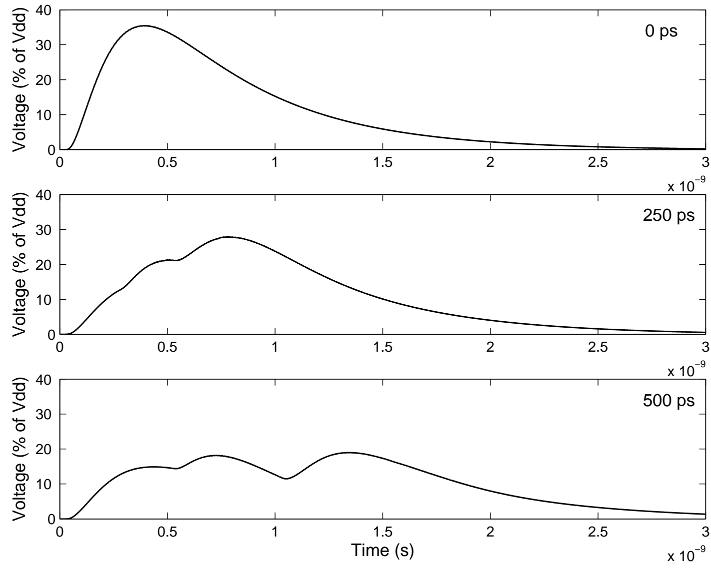

Figure 5.2: Crosstalk voltage on a quiet interconnect in an 8-bit bus with interval times of 0ps, 250ps, and 500ps.

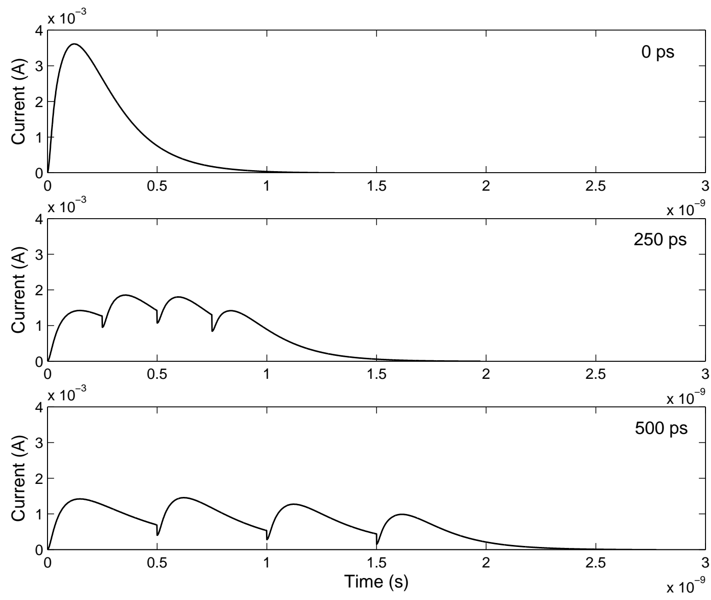

Figure 5.3: Switching current of an 8-bit bus with interval times of 0ps, 250ps, and 500ps.

chapter, the switching current of a coupled bus was derived. The model is used in this chapter for a bus with skewing. The delay and crosstalk voltage on a quiet wire in a skewed bus can be calculated as follows.

The drivers are modeled as exponential voltage sources $\mathbf{V}_S$ with a source impedance in series. The input voltage is

$$V_s(t) = \left(1 - e^{-(t-\tau_j)/t_r}\right) u(t - \tau_j) \tag{5.1}$$

where τ_j is the skewing time when the jth driver starts switching as shown in Figure 5.1. u is the unit step function and t_r is the exponential rise time. The skewing time of each interconnect is defined as a multiple of interval time τ_{int}

$$\tau_j = [(j-1) \bmod p]\, \tau_{int} \tag{5.2}$$

where p is the number of different skewing times.

The receiver is modeled as a capacitive load. The relation between the input voltage V_s and voltage V_{out} at the end of a transmission line is

$$\frac{V_{out}}{V_s} = \frac{Z_L}{(a_{11} + Z_S a_{21}) Z_L + a_{12} + Z_S a_{22}} \tag{5.3}$$

where a are defined in (4.6) and Z_S and Z_L are the source and load impedances, respectively. Similarly to the calculation of current in the previous chapter, the voltage V_{out} at the end of a single wire is obtained by combining (5.1) in s-domain with (5.3) and applying a fourth degree series expansion with inverse Laplace transform

$$V_{out} = \sum_{i=1}^{4} B_i e^{s_i (t-\tau)} u(t-\tau). \tag{5.4}$$

For multiple coupled wires, by combining (5.4), (2.9) and (2.20) the output voltage of the kth wire in an n-bit skewed bus is obtained as

$$V_{out_k} = \sum_{i=1}^{n} \mathbf{M}_{ki} \sum_{j=1}^{n} \mathbf{M}_{ij}^T V_i(t, \tau_j) \tag{5.5}$$

where $V_i(t, \tau_j)$ is the output voltage (5.4) of the ith decoupled interconnect as a function of time t and skewing time τ_j.

The maximum crosstalk noise on a quiet victim wire is obtained when all other wires are switching. In a bus the interconnect in the middle of the bus is generally the most susceptible to crosstalk noise. The crosstalk noise waveform on any interconnect can be obtained from (5.5). To determine the maximum value of crosstalk noise, the maximum of that equation needs to be found. However, it can not be derived analytically. The maximum was searched for with Halley's method. Halley's method was applied instead of the Newton-Raphson method since in practical experiments it was less sensitive to the starting point. As a starting point for the search (3.15) was used. Due to the intentional skewing the aggressors start switching at different times and thus the voltage

waveform on the victim can have several peaks depending on the number of different skewing times as demonstrated in Fig. 5.2. The starting points for the search were therefore set as the sum of (3.15) and the time when each group of aggressors started switching.

The 50% propagation delay of any wire in the bus can be obtained by setting (5.5) equal to $0.5\mathrm{V_{dd}}$. The equation can be used to analyze all driver switching patterns by including downward switching drivers with a minus sign in the sum. The solution to the equation was again obtained with Halley's method. The starting point was obtained from (3.15). Since the equation is for a single wire, a better starting point was obtained by modifying the total wire capacitance term in it by multiplying the coupling capacitance with the appropriate Miller coupling factor depending on the activity of adjacent wires.

5.2.2 Power Supply Noise under Bus Skewing

In order to evaluate analytically the effect of the reduced number of simultaneously switching drivers on power supply noise, the power supply grid was modeled as a network of RLC segments as in [94] as discussed in the previous chapter. Since the original power grid model does not include non-simultaneous switching, the characterization of the switching devices was modified in order to evaluate the change in power supply noise as a function of skewing [110]. The switching devices in the power grid model are characterized as switching capacitors with a pre-characterized load capacitance of C^{load} and switching time t_s. An on-chip bus to which skewing can be applied was instead characterized using two pre-characterized values of C^{load} and t_s. One characterization was performed normally with HSPICE for the bus with no skewing, while the other was performed for a chosen interval time T_{int}. When the interval time of a bus changes, its load capacitance also changes since there is a change in the Miller coupling capacitance. The load capacitance C^{load} for any interval time was calculated using (4.18). The corresponding new switching time t_s of the load capacitor for any interval time was then obtained from the two pre-characterized values by approximating the dependence between C^{load} and t_s as linear. In the simulations, in addition to the regular characterization of the bus with zero skew, the bus was also characterized using an interval time of 500 ps.

5.3 Model Verification

The accuracy of the model was verified by comparing it to HSPICE. The verification was performed using several different driver rise times, source resistances, load capacitances, bus lengths and interval times. Two different buses and power grids were used in the verification. The RLC parameters for the bus and power grid were extracted using FastHenry [90] and Linpar [89]. The first case was an 8-bit bus whose wires were 145 nm wide, and 319 nm thick with a separation distance of 145 nm. The power supply network was a 10×10 grid whose sides were 2 mm long. The power grid wires were 2 μm wide. The bus was

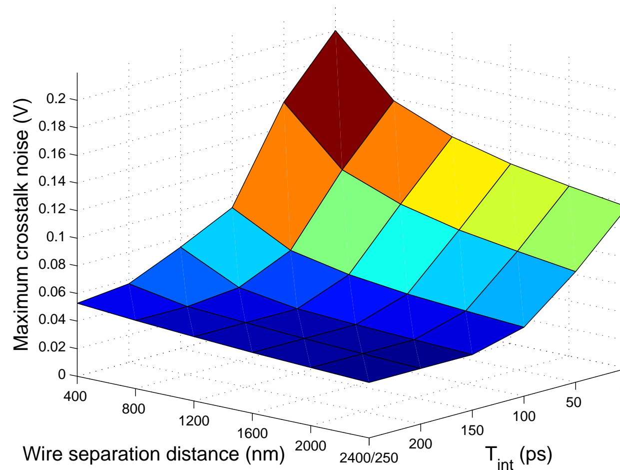

Figure 5.4: Maximum crosstalk noise on a 2 mm 32-bit bus as a function of wire separation distance and interval time.

placed in the middle of the power grid. The verification results for this setup are shown in the upper half of Table 5.1. Verification results were calculated for maximum crosstalk voltage, worst-case power grid voltage and worst-case 50% propagation delay. The delay of the skewed bus was calculated from the first input switching to the last output switching. Four different skewing times were used.

The other verification case was a 16-bit bus whose wires were 300 nm wide, 319 nm thick and the separation distance was 400 nm. The power distribution network was now a 20×20 grid whose sides were 1 mm long. The verification results for this case are shown in the lower half of Table 5.1. The average error between the model and HSPICE was 1.4%, while the maximum error was 12.9%.

5.4 Case Study and Implementation

5.4.1 Reduction of Inductive Crosstalk Noise

Inductive coupling has become a concern in global interconnects due to its long range. Unlike capacitive coupling, inductive coupling is reduced only slowly with distance or signal line insertion [111]. Even shielding with Vdd or ground lines may eliminate only part of the inductive coupling [112]. In this section, the applicability of the proposed skewing method is demonstrated in reducing inductive crosstalk noise.

Fig. 5.4 shows the influence of wire separation distance and skewing on

Table 5.1: Verification results for crosstalk voltage, worst-case supply voltage, and propagation delay using different bus sizes and interval times

8-bit bus: wire width 145 nm, wire distance 145 nm, wire thickness 319 nm										
R_s (Ω)	C_L (fF)	t_r (ps)	h (mm)	T_{int} (ps)	V_{xtalk}^{model} (V)	V_{xtalk}^{spice} (V)	V_{dd}^{model} (V)	V_{dd}^{spice} (V)	t_{prop}^{model} (ps)	t_{prop}^{spice} (ps)
250	10	25	2	0	0.460	0.469	0.925	0.925	401	406
500	10	25	2	50	0.441	0.451	0.949	0.952	601	608
1000	10	25	3	100	0.450	0.458	0.963	0.968	1475	1471
250	50	50	3	150	0.371	0.373	0.956	0.960	1214	1218
500	50	50	4	200	0.405	0.409	0.964	0.967	2104	2105
1000	50	50	4	0	0.412	0.416	0.958	0.958	2152	2149
250	100	100	5	50	0.380	0.379	0.951	0.952	2436	2435
500	100	100	5	100	0.381	0.382	0.961	0.962	2833	2832
1000	100	100	6	150	0.396	0.398	0.969	0.971	4571	4559
250	10	25	6	200	0.490	0.492	0.948	0.952	3257	3229
500	10	25	7	0	0.495	0.497	0.952	0.952	4225	4115
1000	10	25	7	50	0.487	0.492	0.955	0.957	5124	4868
250	50	50	8	100	0.462	0.460	0.945	0.947	5309	5272
500	50	50	8	150	0.461	0.460	0.957	0.962	5878	5802
16-bit bus: wire width 300 nm, wire distance 400 nm, wire thickness 319 nm										
250	10	25	2	0	0.144	0.160	0.915	0.915	134	144
500	10	25	2	50	0.130	0.142	0.943	0.952	299	306
1000	10	25	3	100	0.134	0.140	0.965	0.969	686	694
250	50	50	3	150	0.122	0.108	0.962	0.962	710	718
500	50	50	4	200	0.127	0.126	0.969	0.967	1120	1127
1000	50	50	4	0	0.127	0.131	0.964	0.964	708	718
250	100	100	5	50	0.120	0.125	0.947	0.947	906	917
500	100	100	5	100	0.120	0.124	0.960	0.960	1171	1181
1000	100	100	6	150	0.124	0.127	0.971	0.972	1895	1905
250	10	25	6	200	0.152	0.153	0.948	0.954	1460	1467
500	10	25	7	0	0.153	0.158	0.936	0.936	1422	1422
1000	10	25	7	50	0.148	0.152	0.957	0.962	1874	1852
250	50	50	8	100	0.146	0.141	0.936	0.946	1890	1899
500	50	50	8	150	0.144	0.147	0.952	0.960	2261	2265

crosstalk noise in a 2 mm 32-bit bus. The wires were 1.2 μm wide and 0.319 μm thick. The rise time was 100 ps. The separation distance between the wires was varied at 0.4 μm intervals from 0.4 μm to 2.4 μm. Skewing was applied to the bus with the interval T_{int} time varying from 0 to 250 ps. Four different skewing times were used. The RLC matrices were extracted using field solvers for each separation distance, and the maximum crosstalk noise was calculated with the model for each case. To obtain the maximum crosstalk voltage, the closest wires on both sides of the quiet victim were switching up to maximize capacitive crosstalk noise, while wires farther away were switching down to maximize inductive crosstalk noise. The maximum crosstalk noise with no skewing and a separation distance of 0.4 μm was 0.20 V. Since the wires were wide with a low per-unit-length resistance and ground capacitance dominating coupling capacitance, the majority of crosstalk noise was caused by inductive coupling. Of the maximum crosstalk noise of 0.20 V, only 0.05 V was found to be caused by capacitive coupling by setting the inductive coupling terms to zero.

Fig. 5.4 shows that by increasing the separation distance between wires, while keeping the wire properties otherwise unaltered, the noise was reduced. The results gained from the increased wire separation were however the largest initially, with less reduction in noise from large wire separation distances. As can be seen, skewing was capable of reducing even the inductive noise. With an interval time of 250 ps, the maximum crosstalk noise was reduced to 0.05 V. Further increases in the interval time would not have yielded more reduction in crosstalk noise since the aggressor waveforms induced on the victim were not overlapping any more. It is possible to use skewing together with increased wire separation distance according to available system resources such as routing area and timing slack. For example, as seen in the figure, the maximum noise could be reduced to 0.05 V also with a combination of separation distance of 0.8 μm and interval time of 150 ps.

5.4.2 Reduction of Power Supply Noise using Different Methods

Many different methods may be applied to mitigate power supply noise. In this section, the applicability of the model to such analysis is demonstrated and skewing is compared to other methods. The analysis was performed for a square 10 $\times$10 power distribution grid with a segment length of 100 μm. Two 16-bit buses were placed in the grid. The nodes were numbered as in Fig. 4.5. The driver end of the first bus was placed at node 25, while the driver end of the second bus was at node 58. The bus at node 25 was 2 mm long, while the bus at node 58 was 4 mm long. Both buses had a wire width of 300 nm and a wire separation distance of 400 nm. The rise time of the drivers was 50 ps. The power grid wires were 1 μm wide and the corner nodes of the grid, i.e. nodes 1,10,91 and 100, had a constant operating voltage simulating connections to package pins. The resulting worst case drop in the operating voltage due to the switching buses was calculated with the model and is illustrated in Fig. 5.5. The average noise in the power grid nodes was 53.2 mV.

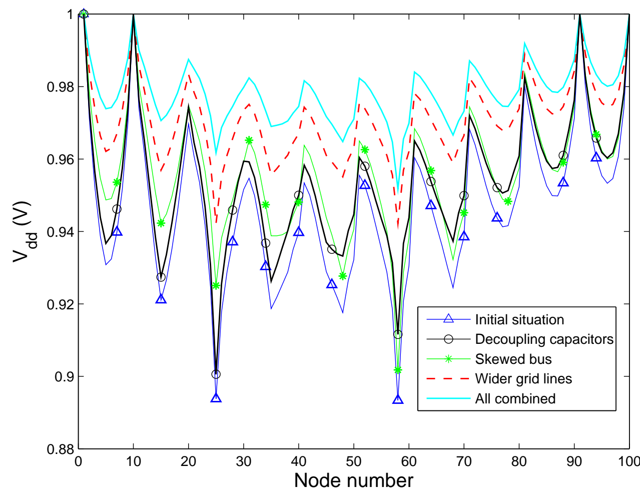

Figure 5.5: The effects of different power distribution noise reduction methods.

The difference in maximum propagation delay between the 2 mm and 4 mm buses was 400 ps. Assuming that both buses operate under the same clock, there is slack available in the shorter bus to apply bus skewing. The available slack was used for skewing the shorter bus with four different skewing times. This reduced power distribution noise in the vicinity of the 2 mm bus as seen in Figure 5.5. The average noise in the grid nodes was reduced by 9.8 mV.

Since there was no slack available for the longer bus, power distribution noise caused by it was reduced with decoupling capacitors. Two 10 pF decoupling capacitors were placed at nodes 59 and 48, which reduced noise in the nodes close to the 4 mm bus. The average noise reduction was 7.0 mV. The effect of power grid lines was analyzed by increasing the power grid line width from 1 μm to 2 μm. This resulted in a considerable overall reduction in power distribution noise of 24.1 mV, albeit at a high cost in circuit area. Finally all methods were applied together. The reduction in average noise was 31.5 mV, and the worst case operating voltage was in all nodes, including the hotspots, 0.95 V or more.

5.4.3 Implementation and Reduction of Crosstalk using Different Methods

In order to apply the skewing method, delays need to be inserted into most of the lines. A common way to create a delay is a straightforward inverter chain. Intentional delays for buses have previously been implemented as additional wire doglegs [113], or with flipflops with adjustable dynamic delays [107]. For the method here, static delays are needed and they were implemented using

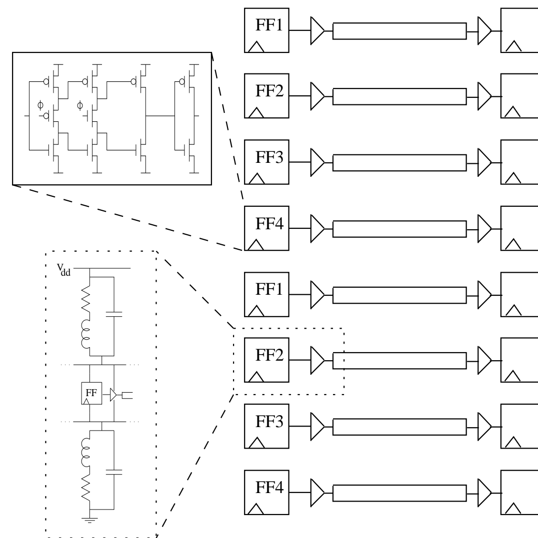

Figure 5.6: Implementation of skewed bus. The driver side flipflops numbered 2-4 are delayed. The dotted area in the lower left corner shows the implementation of the power and ground lines used in the HSPICE analysis.

delayed, precharacterized flipflops. The delay was achieved by adjusting the flipflop transistor sizes. Implementation of the skewed bus using four skewing times is shown in Fig. 5.6. It should be noted that while process variations can affect timing, the skewing is applied to neighboring gates that typically have a strong spatial correlation, thus limiting the effect on the relative delays between the lines.

The skewing was implemented using 65 nm technology. In order to determine the influence of mismatch and power noise on the relative delays, the flipflops and drivers were simulated with HSPICE using mismatch technology library and noisy power and ground rails. The outputs of the flipflops and drivers are shown in Fig. 5.7. As can be seen, the different delays are clearly distinguishable. In order to avoid significant changes in driver rise/fall times, the output transistors of the flipflops were not altered, although this would have provided more delay. The 20%–80% risetimes of the skewed drivers remained between 48 ps and 58 ps. If in smaller technologies flipflop adjustments are not sufficient, simple inverter chains could be used instead or in combination with the delayed flipflops.

The skewing method was also implemented together with other typical cross-talk reduction methods, namely shielding and increased wire separation distance. A 2 mm long 8-bit bus was used. The drivers were 40x inverters and receivers 10x inverters. In order to rapidly simulate the power supply noise caused by the switching bus drivers on the power supply network, the power and ground rails were modeled as in [91]. The resistance, capacitance and in-

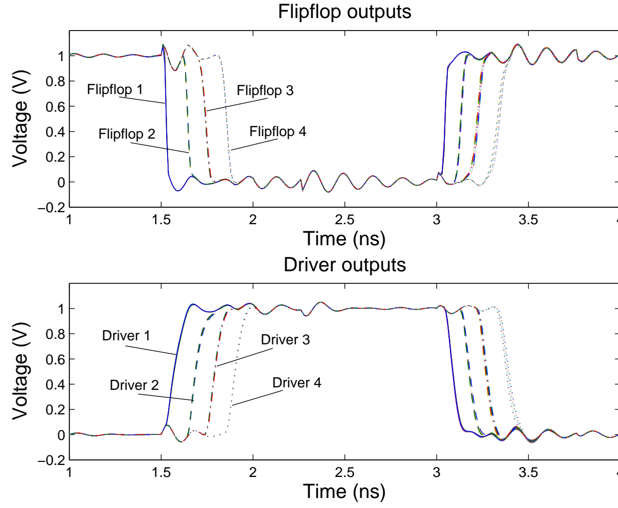

Figure 5.7: Skewed flipflop and driver outputs under mismatch and noisy power and ground rails. Interval time is 100 ps and operating temperature 75C.

ductance of the power and ground rails shown in Fig. 5.6 were 2 Ω, 0.2 pF and 2 nH, respectively.

The simulation results are shown in Table 5.2. The results for using the proposed skewing method alone are shown in the first section. When the interval time T_{int} was zero, the bus acted as a regular bus. As can be seen, the maximum crosstalk noise was reduced from 0.63 V to 0.50 V when the interval time was increased to 100 ps. Since the drivers switched at different times, the load on the power rails was also reduced. The original worst case V_{dd} was improved from 0.90 V to 0.95 V with a 100 ps interval time, thus effectively halving the power supply noise. The energy required to transmit a byte across the 8-bit bus was obtained as the average of all possible switching combinations (up, down, quiet). As can be seen, the delayed flipflops increased the energy consumption slightly by 0.6%. The average energy consumption of the wires themselves did not change when skewing was applied. This was due to the Miller coupling factor that increased for wires switching in the same direction and decreased for wires switching in opposite directions when skewing was increased, thus canceling each other. Further analysis of bus energy consumption under delayed inputs can be found in [107].

The second section of the table shows the results for the combined use of skewing and shield wires. Shield wires were inserted between signal wires. The area of the bus was consequently doubled. The shielding alone effectively reduced crosstalk from 0.63 V to 0.08 V. Use of skewing helped to reduce the crosstalk noise further to 0.03 V. Shielding had no improvement on the worst

Table 5.2: HSPICE simulation results for the skewing method alone and in combination with shielding and increased wire separation distance

T_{int} (ps)	Max. crosstalk (V)	Worst case V_{dd} (V)	Avg. energy/byte (pJ)	Peak power (mW)
Skewing only				
0	0.63	0.90	0.988	5.14
15	0.62	0.91	0.989	5.22
50	0.59	0.94	0.990	4.85
100	0.50	0.95	0.994	4.19
Combination of skewing and shielding				
0	0.08	0.89	0.988	4.59
15	0.06	0.90	0.988	4.45
50	0.05	0.94	0.989	4.03
100	0.03	0.96	0.993	3.14
Combination of skewing and increased wire separation distance				
0	0.34	0.89	0.513	3.98
15	0.33	0.90	0.514	3.92
50	0.30	0.94	0.514	3.36
100	0.25	0.96	0.519	2.72

case operating voltage, but it was again effectively improved with the skewing method to 0.96 V.

The third section of the table shows the same area-doubled bus with the shield wires removed, so that there is an increased separation distance between the signal wires. Increasing the separation distance was not as efficient in reducing crosstalk noise as shielding, as the crosstalk noise was reduced from 0.63 V to 0.34 V. The dissipated energy was however clearly lower, since the total capacitance of wires was smaller due to the increased separation distance between them. When skewing was added the crosstalk noise was further reduced from 0.34 V to 0.25 V. The increased wire separation distance had no effect on the worst case operating voltage, while skewing improved it to 0.96 V as previously. The increase in average energy consumption due to skewing was 1.2%.

The use of shield wires was the most effective method in reducing crosstalk noise, although at the cost of a doubled bus area. Doubling the bus area and using it for increasing the wire separation distance was less effective in crosstalk reduction, but the average dissipated energy was clearly lower. The skewing method did not require an increase in the bus area besides the resizing of the flipflops, and it was the only one to improve power supply noise, but the propagation delay was increased instead. The bus was skewed using four different skewing times for the drivers, i.e. the maximum skewing time was $3 \times T_{int}$. The maximum propagation delay occurred when the drivers were switching in opposite directions to maximize the influence of crosstalk, while the minimum delay occurred when drivers were switching in the same direction. Skewing of the drivers caused the correlation between the switching events to reduce,

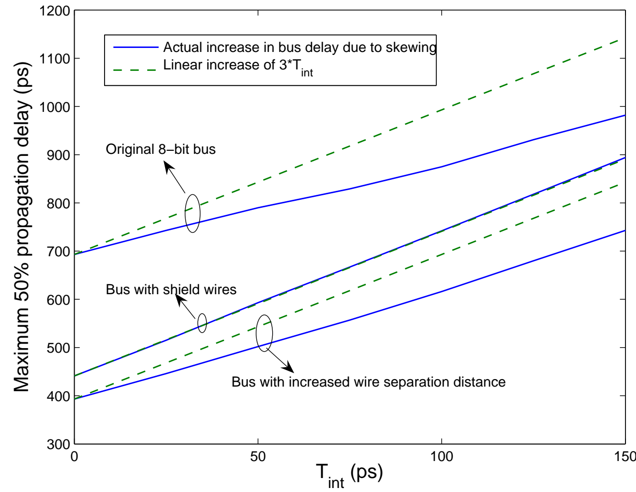

Figure 5.8: Worst-case propagation delays as a function of interval time for three different bus structures; normal bus, bus with shield wires, and a bus with increased separation distance between wires.

thus altering the Miller capacitance. Because of this, the overall increase in the propagation delay of the bus was less than or equal to $3 \times T_{int}$.

The change in the propagation delay of the analyzed 8-bit bus is shown in Figure 5.8. The delays are shown as a function of interval time for the original bus with skewing, the bus with shield wires and skewing, and the bus with increased separation distance and skewing. The dashed lines show the theoretical maximum propagation delay due to the applied skewing, that is, an increase of $3 \times T_{int}$, while the solid lines show the actual delay. The difference between the two is largest for the original bus, which had the largest coupling between signal wires, while for the shielded bus the lines are nearly identical since there is very little coupling between the signal wires. The total performance penalty depends on how much timing slack there is available for the bus or the use of techniques such as a multicycle time-borrowing bus. In some cases skewing can be applied to even reduce the overall propagation delay [105]. The presented model can be applied in the analysis to calculate the propagation delay of the bus under skewing.

5.4.4 Influence of the Number of Skewing Times

The maximum crosstalk noise and power supply noise do not depend solely on the interval time, but also on the number of different skewing times. It is possible to apply the bus and power grid model to any number of different skewing times.

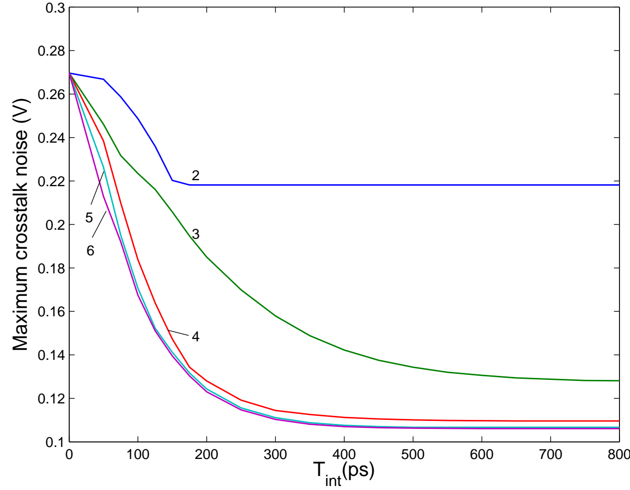

Figure 5.9: Maximum crosstalk noise as a function of interval time using 2-6 different skewing times in a 1-mm 32-bit bus.

The minimum number of different skewing times is one, in which case all drivers switch simultaneously as normal. On the other hand, the maximum number of different skewing times is equal to the number of wires, in which case all drivers switch at a different time. The effect of the number of skewing times on the maximum crosstalk voltage on a quiet wire in a 1 mm 32-bit bus was calculated using the model and is shown in Fig. 5.9.

The bus wires were 145 nm thick with equal separation distance and a rise time of 100 ps and source resistance of 200 Ω. As can be seen, an increase in the number of skewing times helped to further reduce crosstalk noise, although after four or more skewing times the effectiveness was reduced. The reason for this can be seen from Fig. 5.1. As can be seen from the figure, when three or more skewing times are used, the neighboring two aggressors on both sides of any victim wire do not switch at the same time, instead there is a time of at least T_{int} between them. When the number of skewing times is increased to four, the time between the two aggressors switching is increased to $2T_{int}$, helping to further reduce crosstalk voltage. When the number of skewing times is increased to five or six, the time between the two closest aggressors in the worst case remains at $2T_{int}$, and the slight reduction in maximum crosstalk over four skewing times seen in Fig. 5.9 is gained from aggressors farther away.

In Fig. 5.10 is shown the worst case operating voltage as a function of interval time caused by the same 1-mm 32-bit bus. The bus was located in a power grid with 1 μm wide power wires. Power was supplied from the corners of the grid and all drivers were switching from low to high. The number of different

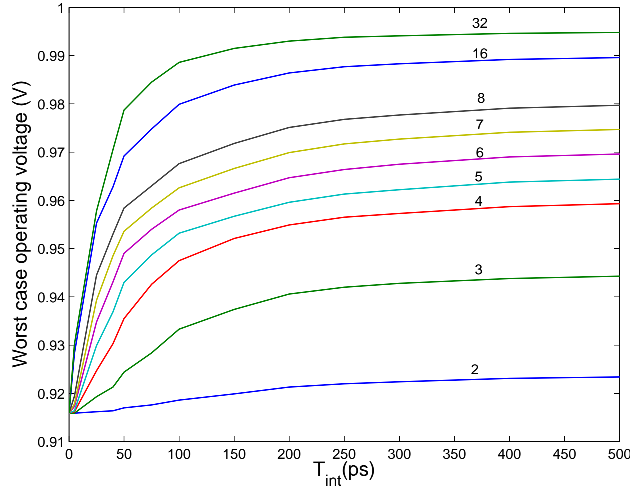

Figure 5.10: Worst case operating voltage caused by a 1-mm 32-bit bus as a function of interval time using 2-8, 16 and 32 different skewing times.

skewing times used was 2-8, 16 and 32. The results were calculated with the model. The power supply noise caused by the bus was reduced as the number of skewing times was increased. This was due to the reduction in the number of drivers switching simultaneously. For example, with two skewing times half of the drivers, i.e. 16, switched simultaneously, while with eight skewing times the number was reduced to four. The lowest noise was achieved with 32 skewing times, when all drivers switched at different times. In this case the total delay however becomes impractically large, and the implementation of 32 different delays is also problematic. Four different skewing times could be seen as a reasonable compromise that also yielded an efficient reduction in crosstalk noise seen in Fig. 5.9.

5.5 Chapter Summary

In this chapter, an optimization method based on analytical RLC models was proposed for simultaneous reduction both of functional crosstalk noise and power supply noise caused by on-chip buses. The reduction was achieved with skewing that does not require additional encoding/decoding circuitry or extra wires, but instead acts mainly as a trade-off between time and noise. The static delays were implemented using resized flipflops. This makes the method well suited for area limited cases. The modeling of the bus crosstalk noise and propagation delay and the power supply noise caused by the bus make it possible to find a suitable value for the skewing time in the trade-off process. The model is

applicable to any number of bus wires and takes into account both capacitive and inductive coupling between wires. The reduction in power supply noise due to skewing in the surrounding RLC power grid was also included in the model. The model was verified by comparing it to HSPICE in 65 nm technology. The average error was 1.4%.

The method was found to be effective in reducing problematic long range inductive crosstalk noise in a case study where the maximum crosstalk noise in an inductance dominated bus was reduced from 0.20 V to 0.05 V. Since the data or bus layout are not changed, the proposed method can be applied individually or together with other methods depending on area and timing constraints to reach targeted crosstalk noise values. The skewing method was implemented together with shielding and increased wire separation distance in 65 nm technology. HSPICE simulations showed an increase in bus energy dissipation due to skewing of less than 1.2%. Skewing was capable of further reducing the functional crosstalk noise levels achieved with the other methods, while also being able to reduce the worst case power supply noise from 0.1 V to 0.05 V. The reduction in power supply noise in a power grid was compared to decoupling capacitors and double-width power lines. Skewing using a 400 ps slack reduced the original average power supply noise of 53.2 mV by 9.8 mV, while for two 10 pF decoupling capacitors the reduction was 7.0 mV and for the wide power grid lines 24.1 mV. When skewing was used together with the two other methods the reduction in power supply noise was 31.5 mV. The influence of different number of skewing times was studied, where four different skewing times was found to be a reasonable compromise between the total delay and implementation complexity and the reduction in functional crosstalk and power supply noise.

Chapter 6

Modeling of Process Variation Effects in Encoded Signaling

Previously, two noise sources on buses, crosstalk and intersymbol interference, were modeled and analyzed. The performance of a bus can also be affected by another source, i.e. process variation. This variation affects both devices and interconnects. On-chip buses are often driven and buffered with simple inverters. However, in recent years, due to increasing delay, power and signal integrity problems, bus encoding has been proposed to alleviate these issues [114, 115, 116, 117]. In bus encoding, there is additional logic that is used to encode the input signals to the bus and decode them at the receiver end. This logic is susceptible to process variation.

The devices are affected by e.g. variation in effective channel length, oxide thickness, dopant concentration and threshold voltage [118], while the interconnects are affected by thickness and width variation due to the copper damascene chemical mechanical polishing (CMP) process and interference in lithography [119]. CMP is used to planarize the interconnect or inter-layer dielectric between adjacent metal layers, while the damascene CMP process is used with copper interconnects to polish the deposited metal. This polishing results in variation in wire thickness due to differences in wire densities across the die [120]. In lithography, the main sources of process variation are focus, exposure dose and mask variations [121].

In this chapter, a model for analyzing signaling over an on-chip bus consisting of encoding circuitry, drivers, transmission lines, receivers and decoding circuitry is proposed [122]. The wires are modeled as capacitively and inductively coupled distributed RLC transmission lines. The driving point effective capacitance for a bus driver is derived for the decoupling method. The delay of the signaling circuitry and rise time of the drivers are characterized as a function of the load capacitance. The effects of process variation are taken into account in both

the characterization of the signaling circuitry and in the wire analysis. The overall delay variation of the bus due to process variation is then calculated. This combination of analytical interconnect models and characterized logic can be used to speed up statistical Monte Carlo simulations to analyze the effects of process variation. The model is verified by comparing it to HSPICE. The derived model is applied to analyze regular voltage mode, level-encoded dual-rail (LEDR), and 1-of-4 signaling. The implementation and analysis are done in 45 nm technology.

6.1 Bus Model

The bus structure considered in this chapter is shown in Fig. 6.1. The bus consists of a number of input signals that are encoded and sent using voltage-mode signaling over an arbitrary number n wires to the receivers and decoder. The total delay of the bus includes the delay of possible encoding circuitry, drivers, wires, receivers, and possible decoding circuitry. Changes in the physical properties of a wire caused by process variation also affect its electrical properties, i.e. resistance, inductance and capacitance. The interaction between a driver and an interconnect with varying electrical properties can be modeled by empirically precharacterizing the driver delays and rise times as a function of load capacitance and input rise time. Circuit simulators such as SPICE can be used in this characterization of non-linear devices. The interconnect can then be analyzed by modeling the driver as a voltage source with the delay and rise times corresponding to the load. The load to a driver has traditionally been modeled as the total capacitance of an interconnect. Because of the scaling of the interconnect sizes, the actual load seen by a driver is smaller due to resistive and inductive shielding [123]. An RC [63] or RLC [124] input admittance can be mapped to a such effective capacitance in order to maintain compatibility with the existing efficient empirical driver models. In moment matching methods such as AWE [22], the input admittance models for the driving points are generated at the same time as the approximate transfer functions. In this section, the effective capacitance is derived instead for the decoupling method that is used in this thesis.

In general, the delay t_d of a driver and the rise time t_r of its output are a function of the load capacitance and the rise time of its input, i.e. $t_d = f(t_r^{in}, C_{load})$ and $t_r = g(t_r^{in}, C_{load})$. The driver output waveform is modeled as a saturated ramp as shown in Fig. 6.2. The encoder and driver were characterized with HSPICE by determining their rise time t_r and delay t_d from the encoder input to the driver output as a function of load capacitance. In order to simplify the characterization without loss of generality, it is assumed that the rise time t_r^{in} of the encoder input signals is constant. In order to connect the encoder and driver characterization with the bus model, the the driving point effective capacitance seen by the drivers is derived. The circuit model of the bus is shown in Fig. 6.3.

The bus consists of n wires of length h with inductive and capacitive coupling

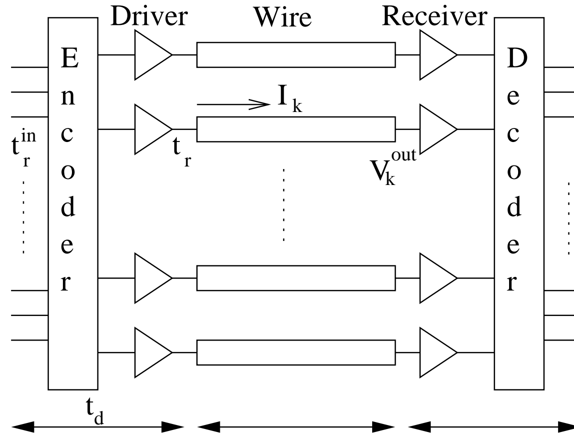

Figure 6.1: Bus implementation with encoding and decoding.

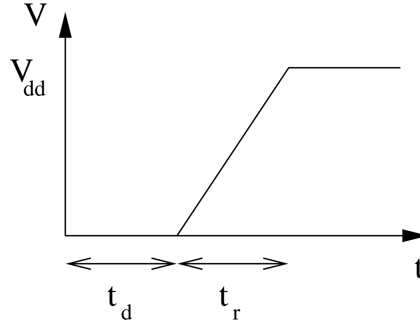

Figure 6.2: The saturated ramp model of the driver output waveform.

between them. The wires were modeled as distributed RLC transmission lines. The bus is driven by the saturated ramp voltage source in Fig. 6.2. C_L is the load capacitance due to the receiver at the end of the wire.
The driver output voltage shown in Fig. 6.2 is in s-domain

$$V_S(s) = \frac{V_{dd}}{t_r s^2}\left(1 - e^{-t_r s}\right). \tag{6.1}$$

In Chapter 4, the current flowing into a transmission line using a driver mapped to linear circuit components was derived as (4.10). We apply it here to a precharacterized driver instead in order to evaluate the effects of device process variation. The equation can then be written as

$$\frac{I_s}{V_s} = \frac{Z_L a_{21} + a_{22}}{(a_{11} + R_S a_{21})Z_L + a_{12} + R_S a_{22}}. \tag{6.2}$$

It should be noted that the value of R_S is different from the one in Chapter 4, and its use is here optional as explained later. By combining (6.1) with (6.2)

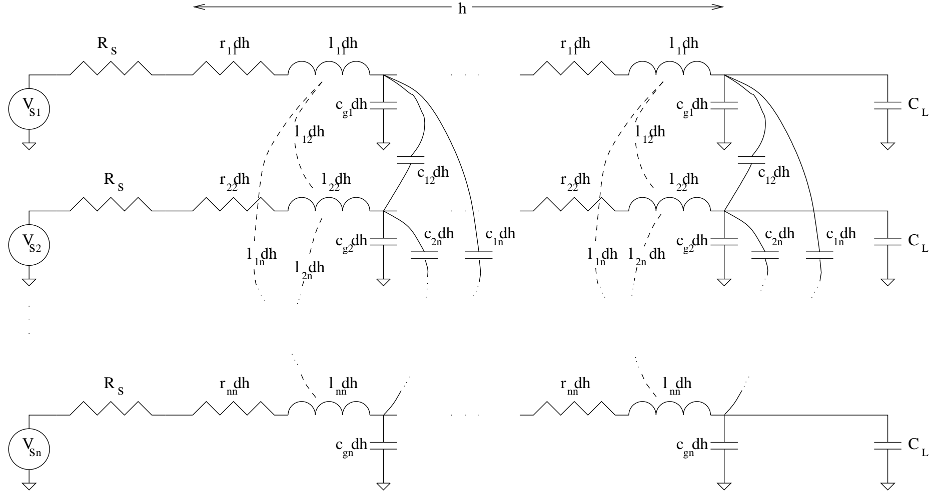

Figure 6.3: Circuit model of the bus.

and (2.20), and applying (2.10), the current I_k flowing into the k-th wire in a bus consisting of n wires can the be derived as

$$I_k(t) = \sum_{i=1}^{n} \mathbf{M}_{ki} \sum_{j=1}^{n} \mathbf{M}_{ij}^T I_i(t) \tag{6.3}$$

where

$$\begin{aligned} I_i(t) = \textstyle\sum_{p=1}^{m-1} A_p e^{s_p t} + A_m e^{s_m t} - \\ \left(\textstyle\sum_{p=1}^{m-1} A_p e^{s_p (t-tr)} + A_m e^{s_m (t-tr)} \right) u(t-tr) \end{aligned} \tag{6.4}$$

where m is the order of the terms included in the derivation and $u(t)$ is the unit step function. The current I_i is calculated using the diagonalized resistance, capacitance and inductance values of $\hat{R}_{ii}$, $\hat{C}_{ii}$ and $\hat{L}_{ii}$, respectively. The effective capacitance seen by a driver was calculated by equating the average currents drawn by the interconnect I_k and the effective capacitance I_C over a time interval τ up to the 50% delay point, as proposed in [63]

$$\frac{1}{\tau} \int_0^{\tau} I_k(t) dt = \frac{1}{\tau} \int_0^{\tau} I_C(t) dt. \tag{6.5}$$

The initial rise time t_r and delay t_d were set according to the total capacitance of the wire, and the effective capacitance seen by the driver was then acquired iteratively using (6.5). In practice three to five iterations were needed for the effective capacitance to converge. In order to determine the propagation

delay of the interconnects, (5.3) is used. By using (2.20) and (2.9), the far-end voltage of the k-th wire in an n-bit bus is

$$V_k^{out}(t) = \sum_{i=1}^{n} \mathbf{M}_{ki} \sum_{j=1}^{n} \mathbf{M}_{ij}^T V_i(t) \tag{6.6}$$

where V_i is obtained by substituting (6.1) into (5.3) and using partial fraction expansion and inverse Laplace transform

$$\begin{aligned} V_i(t) = \textstyle\sum_{p=1}^{m-2} B_p e^{s_p t} + B_{m-1}t + B_m - \big(\textstyle\sum_{p=1}^{m-2} \\ B_p e^{s_p(t-t_r)} + B_{m-1}(t-t_r) + B_m \big) u(t-t_r). \end{aligned} \tag{6.7}$$

Possible non-switching bus drivers are not included in the summations of (6.6) and (6.3), while downward switching is included with a minus sign. The RLC transmission line matrices of the interconnects were extracted using analytical equations from [125] in order to rapidly evaluate the influence of different wire properties. The cross-section view of the wire configuration is shown in Fig. 6.4. The wires run parallel to each other over a ground plane.

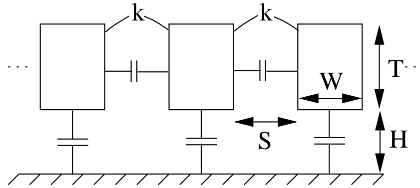

Figure 6.4: Cross-section view of wire configuration.

6.2 Signaling Techniques

The model is applied to two different asynchronous signaling techniques, namely level-encoded two-phase dual-rail encoding (LEDR) [126] and two-phase 1-of-4 encoding [127]. In the asynchronous design approach, no global clock is used and synchronization is applied instead. Two-phase or nonreturn-to-zero handshaking uses signal transitions to assert data validity and reception. Two-phase handshaking is preferred for long interconnects since it uses half of the number of transitions of four-phase or return-to-zero handshaking.

The benefits of LEDR signaling include improved throughput and power since it requires no reset phase and since only one transition occurs on a wire per data bit transmission [128]. LEDR uses two wires to encode one bit of data. One of the wires is the data wire which holds the bit value in standard single wire encoding while the other wire indicates phase by its parity relative to the data wire. The encoding in LEDR alternates between odd and even phases. The encoding of a bit 1 is 01 in odd phases or 11 in even phases while the encoding of a bit 0 is 10 in odd phases and 00 in even phases. This is illustrated in Fig. 6.5.

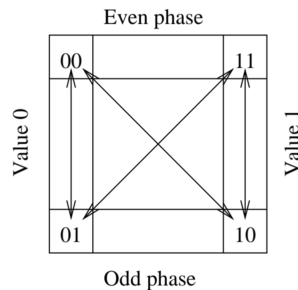

Figure 6.5: LEDR codeword transitions.

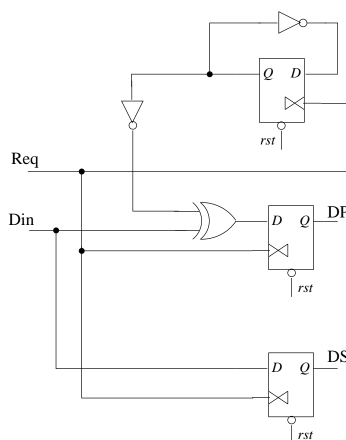

Figure 6.6: LEDR encoder implementation.

The encoder used in the analysis is shown in Fig. 6.6. The encoder takes the request and data bits in single-rail encoding and converts them into LEDR encoding [122]. An inverter was used as both driver and receiver in this signaling. In LEDR signaling the decoded data is obtained directly from the output of the data wire. The completion detection for N wires was performed with a C-element as shown in Fig. 6.7.

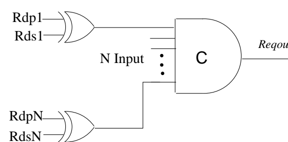

Figure 6.7: LEDR completion detector implementation.

1-of-4 encoding uses a group of four wires to transmit two bits of information per symbol. A symbol is one of the two-bit codes 00, 01, 10 or 11 and is transmitted through activity on one of the wires. 1-of-4 encoding is therefore

less sensitive to crosstalk than single-line encoding. The straightforward implementation of the encoder is shown in Fig. 6.8. An inverter was used as both driver and receiver also in this signaling. The decoder and completion detector implementation are shown in Fig. 6.9. The gates and latches were used to decode the data back into single-line form while the C-element was used again for completion detection.

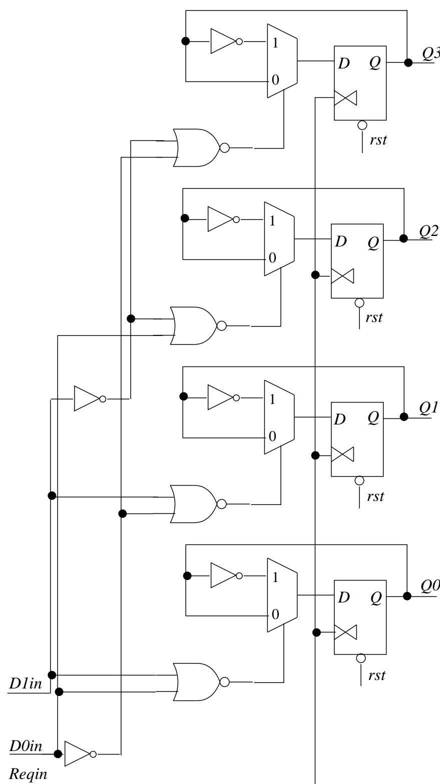

Figure 6.8: 1-of-4 encoder implementation.

6.3 Verification and Case Study

Channel length and threshold voltage are seen as the most important device variation sources, while effective mobility is also emerging as an additional key variation source [129]. The focus of the transistor process variation analysis in this Chapter is on threshold voltage variation, although it can be performed similarly also for other sources. The dependence of the delay and rise time of each signaling circuitry on load capacitance was characterized using HSPICE. The HSPICE transistor models for 45 nm technology were obtained using Predictive Technology Model [130]. The characterizations were done for each variation in

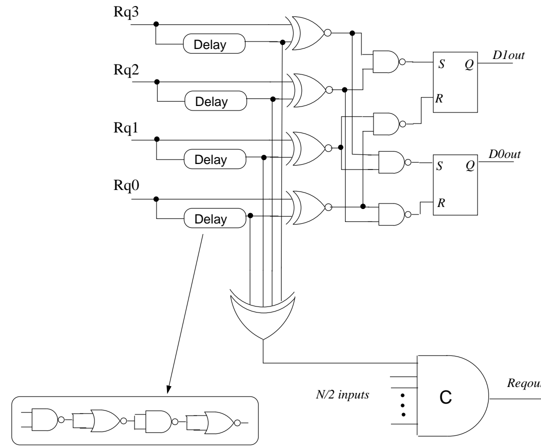

Figure 6.9: 1-of-4 decoder implementation.

the threshold voltage. In addition to the normal 0.18 V threshold voltage also 0.15 V and 0.21 V were used. Fig. 6.10 demonstrates the rise time t_r of the LEDR encoder and driver as a function of load capacitance. The 50% delay t_d of the LEDR encoder and driver are shown in Fig. 6.11. The curve-fitted results were used in the effective capacitance calculations in the model. Regular voltage mode and 1-of-4 signaling circuits were characterized in a similar manner. A change in the physical properties of a wire, e.g. width or thickness due to process variation, also caused the effective capacitance to change. Due to the precharacterization of encoding circuitry as a function of load capacitance, all changes in wire properties could be analyzed analytically instead of using SPICE.

The voltage waveforms obtained with the model for driver output and wire far-end are compared to HSPICE in Fig. 6.12 and in Fig. 6.13. The comparison was performed for a 16-bit bus. The wire in the middle of the bus was used in the analysis. The results are shown for regular voltage mode signaling, where the driver was a 200x inverter and the receiver was a 20x inverter. The receiving inverter was modeled in the model as a capacitive load C_L at the end of the wire, and this capacitance was extracted with HSPICE. In the first case, the comparison was performed for a 1 mm long bus where the wire width W and separation distance S were set to 68 nm as approximated in the ITRS roadmap for minimum global wiring pitch in 45 nm technology. The comparison was also performed for a longer 3 mm long bus where wire width and separation distance were 135 nm. The wire thickness T and distance to ground H were in both cases 162 nm. The input signal t_r^{in} to the driver inverter was a falling ramp with a 50 ps fall time as shown in the figures. The model and HSPICE results were close to each other. The propagation delay of the wire was slightly underestimated since the saturated ramp did not accurately capture the exponential tail of the driver output. If needed the exponential tail can be modeled with a source

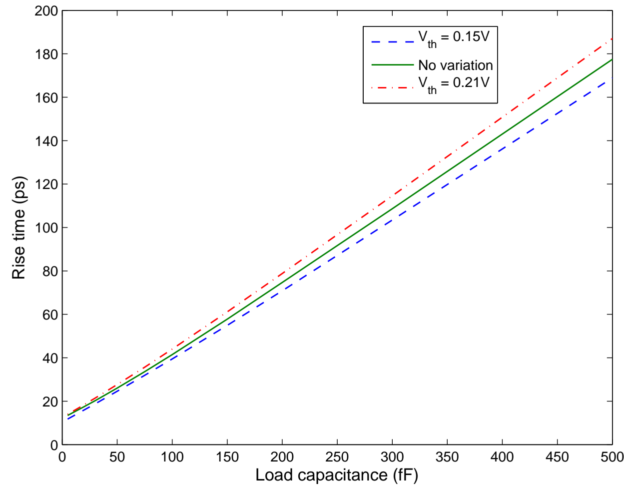

Figure 6.10: The rise time of the LEDR encoder and driver as a function of load capacitance with different transistor threshold voltages.

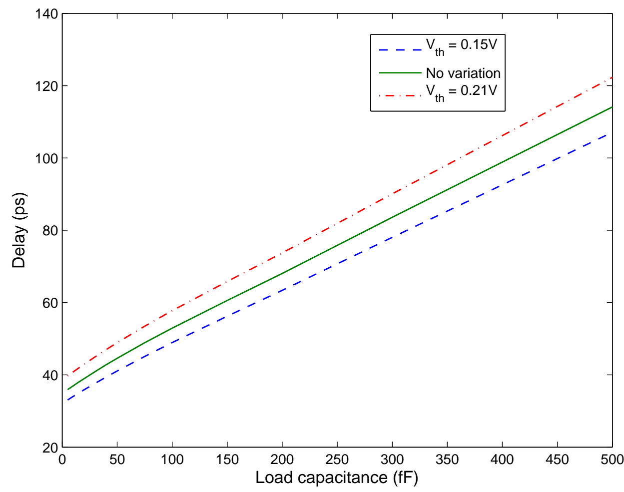

Figure 6.11: 50% delay of the LEDR encoder and driver as a function of load capacitance with different transistor threshold voltages.

resistor as in [63].

The total delay variation of the bus was obtained by adding the delay of the receiver and decoder to the 50% delay at the far-end of the wire. The receiver and decoder delay was also characterized with HSPICE for different threshold voltages. Table 6.1 shows the amount of delay variation in the 16-bit bus for different signaling techniques. The delay variation was calculated as the difference between the delay acquired in the presence of process variation and the delay acquired without process variation. All signaling techniques had a 200x inverter as a driver and a 20x inverter as the receiver. The length of the bus was 3 mm and the wire width and separation distance were 135 nm. The data to the encoders consisted of all inputs switching. For LEDR and 1-of-4 signaling the 16-bit bus was encoded into 32 wires. The regular voltage mode signaling had no encoding or decoding circuitry. As shown in the table, the model was further verified by comparing the delay variation obtained with HSPICE and the model. The delay variation was accurately modeled. The first part of the table shows the delay variation due to threshold voltage variation. A lower threshold voltage decreased the delay of the bus while a higher voltage increased it. The second part of the table shows the delay variation when only the wire properties vary. It was assumed that the wire pitch remains constant while the wire width varied. As can be seen, for regular voltage mode signaling the effect of wire variation on bus delay was clearly larger than the effects of device variation. On the other hand, the LEDR and 1-of-4 signaling techniques suffered more delay variation from transistor variation due to their encoding and decoding circuitry. The third part of the table shows the delay variation when both the threshold voltage and wire properties vary simultaneously.

Table 6.1: The total delay variation of the bus for different signaling techniques

	Regular		LEDR	1-of-4
Variation source	Model	HSPICE	Model	Model
V_{th} = 0.15V	-2.2ps	-2.7ps	-28.8ps	-40.2ps
V_{th} = 0.21V	+3.4ps	+3.6ps	+34ps	+50.7ps
Wire width -10%	+27.6ps	+27.3ps	+34ps	+31ps
Wire width +10%	-22.7ps	-21.9ps	-26ps	-21ps
Wire thickn. -10%	+54.3ps	+55.4ps	+68ps	+63ps
0.15V, width+10%	-25.1ps	-24.7ps	-53.9ps	-61.2ps
0.21V, thickn.-10%	+57.7ps	+58.9ps	+103ps	+115ps

The presented analytical model was also applied to demonstrate its use in analyzing the statistical effects of wire variation. Conventional deterministic static timing analysis (STA) is today often seen as inadequate due to the rising importance of process variation. In STA, process variation is modeled by running the analysis multiple times for different process conditions thus creating the so-called corner files [131]. The number of corner files and simulation time increases rapidly as the number of variation sources increases. Also, STA

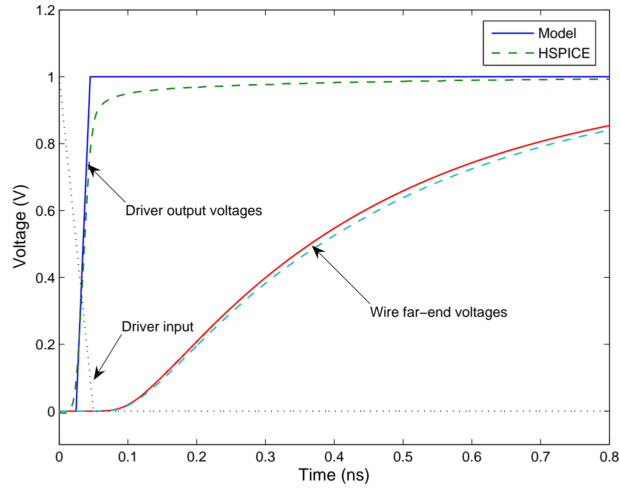

Figure 6.12: Comparison between HSPICE and the model for driver output voltages and wire far-end voltages in a 16-bit 3 mm bus. Wire width and separation distance are 135 nm.

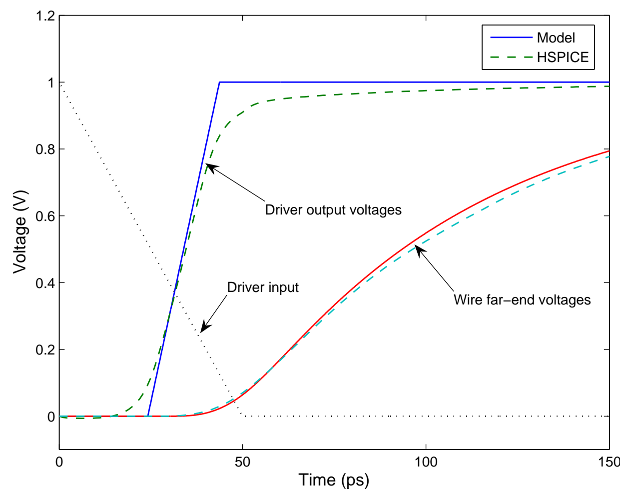

Figure 6.13: Comparison between HSPICE and the model for driver output voltages and wire far-end voltages in a 16-bit 1 mm bus. Wire width and separation distance are 68 nm.

can not accurately model within-die variations. To overcome these limitations, statistical static timing analysis (SSTA) has been proposed. In probabilistic SSTA [132], signal delays are treated as random variables or probability distribution functions and propagated by performing statistical sum and maximum operations. In Monte Carlo SSTA [133, 134], statistical samples are generated with conventional STA methods to obtain the delay distribution. In this chapter, Monte Carlo analysis was used to analyze the delay variation since the presented model enables fast calculation of samples. Fig. 6.14 shows the delay variation of the bus for different signaling techniques when the wire width varies. The wire width was varied with a 3-sigma variation of 10% so that the wire pitch remained constant. The Monte Carlo analysis was done with 1000 samples.

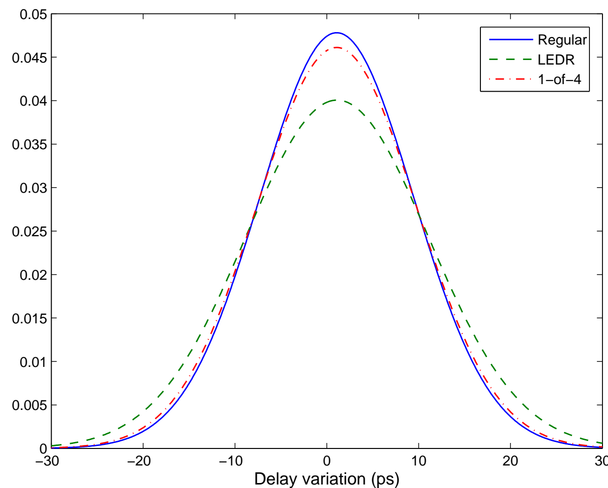

Figure 6.14: Bus propagation delay variation due to wire width variation in regular, LEDR and 1-of-4 signaling.

Although the LEDR and 1-of-4 signaling techniques had in general larger delay variation than regular voltage mode signaling, they are able to operate correctly regardless of the delay since they employ delay-insensitivity. The correct operation of regular synchronous voltage mode signaling is however susceptible to delay variation. The proposed model can be applied to evaluate the increase in delay variation caused by encoded signaling and to determine the need for encoding techniques with delay-insensitivity.

6.4 Chapter Summary

In this chapter, a model to analyze the effects of process variation on delay in on-chip bus signaling was developed. The model combined the variation

in signaling circuitry and in the wires to calculate the total delay variation of the bus. The wires were modeled as distributed RLC transmission lines including capacitive and inductive coupling between them. The effective load capacitance was derived for the decoupling method. The signaling circuitry was characterized as a function of its load capacitance. The driver delay and rise time corresponding to the derived effective capacitance were used to calculate the far-end voltage of a transmission line. The effects of process variation were taken into account in the characterization of the signaling circuitry and in the wire analysis. The overall delay variation of the bus due to process variation was then calculated. The model was verified by comparing it to HSPICE. The delay variation of regular voltage mode, level-encoded dual-rail and 1-of-4 signaling was analyzed with the model. The analysis was done in 45 nm technology.

Chapter 7

Energy Modeling in RLC Current-Mode Signaling

In the previous chapter, encoded signaling was addressed. In addition to encoded signaling, there are also other alternative signaling techniques for global interconnects, such as current-mode signaling [12, 135, 136, 137, 138]. In current-mode signaling, the major difference over voltage-mode is the resistive termination at the receiver end, because of which there is not a full voltage swing. In addition, the distributed wire capacitances are not even uniformly charged. Familiar voltage-mode models are not therefore applicable, and accurate and efficient models need to be developed for current-mode signaling for issues such as energy dissipation and propagation delay.

In voltage-mode signaling, the dynamic energy dissipation has traditionally been obtained from the well-known equation $E = CV_{dd}^2$, where C is the total capacitance. Since an increasing portion of energy is dissipated in interconnects, more accurate and extensive models have recently been presented for voltage-mode signaling [139, 140, 141]. The traditional CV_{dd}^2 model fails to predict the energy dissipation in high clock speeds where the signal transients do not settle to a steady-state value [139]. The energy dissipated by wire resistances during the transient switching is also not accurately included [140]. For a lumped RC circuit with a step input, the energy dissipated in the resistor is equal to the energy needed to charge the capacitor, i.e. $(1/2)CV_{dd}^2$. However, in practice an input to a wire has a finite rise time which reduces the resistive energy component. This energy dependence on rise time is intentionally applied in adiabatic charging [142, 143]. In addition, a separate evaluation of the driver and interconnect contributions can be useful to understand the sources of energy dissipation and to analyze local temperature increases [141]. High wire temperatures affect wire delays and electromigration reliability. Global wires are especially susceptible to higher temperatures since they are farthest away from the substrate and the heat sink, and since they are surrounded by low-κ dielectrics that have poor thermal conductivity. Also, due to their large geometries they have a high

ability to retain heat [144].

In [145, 146], models for the dynamic and static power dissipation of an RC current-mode line have been presented. The models do not however include the aforementioned aspects that have been introduced in later voltage-mode energy models. In addition, the inclusion of inductive effects is desirable for today's high speed circuits [141]. The current-mode driver in [145, 146] is modeled using a switch-resistor model. More accurate modeling can however be achieved by characterizing the driver as a function of its load. In voltage-mode signaling, the behavior of a driver is commonly characterized as a function of its capacitive load or effective capacitance [63]. More accurate Π-type circuits for modeling the interconnect load have also been presented [147]. These effective capacitance and Π-models are however not compatible with current-mode signaling since there is no resistive path to ground. In current-mode signaling an accurate representation of the interconnect load is needed since current-mode signaling is typically used for long-range communication where resistive and inductive parasitics are often significant.

In this chapter, a novel analytical model for energy dissipation in RLC current-mode signaling is derived [148]. The energy is derived separately for the driver, wire and receiver termination components. The effects of transient and static resistive power and different rise times and clock cycles are included. A realizable Π-model is derived to model the driving point impedance of an RLC current-mode transmission line. The Π-model is used to characterize the driver and in the energy calculations. The output current of a current-mode RLC transmission line is derived. The modeling is extended to multiple coupled RLC lines with capacitive and inductive coupling between them, and applied to model differential current-mode signaling.

7.1 Current-Mode Driving Point Impedance

In this section, a realizable RLC Π-model for the driving point impedance of a resistively terminated transmission line is derived in order to analyze energy dissipation in current-mode signaling. The model was also used to characterize the drivers. The Π-model parameters are calculated directly from the total interconnect resistance, capacitance, inductance and receiver resistance. Although Π-models introduce more parameters than a simple capacitance model into the characterization process, it should be noted that the total number of gates to characterize is smaller in current-mode signaling since current-mode gates are usually used only for global communication, and not as e.g. logic gates. The driving point impedance Z_{in}^{tl} of a terminated RLC transmission line can be calculated as [149]

$$Z_{in}^{tl} = \frac{a_{11}Z_L + a_{12}}{a_{21}Z_L + a_{22}} \tag{7.1}$$

where Z_L is the load impedance at the end of the line and a are defined in (4.6). h is the length of the line and r, l and c are the resistance, inductance

and capacitance of the line per unit length, respectively. By applying a series expansion to the hyperbolic functions in (7.1), as in (4.12)–(4.14), the driving point impedance can be written as

$$Z_{in}^{tl} = \frac{a_0 + a_1 s + ...}{b_0 + b_1 s + b_2 s^2 + ...} \tag{7.2}$$

where

$$\begin{aligned} a_0 &= R_{rec} + R_{tot} \\ a_1 &= L_{tot} + 1/6 R_{tot}^2 C_{tot} + 1/2 R_{tot} C_{tot} R_{rec} \\ b_0 &= 1 \\ b_1 &= C_{tot} R_{rec} + 1/2 R_{tot} C_{tot} \\ b_2 &= 1/6 R_{tot} C_{tot}^2 R_{rec} + 1/24 R_{tot}^2 C_{tot}^2 + 1/2 L_{tot} C_{tot} \end{aligned} \tag{7.3}$$

where $R_{tot} = rh$, $L_{tot} = lh$, $C_{tot} = ch$ and $Z_L = R_{rec}$ which is the resistance of the current-mode receiver. The driving point impedance of a resistance-terminated Π-model shown in Fig. 7.1 can be derived as

$$Z_{in}^{\Pi} = \frac{n_0 + n_1 s + O(s^2)}{d_0 + d_1 s + d_2 s^2 + O(s^3)} \tag{7.4}$$

where

$$\begin{aligned} n_0 &= R_1 + R_2 + R_{rec} \\ n_1 &= R_1 C_2 (R_2 + R_{rec}) + L_1 \\ d_0 &= 1 \\ d_1 &= C_2 (R_2 + R_{rec}) + C_1 (R_2 + R_{rec}) + C_1 R_1 \\ d_2 &= C_1 R_1 C_2 (R_2 + R_{rec}) + C_1 L_1. \end{aligned} \tag{7.5}$$

In order to obtain the RC-model for the driving point impedance of a resistance-terminated RC transmission line, we set $Z_{in}^{tl} = Z_{in}^{\Pi}$ while setting inductive values to zero. The RC values are obtained as

$$\begin{aligned} C_1^{rc} &= \frac{1}{4} \frac{C_{tot}(4R_{rec} + R_{tot})}{\gamma} \\ C_2^{rc} &= \frac{3}{4} \frac{C_{tot}(8R_{rec}^2 + 5R_{rec}R_{tot} + R_{tot}^2)^2}{\gamma(24R_{rec}^3 + 21R_{rec}^2 R_{tot} + 6R_{rec}R_{tot}^2 + R_{tot}^3)} \\ R_1^{rc} &= \frac{2}{3} \frac{R_{tot}(9R_{rec}^2 + 6R_{rec}R_{tot} + R_{tot}^2)}{8R_{rec}^2 + 5R_{rec}R_{tot} + R_{tot}^2} \\ R_2^{rc} &= \frac{1}{3} \frac{R_{tot}(6R_{rec}^2 + 3R_{rec}R_{tot} + R_{tot}^2)}{8R_{rec}^2 + 5R_{rec}R_{tot} + R_{tot}^2} \end{aligned} \tag{7.6}$$

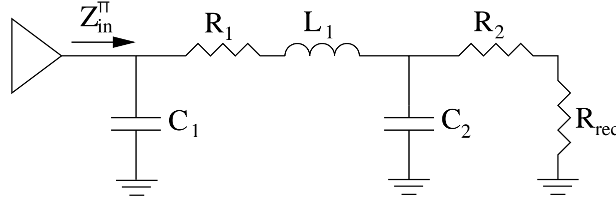

Figure 7.1: RLC Π model for current-mode driving point impedance. R_2 and R_{rec} are drawn separately for clarity.

where $\gamma = 3R_{rec} + R_{tot}$. In order to obtain an RLC-model, a fifth condition is needed to solve the inductance term L_1, while also obtaining realizable values. We set $C_1 + C_2 = C_{tot}$, which is desirable for energy calculations. Similarly, we already have $R_1 + R_2 = R_{tot}$ from (7.3) and (7.5). The values for the RLC model in Fig. 7.1 are obtained as

$$\begin{aligned}
C_1^{rlc} &= \frac{1}{4}\frac{C_{tot}(R_{tot}^2 C_{tot} + 4R_{tot}C_{tot}R_{rec} + 12L_{tot})}{3R_{tot}C_{tot}R_{rec} + 6L_{tot} + R_{tot}^2 C_{tot}} \\
C_2^{rlc} &= \frac{1}{4}\frac{C_{tot}(3R_{tot}^2 C_{tot} + 8R_{tot}C_{tot}R_{rec} + 12L_{tot})}{3R_{tot}C_{tot}R_{rec} + 6L_{tot} + R_{tot}^2 C_{tot}} \\
R_1^{rlc} &= \frac{2R_{tot}(R_{tot}^2 C_{tot} + 3R_{tot}C_{tot}R_{rec} + 6L_{tot})}{3R_{tot}^2 C_{tot} + 8R_{tot}C_{tot}R_{rec} + 12L_{tot}} \\
R_2^{rlc} &= \frac{R_{tot}^2(2R_{rec}C_{tot} + R_{tot}C_{tot})}{3R_{tot}^2 C_{tot} + 8R_{tot}C_{tot}R_{rec} + 12L_{tot}} \\
L_1^{rlc} &= \frac{\alpha R_{tot}C_{tot} + 36L_{tot}^2}{9R_{tot}^2 C_{tot} + 24R_{tot}C_{tot}R_{rec} + 36L_{tot}}
\end{aligned} \tag{7.7}$$

where $\alpha = R_{tot}^2 C_{tot}R_{rec} + 15R_{tot}L_{tot} + 24L_{tot}R_{rec}$. As can be seen, the RLC values are always positive. It can be noted that the value of L_1 and the inductance seen by the driver depend on the amount of resistive attenuation, or total resistance of the wire.

7.2 Modeling of Energy Dissipation

In order to be able to use both pre-characterized drivers and switch-resistor drivers, the input voltage to the wire in Fig. 7.2 is used as the input signal. The input V_{in} to the wire is modeled as an exponential voltage

$$V_{in}(t) = V_{max}[1 - e^{-t/t_r}] \tag{7.8}$$

where V_{max} is the characterized or calculated maximum voltage of the input signal to the wire. In current-mode signaling, the input signal to the wire does

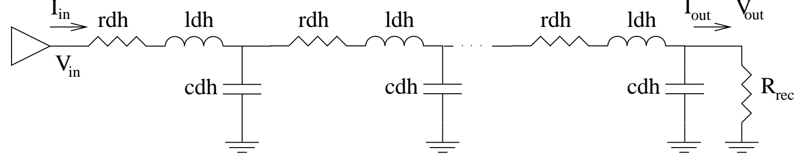

Figure 7.2: RLC transmission line model for current-mode signaling.

not have a full voltage swing. Instead, the swing depends on driver, wire and receiver properties. The exponential rise time t_r and gate delay were also used to characterize the driver with the Π model. In case of a driver represented as a switch-resistor with source resistance R_s along with a voltage source with finite rise time, $V_{max} = V_{dd}(R_{tot} + R_{rec})/(R_s + R_{tot} + R_{rec})$, and t_r is easily calculated from the presented Π-circuit. The input in s-domain is

$$V_{in}(s) = V_{max}\left[\frac{1}{s} - \frac{1}{s + 1/t_r}\right]. \tag{7.9}$$

The total energy E_{tot} dissipated by the transmission line in Fig. 7.2 during one clock cycle including the driver, wire and receiver termination is obtained from

$$E_{tot} = V_{dd}\int_0^{t_c} I_{in}(t)dt \tag{7.10}$$

where t_c is the clock cycle time. The input current can be obtained from $I_{in} = V_{in}/Z_{in}^{\Pi}$. For energy calculations a 1-pole form of the input current is used in order to obtain compact and computationally effective models while maintaining accuracy. The input current is

$$I_{in}(t) = \frac{V_{max}}{n_0} + \left(\frac{V_{max}t_r^{-1}d_1}{t_r^{-1}n_1 + n_0} - \frac{V_{max}}{n_0}\right)e^{-pt} \tag{7.11}$$

where

$$p = \frac{n_0 t_r^{-1}}{n_1 t_r^{-1} + n_0}. \tag{7.12}$$

The total energy dissipation is obtained using (7.10) and (7.11) as

$$\begin{aligned} E_{tot} &= V_{dd}\left[\frac{V_{max}t_c}{n_0} + \left(\frac{V_{max}d_1}{n_0}\right.\right. \\ &- \left.\left.\frac{V_{max}(t_r^{-1}n_1 + n_0)}{t_r^{-1}n_0^2}\right)(1 - e^{-pt_c})\right]. \end{aligned} \tag{7.13}$$

The output current I_{out} of the transmission line in Fig. 7.2 can be calculated by substituting (7.9) into

$$I_{out} = \frac{V_{in}}{a_{11}R_{rec} + a_{12} + a_{22}R_{rec}}. \tag{7.14}$$

By applying partial fraction expansion and taking an inverse Laplace transform the output current becomes

$$I_{out}(t) = A_0 + \sum_{i=1}^{m} A_i e^{s_i t}. \tag{7.15}$$

A four pole form of (7.15) is the longest that can be obtained analytically. This form is applied to capture the complex waveform of the output current in delay calculations while for energy calculation the 1-pole form is used again as

$$I_{out}(t) = \frac{V_{max}}{R_{tot} + R_{rec}} - \frac{V_{max}}{R_{tot} + R_{rec}} e^{-\frac{t_r^{-1} a_0 t}{t_r^{-1} a_1 + a_0}}. \tag{7.16}$$

The energy E_{rec} dissipated by the receiver is

$$E_{rec} = \int_0^{t_c} V_{out}(t) I_{out}(t) dt \tag{7.17}$$

where $V_{out} = I_{out} R_{rec}$. The receiver termination energy dissipation is then obtained using (7.16) and (7.17) as

$$E_{rec} = \frac{V_{max}^2 R_{rec}}{2q(R_{tot} + R_{rec})^2} [2qt_c + 4e^{-qt_c} - e^{-2qt_c} - 3] \tag{7.18}$$

where

$$q = \frac{t_r^{-1} a_0}{t_r^{-1} a_1 + a_0}. \tag{7.19}$$

The energy E_{wire} dissipated in the wire can be obtained from

$$E_{wire} = \int_0^{t_c} V_{in}(t) I_{in}(t) dt - E_{rec} \tag{7.20}$$

where the integral term is the energy dissipated by the wire and the receiver together. The wire energy is

$$\begin{aligned} E_{wire} &= \frac{V_{max}^2}{n_0} \left(t_c + t_r e^{-t_c/t_r} - t_r \right) \\ &- \left(\frac{V_{max}^2 t_r^{-1} d_1}{t_r^{-1} n_1 + n_0} - \frac{V_{max}^2}{n_0} \right) \left(\frac{1}{p} (e^{-t_c p} - 1) \right. \\ &- \left. \frac{1}{p + t_r^{-1}} \left(e^{-t_c (p + t_r^{-1})} - 1 \right) \right) - E_{rec}. \end{aligned} \tag{7.21}$$

The energy E_{dr} dissipated in the driver is then obtained as

Table 7.1: Wire properties and RLC parameters used in simulations

	Wire width (μm)	R (Ω/mm)	L (nH/mm)	C (fF/mm)
1 mm wire	0.5	161	1.31	164
3 mm wire	1.0	80.6	1.22	243
5 mm wire	1.5	53.8	1.16	322

$$E_{dr} = \int_0^{t_c} [V_{dd} - V_{in}(t)]\, I_{in}(t) dt = E_{tot} - E_{rec} - E_{wire}. \tag{7.22}$$

The previous analysis has been for a rising transition. In case of a falling transition, the wire capacitances are discharged through the receiver and driver. The input to the wire is then

$$V_{in}(t) = V_{max} e^{-t/t_f}. \tag{7.23}$$

where t_f is the fall time of the input signal. Assuming that the system has reached steady state between signals, the steady state current and voltage values used in the analysis as the starting points of the falling transition are

$$I_{in}^{ss} = I_{out}^{ss} = \frac{V_{max}}{R_{tot} + R_{rec}} \tag{7.24}$$

and

$$V_{out}^{ss} = \frac{V_{max} R_{rec}}{R_{tot} + R_{rec}}. \tag{7.25}$$

For multiple coupled wires as in a bus, in the characterization of the driving-point impedance and the calculation of energy, the coupling capacitance in C_{tot} was taken into account by multiplying it with the appropriate switching factor depending on the transition activity of neighboring wires. (2.10) and (2.20) where then used to calculate the response of the current-mode system.

7.3 Verification

7.3.1 Single-Ended Current-Mode Signaling

In Fig. 7.3 is shown a comparison between the driving point voltages of the RLC Π-model and a transmission line. The driver was a 50x inverter and the transmission line consisted of 40 RLC segments and was terminated with a 150Ω resistor. The comparison was done using HSPICE in 65 nm technology. Three different wire types, whose RLC parameters were extracted using field solvers [90, 89], were used. The wire parameters are shown in Table 7.1. Wire thickness was 319 nm for all cases. As can be seen from Fig. 7.3, the Π driving point model followed the transmission line well, although as expected the accuracy was slightly reduced as the wire length increased.

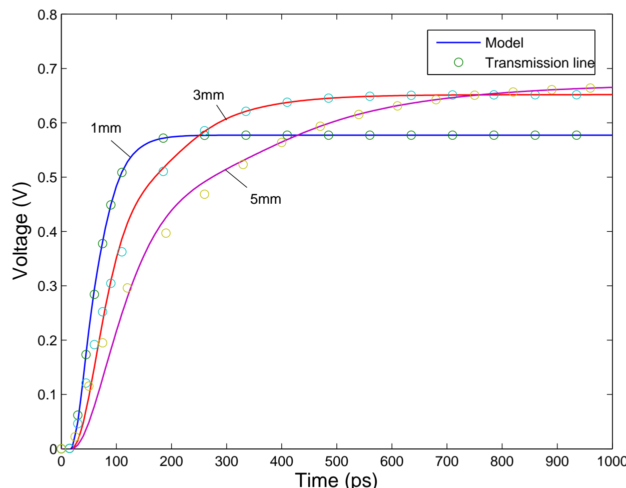

Figure 7.3: Driving point voltages of the presented RLC Π-model and a transmission line. Three different wires were used.

In Fig. 7.4 is shown a comparison between the model and HSPICE for the power dissipation of a 50x inverter with a rising output driving a 3 mm long wire with a termination resistance of 150Ω. The results are plotted separately for the driver, wire, receiver and total power. The power components were calculated as a product of voltage and current as in (7.10), (7.17), (7.20) and (7.22). As can be seen, the model and HSPICE are in good agreement. It should be noted that none of the power dissipation curves falls to zero, since in current-mode signaling there is a resistive path from V_{dd} to ground, which causes a steady state current for rising signals. The brief short-circuit power in the driver during transitions is not included, but it can be estimated as approximately 10% of dynamic power [150].

In Tables 7.2 and 7.3 is shown a comparison between the model and HSPICE for energy and propagation delay. The values were calculated using the wire properties in Table 7.1. The driver and receiver were varied as shown. The total energy dissipation was calculated for two different cycle times, i.e. 0.5 ns and 1 ns. The threshold used in delay calculation was 0.4 mA. The delay was calculated using two different forms of (7.15), i.e. 1 pole and 4 poles. The energy dissipation was calculated using (7.13). As can be seen, the 4 pole approximation of the delay was in good agreement with the HSPICE results with an average error of 1.9 %, while the shorter 1 pole approximation had an average error of 13.3 %. The energy dissipation had an average error of 1.9%.

Verification results using a switch-resistor driver are shown in Fig. 7.5. A histogram with 1500 random samples was generated by comparing the model

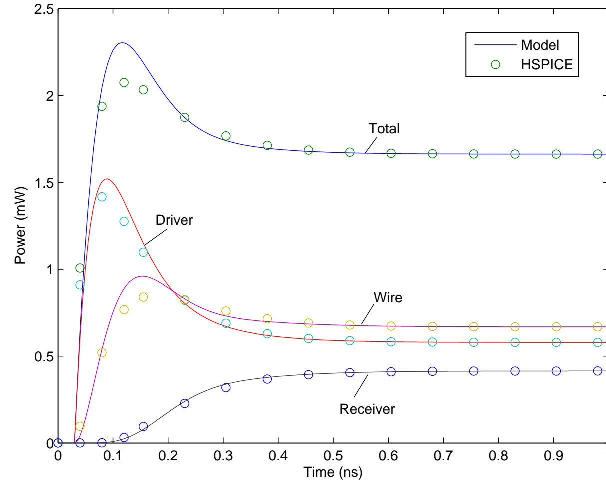

Figure 7.4: Comparison between the model and HSPICE for the power dissipation of a 50x inverter driving a 3 mm wire with a termination resistance of 150Ω.

Table 7.2: Verification results for total energy dissipation using different wire, driver and receiver sizes

Driver (size)	Receiver (Ω)	Wire len. (mm)	E_{tot}^{model} (pJ)		E_{tot}^{spice} (pJ)	
			$t_c = 0.5ns$	$t_c = 1ns$	$t_c = 0.5ns$	$t_c = 1ns$
10x	500	1	0.224	0.466	0.225	0.467
25x	1000	3	0.490	0.860	0.491	0.873
50x	2000	5	0.866	1.375	0.900	1.460
25x	500	1	0.436	0.891	0.437	0.889
50x	2000	3	0.649	0.931	0.682	0.941
10x	1000	5	0.250	0.498	0.242	0.495

Table 7.3: Verification results for propagation delay using different wire, driver and receiver sizes

Driver (size)	Receiver (Ω)	Wire len. (mm)	t_{delay}^{model} (ps)		t_{delay}^{spice} (ps)
			1 pole	4 poles	
10x	500	1	210	199	200
25x	1000	3	414	414	430
50x	2000	5	1998	1523	1549
25x	500	1	81	86	88
50x	2000	3	843	666	665
10x	1000	5	4766	4301	4439

results to HSPICE over a wide range of parameters. In the figure is demonstrated the error distribution for E_{tot} and as a comparison also for the model in [145]. The parameters used were: voltage source risetime 1–500ps, h 0.5–8mm, c 20–500fF/mm, r 10–500Ω/mm, l 0.01–5nH/mm, R_s 10–1000Ω, R_{rec} 10–4000Ω, and t_c 150–6300ps or at least 75% of output signal risetime. The mean and standard deviation are also shown in the figure for total, driver, wire and receiver energy components calculated with the presented model. The results were calculated using equations (7.13), (7.18), (7.21) and (7.22).

7.3.2 Differential Current-Mode Signaling

The model was applied to the analysis of differential current-mode signaling. The implementation of the differential signaling is shown in Fig. 7.6. The driver was implemented as two 50x inverters while the receiver was a modified clamped bit-line sense amplifier [151]. The 200 Ω termination resistances in the lower-right corner were implemented as in [152]. The termination transistor lengths were 65 nm and their widths were 3.2 μm. The wires were 3 mm long and the separation distance was 0.25μm. The coupling capacitance was 41 fF/mm and mutual inductance 0.94 nH/mm. The output and input currents of the wires are shown in Fig. 7.7. As can be seen, the model results and HSPICE were close to each other. A comparison between the model and HSPICE for the rising input energy dissipation of the differential system is shown in Fig. 7.8. As can be seen, the results were again in good agreement.

7.4 Case Study

In Fig. 7.9 is shown the energy dissipation of a 3 mm wire with a 50x inverter as a driver and a 200 Ω termination. The energy dissipation was calculated with the model as a function of t_c and wire widths ranging from 0.25 μm to 1.5 μm at 0.25 μm intervals. The RLC parameters were extracted with field solvers for each case. In voltage-mode signaling, the energy dissipation of an interconnect depends linearly on capacitance, as seen from the CV^2 model. In

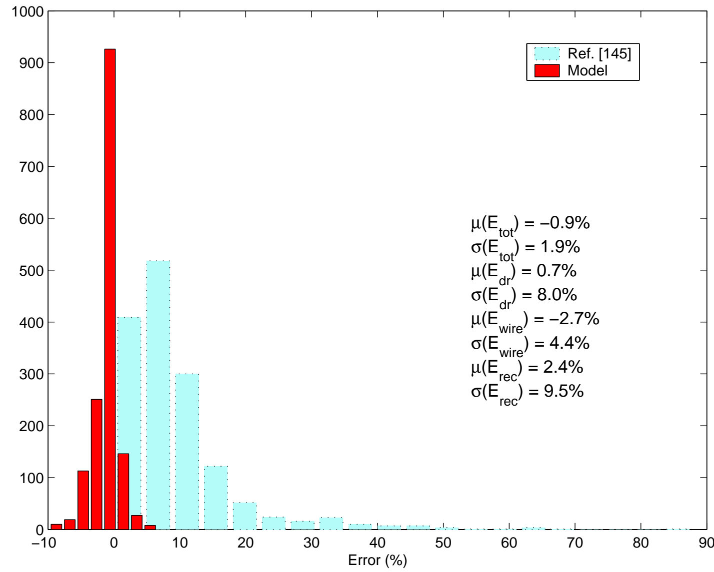

Figure 7.5: Error comparison for E_{tot} using the model and [145]. The mean μ, and standard deviation σ are shown for all model energy components.

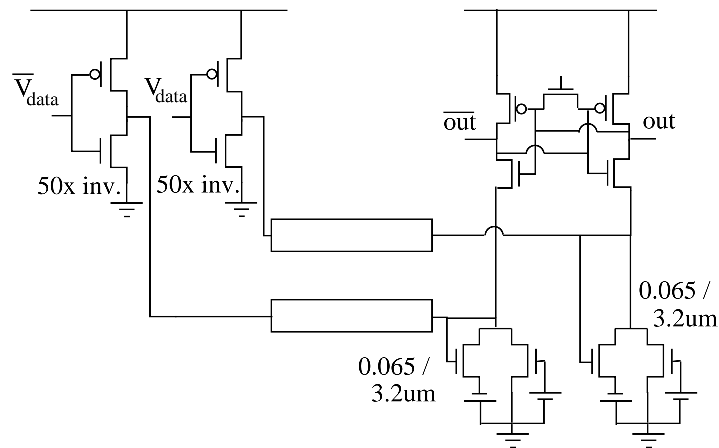

Figure 7.6: Implementation of differential current-mode signaling.

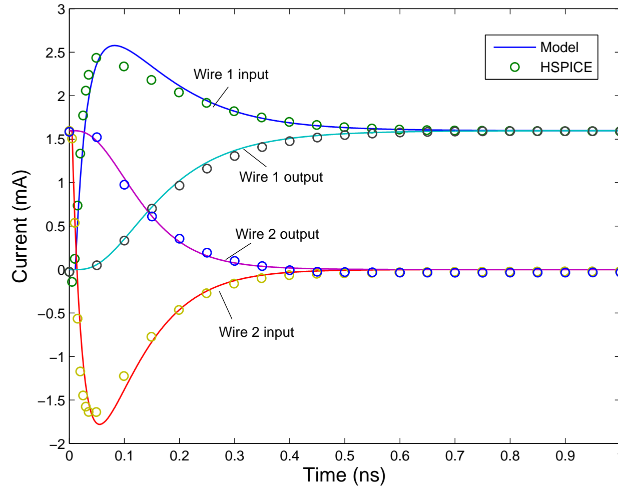

Figure 7.7: Comparison between the model and HSPICE for the input and output currents of the 3 mm wires using differential current-mode signaling.

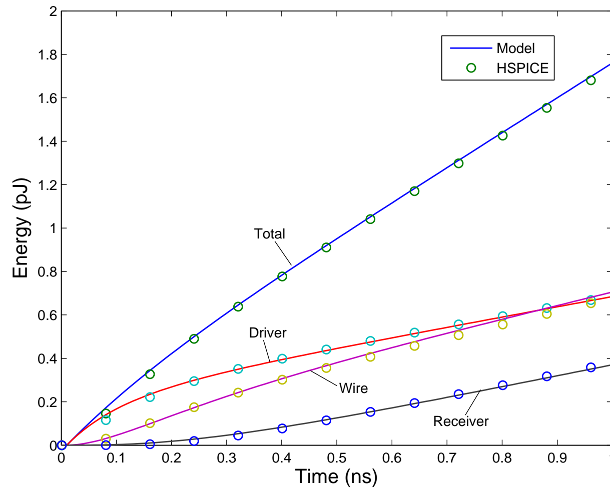

Figure 7.8: Comparison between the model and HSPICE for rising wire energy dissipation using differential current-mode signaling.

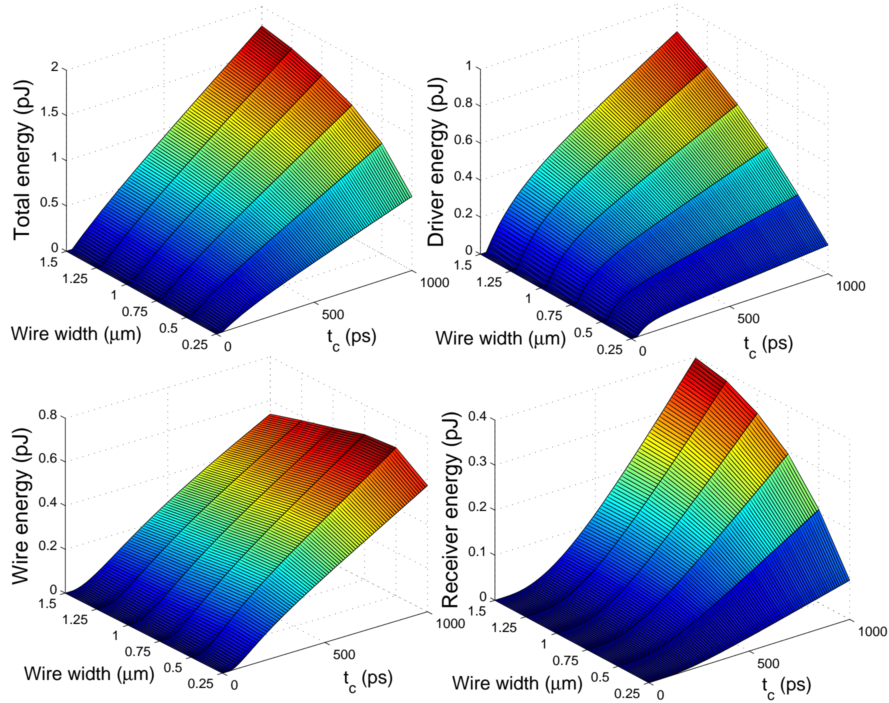

Figure 7.9: Energy as a function of wire width and clock cycle time t_c for a 3 mm wire with width ranging from 0.25 μm to 1.5 μm using a 50x inverter as a driver and a 200Ω termination.

current-mode signaling, the amount of energy and where the energy is dissipated varies depending on the wire width as seen in Fig. 7.9. For example, the energy dissipated at the receiver grew when the wire width was increased. This was caused by the reduced wire resistance that increased the output voltage swing. The overall reduced resistance also resulted in an increase in the total energy and driver energy dissipation. The energy dissipation in the wire varied with wire width based on the static power dissipation and the voltage swing that influences the capacitive energy dissipation. The voltage swing varies depending on the driver, wire and receiver properties. The significant effect of the clock cycle time on all energy components is also seen in the figure.

7.5 Chapter Summary

In this chapter, an analytical model for the energy dissipation of RLC transmission lines in current-mode signaling was proposed. The energy was derived separately for the driver, wire and receiver termination. The model included the effects of different clock cycles, rise times, transient resistive power and inductance. In addition, a realizable Π-model for the driving point impedance of a current-mode RLC transmission line was derived. The output current at the end of an RLC current-mode line was also derived. The models were developed for both switch-resistor and pre-characterized drivers. The energy, driving-point and output current models were verified by comparison to HSPICE in 65 nm technology. The average error was 1.9% for delay using 4-pole output current and -0.9% for total energy with a standard deviation of 1.9% using 1-pole form. The model was extended to multiple interconnects with capacitive and inductive coupling and applied to model differential current-mode signaling. The component where energy is dissipated in current-mode signaling was shown to depend on wire width.

Chapter 8

Conclusions

This thesis considered modeling and analysis of noise and interconnects in on-chip communication links. These long links are used to connect IP blocks together and they are often a bottleneck in modern integrated circuits. Analysis and optimization of the links requires accurate and computationally effective interconnect models that can be used in the iterative refinement loops of the early stages of a design flow. For this purpose, several models were proposed in this thesis. Specifically, the models were developed for multiple parallel interconnects that commonly form a bus segment or a link in a NoC. Because of significant electromagnetic coupling in such links, the interconnects were modeled as an interacting group instead of as isolated signal paths. The developed analytical models addressed issues such as signal integrity, energy dissipation, and alternative signaling techniques. Furthermore, the models were also applied to optimize signal integrity problems.

A major source of noise that affects interconnects running close to each other is crosstalk. Another interconnect noise source is intersymbol interference that influences successive signals. An analytical model was proposed in the thesis to evaluate both crosstalk and intersymbol interference. The model includes multiple aspects that affect these noise sources such as both inductive and capacitive coupling, phases and different bit sequences. The model was then applied in case studies to show that intersymbol interference affects crosstalk voltage and propagation delay depending on bus throughput and the amount of inductance.

On-chip communication consumes a significant portion of total power and therefore places a burden on the power supply network. In order to determine the induced power supply noise, it is necessary to know the load on a power supply network. A model for the switching current of a bus was therefore developed in the thesis. The switching current was shown to depend on the interconnect coupling and switching patterns. The model was then combined with an existing power supply network model and applied to demonstrate the reduction of power supply noise with bus input skewing.

This intentional skewing was then applied to reduce both functional crosstalk and power supply noise. Unlike in previous methods, this was achieved as a

trade-off with time or timing slack and without encoding or additional wires which makes the method well suited for area limited cases. Models proposed in the previous chapters were used to calculate crosstalk and power supply noise as a function of skewing. The skewing method was shown to be effective in reducing long-range inductive crosstalk. The method was implemented and compared to other crosstalk and power supply reduction methods. The impact of the implementation on energy dissipation was less than 1.2% in simulations. Skewing was also demonstrated to be usable alone or together with other noise reduction methods.

In long buses, encoding is a promising method to avoid problematic switching patterns. This is however achieved with additional logic circuitry that is susceptible to process variation together with the wires. A model was thus proposed for analyzing the effects of process variation on encoded buses. The model includes variation in both the signaling circuitry and in the wires to calculate the delay variation of the encoded bus. The model was applied to level-encoded dual-rail and 1-of-4 signaling using Monte Carlo analysis to evaluate the statistical influence of wire width variation.

Another promising signaling method for long interconnects is current-mode signaling that employs current sensing together with a resistive termination. An analytical model for energy dissipation in RLC current-mode signaling was proposed in the thesis. The energy was derived separately for the driver, wire and receiver termination. The model was developed for both switch-resistor and pre-characterized drivers and it included the effects of different clock cycles, rise times, transient resistive power and inductance. A realizable driving-point impedance for an RLC current-mode line was also derived. The energy model was applied to differential signaling and to analyze the changes in energy dissipation as a function of wire width. The location where energy is dissipated in current-mode signaling was shown to depend on wire width.

To conclude, a set of analytical models was proposed for the analysis and optimization of on-chip communication links. The proposed models were also applied in noise reduction. All models proposed in the thesis included the effects of inductance and they were verified by a comparison to HSPICE using RLC parameters extracted with field solvers. A significant speedup over HSPICE was also demonstrated. In addition to the wires themselves, also signaling circuitry was considered in the modeling. While the focus of the thesis was in the analysis and modeling of on-chip communication links, possible future research directions can be outlined. One future possibility could be to integrate the developed models into a simulation tool, e.g. for design space exploration or communication optimization purposes. Besides simulation tool integration, another possible future direction could be to adjust or expand the developed models for emerging on-chip interconnects such as through-silicon via bundles [153, 154] in 3-D integrated circuits, or even carbon nanotubes whose interconnect behavior has been shown to be analyzable with RLC transmission line circuits [155, 156].

Bibliography

[1] N. A. Kurd, S. Bhamidipati, C. Mozak, J. L. Miller, T. M. Wilson, M. Nemani, and M. Chowdhury. Westmere: A family of 32nm IA processors. In *Digest of IEEE Int. Solid-State Circuits Conference*, pages 96–97, 2010.

[2] S. Natarajan et al. A 32nm logic technology featuring 2nd-generation high-k + metal-gate transistors, enhanced channel strain and $0.171\mu m^2$ SRAM cell size in a 291Mb array. In *Proc. IEEE Int. Electron Devices Meeting*, pages 1–3, 2008.

[3] International Technology Roadmap for Semiconductors. Interconnect, 2005, 2007 and 2009 editions. Online, http://www.itrs.net.

[4] N. Magen, A. Kolodny, U. Weiser, and N. Shamir. Interconnect-power dissipation in a microprocessor. In *Proc. Int. Workshop on System-Level Interconnect Prediction*, pages 7–13, 2004.

[5] R. Ho, K. W. Mai, and M. A. Horowitz. The future of wires. *Proceedings of the IEEE*, 89(4):490–504, Apr. 2001.

[6] S. Kumar, A. Jantsch, J.-P. Soininen, M. Forsell, M. Millberg, J. Öberg, K. Tiensyrjä, and A. Hemani. A network on chip architecture and design methodology. In *Proc. IEEE Computer Society Annual Symp. on VLSI*, pages 105–112, 2002.

[7] T. Bjerregaard and S. Mahadevan. A survey of research and practices of network-on-chip. *ACM Computing Surveys*, 38(1):1–51, Mar. 2006.

[8] S. Vangal et al. An 80-tile 1.28TFLOPS network-on-chip in 65nm CMOS. In *Digest of IEEE Int. Solid-State Circuits Conf.*, pages 98–99, 2007.

[9] C.-T. Hsieh and M. Pedram. Architectural energy optimization by bus splitting. *IEEE Transactions on Computer-Aided Design of Integrated Circuits and Systems*, 21(4):408–414, Apr. 2002.

[10] A. Narasimhan and R. Sridhar. Variability aware low-power delay optimal buffer insertion for global interconnects. *IEEE Transactions on Circuits and Systems I*, 57(12):3055–3063, Dec. 2010.

[11] W. J. Dally and J. W. Poulton. *Digital Systems Engineering*. Cambridge, UK: Cambridge University Press, 1998.

[12] A. Katoch, E. Seevinck, and H. Veendrick. Fast signal propagation for point to point on-chip long interconnects using current sensing. In *Proc. 28th European Solid-State Circuits Conference*, pages 195–198, Sept. 2002.

[13] K. Banerjee, H. Li, and N. Srivastava. Current status and future perspectives of carbon nanotube interconnects. In *Proc. IEEE Conf. on Nanotechnology*, pages 432–436, 2008.

[14] S. Pasricha, F. J. Kurdahi, and N. Dutt. Evaluating carbon nanotube global interconnects for chip multiprocessor applications. *IEEE Transactions on Very Large Scale Integration (VLSI) Systems*, 18(9):1376–1380, Sept. 2010.

[15] M. Haurylau, G. Chen, H. Chen, J. Zhang, N. A. Nelson, D. H. Albonesi, E. G. Friedman, and P. M. Fauchet. On-chip optical interconnect roadmap: Challenges and critical directions. *IEEE Journal of Selected Topics in Quantum Electronics*, 12(6):1699–1705, Nov./Dec. 2006.

[16] M. F. Chang, J. Cong, A. Kaplan, M. Naik, G. Reinman, E. Socher, and S.-W. Tam. CMP network-on-chip overlaid with multi-band RF-interconnect. In *Proc. IEEE Int. Symp. on High Performance Computer Architecture*, pages 191–202, 2008.

[17] A. Agarwal, D. Blaauw, and V. Zolotov. Statistical timing analysis for intra-die process variations with spatial correlations. In *Proc. Int. Conf. on Computer Aided Design*, pages 900–907, 2003.

[18] R. Gandikota, D. Blaauw, and D. Sylvester. Modeling crosstalk in statistical static timing analysis. In *Proc. 45th Design Automation Conference*, pages 974–979, 2008.

[19] E. Humenay, D. Tarjan, and K. Skadron. Impact of process variations on multicore performance symmetry. In *Proc. Design, Automation and Test in Europe*, pages 1–6, 2007.

[20] W. Zhao and Y. Cao. New generation of predictive technology model for sub-45nm early design exploration. *IEEE Transactions on Electron Devices*, 53(11):2816–2823, Nov. 2006.

[21] A. Agarwal, D. Blaauw, V. Zolotov, and S. Vrudhula. Computation and refinement of statistical bounds on circuit delay. In *Proc. 40th Design Automation Conference*, pages 348–353, 2003.

[22] L. T. Pillage and R. A. Rohrer. Asymptotic waveform evaluation for timing analysis. *IEEE Transactions on Computer-Aided Design of Integrated Circuits and Systems*, 9(4):352–366, Apr. 1990.

[23] A. Odabasioglu, M. Celik, and L. T. Pileggi. PRIMA: Passive reduced-order interconnect macromodeling algorithm. *IEEE Transactions on Computer-Aided Design of Integrated Circuits and Systems*, 17(8):645–654, Aug. 1998.

[24] L. Ding, D. Blaauw, and P. Mazumder. Accurate crosstalk noise modeling for early signal integrity analysis. *IEEE Transactions on Computer-Aided Design of Integrated Circuits and Systems*, 22(5):627–634, May 2003.

[25] Y. I. Ismail, E. G. Friedman, and José L. Neves. Figures of merit to characterize the importance of on-chip inductance. *IEEE Transactions on Very Large Scale Integration (VLSI) Systems*, 7(4):442–449, Dec. 1999.

[26] C. R. Paul. Decoupling the multiconductor transmission line equations. *IEEE Transactions on Microwave Theory and Techniques*, 44(8):1429–1440, Aug. 1996.

[27] J. W. Johnson and M. Graham. *High-Speed Signal Propagation: Advanced Black Magic.* Upper Saddle River, NJ: Prentice Hall, 2003.

[28] C. R. Paul. *Analysis of Multiconductor Transmission Lines.* New York, NY: John Wiley & Sons, 1994.

[29] F. J. German and R. W. Johnson. Full wave three-dimensional simulation of Maxwell's equations for the electrical characterization of high-speed interconnects. *IEEE Transactions on Components, Hybrids, and Manufacturing Technology*, 13(2):341–346, June 1990.

[30] J. Cong, T. Kong, and D. Z. Pan. Buffer block planning for interconnect-driven floorplanning. In *Proc. Int. Conf. on Computer-Aided Design*, pages 358–363, 1999.

[31] Y.-H. Cheng and Y.-W. Chang. Integrating buffer planning with floorplanning for simultaneous multi-objective optimization. In *Proc. Asia and South Pacific Design Automation Conference*, pages 624–627, 2004.

[32] W.-L. Hung, G. M. Link, Y. Xie, N. Vijaykrishnan, and M. J. Irwin. Interconnect and thermal-aware floorplanning for 3D microprocessors. In *Proc. 7th Int. Symp. on Quality Electronic Design*, pages 104–109, 2006.

[33] T. Zhang and S. S. Sapatnekar. Simultaneous shield and buffer insertion for crosstalk noise reduction in global routing. *IEEE Transactions on Very Large Scale Integration (VLSI) Systems*, 15(6):624–636, Jun. 2007.

[34] M. Cho, D. Z. Pan, H. Xiang, and R. Puri. Wire density driven global routing for CMP variation and timing. In *Proc. Int. Conf. on Computer-Aided Design*, pages 487–492, 2006.

[35] M. R. Becer, D. Blaauw, I. Algor, R. Panda, C. Oh, V. Zolotov, and I. N. Hajj. Postroute gate sizing for crosstalk noise reduction. *IEEE Transactions on Computer-Aided Design of Integrated Circuits and Systems*, 23(12):1670–1677, Dec. 2004.

[36] N. Hanchate and N. Ranganathan. Post-layout gate sizing for interconnect delay and crosstalk noise optimization. In *Proc. 7th Int. Symp. on Quality Electronic Design*, pages 97–102, 2006.

[37] K. Moiseev, A. Kolodny, and S. Wimer. Power-delay optimiztion in VLSI microprocessors by wire spacing. *ACM Transactions on Design Automation of Electronic Systems*, 14(4):55:1–55:28, Aug. 2009.

[38] A. Vittal and M. Marek-Sadowska. Crosstalk reduction for VLSI. *IEEE Transactions on Very Large Scale Integration (VLSI) Systems*, 16(3):290–298, Mar. 1997.

[39] K. Agarwal, D. Sylvester, and D. Blaauw. Modeling and analysis of crosstalk noise in coupled RLC interconnects. *IEEE Transactions on Computer-Aided Design of Integrated Circuits and Systems*, 25(5):892–901, May 2006.

[40] C.-W. Ho, A. Ruehli, and P. Brennan. The modified nodal approach to network analysis. *IEEE Transactions on Circuits and Systems*, 22(6):504–509, June 1975.

[41] M. Celik, L. Pileggi, and A. Odabasioglu. *IC Interconnect Analysis*. Norwell, MA: Kluwer Academic Publishers, 2002.

[42] E. Chiprout and M. S. Nakhla. Analysis of interconnect networks using complex frequency hopping (CFH). *IEEE Transactions on Computer-Aided Design of Integrated Circuits and Systems*, 14(2):186–200, Feb. 1995.

[43] P. Feldmann and R. W. Freund. Efficient linear circuit analysis by Padé approximation via the Lanczos process. *IEEE Transactions on Computer-Aided Design of Integrated Circuits and Systems*, 14(5):639–649, May 1995.

[44] J. R. Phillips and L. M. Silveira. Poor man's TBR: A simple model reduction scheme. *IEEE Transactions on Computer-Aided Design of Integrated Circuits and Systems*, 24(1):43–55, Jan. 2005.

[45] K. C. Sou, A. Megretski, and L. Daniel. A quasi-convex optimization approach to parameterized model order reduction. *IEEE Transactions on Computer-Aided Design of Integrated Circuits and Systems*, 27(3):456–469, Mar. 2008.

[46] H. Yu, Y. Shi, and L. He. Fast analysis of structured power grid by triangularization based structure preserving model order reduction. In *Proc. 43rd Design Automation Conference*, pages 205–210, 2006.

[47] Y. Shin and T. Sakurai. Power distribution analysis of VLSI interconnects using model order reduction. *IEEE Transactions on Computer-Aided Design of Integrated Circuits and Systems*, 21(6):739–745, Jun. 2002.

[48] B. Franzini, C. Forzan, D. Pandini, P. Scandolara, and A. Dal Fabbro. Crosstalk aware static timing analysis: a two step approach. In *Proc. IEEE Int. Symp. on Quality Electronic Design*, pages 499–503, 2000.

[49] P. Feldmann. Model order reduction techniques for linear systems with large numbers of terminals. In *Proc. Design, Automation and Test in Europe*, pages 944–947, 2004.

[50] P. Liu, S. X.-D. Tan, B. McGaughy, L. Wu, and L. He. Termmerg: An efficient terminal-reduction method for interconnect circuits. *IEEE Transactions on Computer-Aided Design of Integrated Circuits and Systems*, 26(8):1382–1392, Aug. 2007.

[51] P. Feldmann and F. Liu. Sparse and efficient reduced order modeling of linear subcircuits with large number of terminals. In *Proc. IEEE/ACM Int. Conf. on Computer-Aided Design*, pages 88–92, 2004.

[52] S. Aaltonen. *Order Reduction of Interconnect Circuits*. Licentiate thesis, Helsinki University of Technology, 2003.

[53] S. Yu, D. M. Petranovic, S. Krishnan, K. Lee, and C. Y. Yang. Loop-based inductance extraction and modeling for multiconductor on-chip interconnects. *IEEE Transactions on Electron Devices*, 53(1):135–145, Jan. 2006.

[54] G.-T. Lei, G.-W. Pan, and B. K. Gilbert. Examination, clarification, and simplification of modal decoupling method for multiconductor transmission lines. *IEEE Transactions on Microwave Theory and Techniques*, 43(9):2090–2100, Sept. 1995.

[55] F. Szidarovszky and O. A. Palusinski. Clarification of a decoupling method for multiconductor transmission lines. *IEEE Transactions on Microwave Theory and Techniques*, 47(5):648–649, May 1999.

[56] R. J. Lopez. *Advanced Engineering Mathematics.* Boston, MA: Addison-Wesley, 2001.

[57] C. R. Paul. *Introduction to Electromagnetic Compatibility.* Hoboken, NJ: John Wiley & Sons, 2006.

[58] J. Chen and L. He. A decoupling method for analysis of coupled RLC interconnects. In *Proc. IEEE/ACM Int. Great Lakes Symposium on VLSI*, pages 41–46, 2002.

[59] G. Chen and E. G. Friedman. An RLC interconnect model based on Fourier analysis. *IEEE Transactions on Computer-Aided Design of Integrated Circuits and Systems*, 24(2):170–183, Feb. 2005.

[60] S. Subash, M. S. Rahaman, and M. H. Chowdhury. Compact model for carbon nanotubes interconnects using Fourier series analysis. In *Proc. IEEE Int. Midwest Symp. on Circuits and Systems*, pages 1175–1178, 2009.

[61] Y. Eo, S. Shin, W. R. Eisenstadt, and J. Shim. Generalized traveling-wave-based waveform approximation technique for the efficient signal integrity verification of multicoupled transmission line system. *IEEE Transactions on Computer-Aided Design of Integrated Circuits and Systems*, 21(12):1489–1497, Dec. 2002.

[62] J. Cong, L. He, K.-Y. Khoo, C.-K. Koh, and Z. Pan. Interconnect design for deep submicron ICs. In *Proc. IEEE/ACM Int. Conf. on Computer-Aided Design*, pages 478–485, 1997.

[63] J. Qian, S. Pullela, and L. Pillage. Modeling the 'effective capacitance' for the RC interconnect of CMOS gates. *IEEE Transactions on Computer-Aided Design of Integrated Circuits and Systems*, 13(12):1526–1535, Dec. 1994.

[64] K. Agarwal, D. Sylvester, and D. Blaauw. An effective capacitance based driver output model for on-chip RLC interconnects. In *Proc. 40th Design Automation Conference*, pages 376–381, 2003.

[65] S. Abbaspour and M. Pedram. Calculating the effective capacitance for the RC interconnect in VDSM technologies. In *Proc. Asia and South Pacific Design Automation Conference*, pages 43–48, 2003.

[66] A. Goel and S. Vrudhula. Current source based standard cell model for accurate signal integrity and timing analysis. In *Proc. Design, Automation and Test in Europe*, pages 574–579, 2008.

[67] N. Menezes, C. Kashyap, and C. Amin. A 'true' electrical cell model for timing, noise, and power grid verification. In *Proc. 45th Design Automation Conference*, pages 462–467, 2008.

[68] J. F. Croix and D. F. Wong. Blade and Razor: Cell and interconnect delay analysis using current-based models. In *Proc. 40th Design Automation Conference*, pages 386–389, 2003.

[69] I. Keller, K. H. Tam, and V. Kariat. Challenges in gate level modeling for delay and SI at 65nm and below. In *Proc. 45th Design Automation Conference*, pages 468–473, 2008.

[70] S. Nazarian, H. Fatemi, and M. Pedram. Accurate timing and noise analysis of combinational and sequential logic cells using current source modeling. *IEEE Transactions on Very Large Scale Integration (VLSI) Systems*, 19(1):92–103, Jan. 2011.

[71] P. Liljeberg, J. Tuominen, S. Tuuna, J. Plosila, and J. Isoaho. Self-timed approach for noise reduction in NOC. In J. Nurmi, H. Tenhunen, J. Isoaho, and A. Jantsch, editors, *Interconnect-Centric Design for Advanced SOC and NOC*, pages 285–313. Kluwer, Dordrecht, The Netherlands, 2004.

[72] T. Sato, Y. Cao, K. Agarwal, D. Sylvester, and C. Hu. Bidirectional closed-form transformation between on-chip coupling noise waveforms and interconnect delay-change curves. *IEEE Transactions on Computer-Aided Design of Integrated Circuits and Systems*, 22(5):560–572, May 2003.

[73] M. Becer and I. N. Hajj. An analytical model for delay and crosstalk estimation in interconnects under general switching conditions. In *Proc. IEEE Int. Conf. Electronics, Circuits and Systems*, pages 831–834, 2000.

[74] G. Servel and D. Deschacht. On-chip crosstalk evaluation between adjacent interconnections. In *Proc. IEEE Int. Conf. Electronics, Circuits and Systems*, pages 827–834, 2000.

[75] A. B. Kahng, S. Muddu, N. Pol, and D. Vidhani. Noise model for multiple segmented coupled RC interconnects. In *Proc. Int. Symp. Quality Electronic Design*, pages 145–150, 2001.

[76] J. Cong, D. Zhigang Pan, and P. V. Srinivas. Improved crosstalk modeling for noise constrained interconnect optimization. In *Proc. Asia South Pacific Design Automation Conf.*, pages 373–378, 2001.

[77] H. Kawaguchi and T. Sakurai. Delay and noise formulas for capacitively coupled distributed RC lines. In *Proc. Asia and South Pacific Design Automation Conf.*, pages 35–43, 1998.

[78] D. Pamunuwa, L.-R. Zheng, and H. Tenhunen. Maximizing throughput over parallel wire structures in the deep submicrometer regime. *IEEE Transactions on Very Large Scale Integration (VLSI) Systems*, 11(2):224–243, Apr. 2003.

[79] I. B. Dhaou, K. Parhi., and H. Tenhunen. Energy efficient signaling in deep submicron CMOS technology. *Special Issue on Timing Analysis and Optimization for Deep Sub-Micron ICs, VLSI Design Journal*, 15(3):563–586, 2002.

[80] S. H. Choi, B. C. Paul, and K. Roy. Dynamic noise analysis with capacitive and inductive coupling. In *Proc. IEEE Int. Conf. VLSI Design*, pages 65–70, 2002.

[81] G. Servel, D. Deschacht, F. Saliou, J.-L. Mattei, and F. Huret. Inductance effect in crosstalk prediction. *IEEE Transactions on Advanced Packaging*, 25(3):340–346, Aug. 2002.

[82] S. Tuuna, J. Isoaho, and H. Tenhunen. Analytical model for crosstalk and intersymbol interference in point-to-point buses. *IEEE Transactions on Computer-Aided Design of Integrated Circuits and Systems*, 25(7):1400–1411, July 2006.

[83] W. McC. Siebert. *Circuits, Signals and Systems.* Cambridge, MA: The MIT Press, 1986.

[84] Y. I. Ismail and E. G. Friedman. Effects of inductance on the propagation delay and repeater insertion in VLSI circuits. *IEEE Transactions on Very Large Scale Integration (VLSI) Systems*, 8(2):195–206, Apr. 2000.

[85] Y. Eo, W. R. Eisenstadt, J. Y. Jeong, and O.-K. Kwon. A new on-chip interconnect crosstalk model and experimental verification for CMOS VLSI circuit design. *IEEE Transactions on Electron Devices*, 47(1):129–140, Jan. 2000.

[86] W.-Y. Chen, S. K. Gupta, and M. A. Breuer. Analytical models for crosstalk excitation and propagation in VLSI circuits. *IEEE Transactions on Computer-Aided Design of Integrated Circuits and Systems*, 21(10):1117–1131, Oct. 2002.

[87] H. B. Bakoglu. *Circuits, interconnections and packaging for VLSI.* Reading, MA: Addison-Wesley, 1990.

[88] P. Heydari, S. Abbaspour, and M. Pedram. Interconnect energy dissipation in high-speed ULSI circuits. *IEEE Transactions on Circuits and Systems I*, 51(8):1501–1514, Aug. 2004.

[89] A. Djordjevic, M. Bazdar, T. Sarkar, and R. Harrington. *LINPAR for Windows: Matrix parameters for multiconductor transmission lines, software and user's manual, version 2.0.* Artech House, Boston, 1999.

[90] M. Kamon, M. J. Tsuk, and J. K. White. Fasthenry: A multipole-accelerated 3-D inductance extraction program. *IEEE Transactions on Microwave Theory and Techniques*, 42(9):1750–1758, Sep. 1994.

[91] K. T. Tang and E. G. Friedman. Simultaneous switching noise in on-chip cmos power distribution networks. *IEEE Transactions on Very Large Scale Integration (VLSI) Systems*, 10(4):487–493, Aug. 2002.

[92] Y. Eo, W. R. Eisenstadt, J. Y. Jeong, and O.-K. Kwon. New simultaneous switching noise analysis and modeling for high-speed and high-density cmos ic package design. *IEEE Transactions on Advanced Packaging*, 23(2):303–312, May 2000.

[93] S. Tuuna, L.-R. Zheng, J. Isoaho, and H. Tenhunen. Modeling of on-chip bus switching current and its impact on noise in power supply grid. *IEEE Transactions on Very Large Scale Integration (VLSI) Systems*, 16(6):766–770, Jun. 2008.

[94] L.-R. Zheng and H. Tenhunen. Fast modeling of core switching noise on distributed LRC power grid in ULSI circuits. *IEEE Transactions on Advanced Packaging*, 24(3):245–254, Aug. 2001.

[95] M. R. Stan and W. P. Burleson. Bus-invert coding for low-power I/O. *IEEE Transactions on Very Large Scale Integration (VLSI) Systems*, 3(1):49–58, Mar. 1995.

[96] H. Kaul, D. Sylvester, M. A. Anders, and R. K. Krishnamurthy. Design and analysis of spatial encoding circuits for peak power reduction in on-chip buses. *IEEE Transactions on Very Large Scale Integration (VLSI) Systems*, 13(11):1225–1238, Nov. 2005.

[97] C. Raghunandan, K. S. Sainarayanan, and M. B. Srinivas. Bus-encoding technique to reduce delay, power and simultaneous switching noise (SSN) in RLC interconnects. In *Proc. ACM Great Lakes Symp. on VLSI*, pages 371–376, 2007.

[98] B. Victor and K. Keutzer. Bus encoding to prevent crosstalk delay. In *Proc. IEEE Int. Conf. on Computer-Aided Design*, pages 57–63, 2001.

[99] C.-G. Lyuh and T. Kim. Low-power bus encoding with crosstalk delay elimination. *IEE Proceedings Computers and Digital Techniques*, 153(2):93–100, Mar. 2006.

[100] Z. Khan, T. Arslan, and A. T. Erdogan. Low power system on chip bus encoding scheme with crosstalk noise reduction. *IEE Proceedings Computers and Digital Techniques*, 153(2):101–108, Mar. 2006.

[101] E. Macii, M. Poncino, and S. Salerno. Combining wire swapping and spacing for low-power deep-submicron buses. In *Proc. ACM Great Lakes Symp. on VLSI*, pages 198–202, 2003.

[102] J. Zhang and E. G. Friedman. Effect of shield insertion on reducing crosstalk noise between coupled interconnects. In *Proc. Int. Symp. on Circuits and Systems*, pages 529–532, 2004.

[103] M. Mutyam. Selective shielding technique to eliminate crosstalk transitions. *ACM Transactions on Design Automation of Electronic Systems*, 14(3):43:1–43:20, May 2009.

[104] N. Hanchate and N. Ranganathan. Simultaneous interconnect delay and crosstalk noise optimization through gate sizing using game theory. *IEEE Transactions on Computers*, 55(8):1011–1023, Aug. 2006.

[105] K. Hirose and H. Yasuura. A bus delay reduction technique considering crosstalk. In *Proc. Design Automation and Test in Europe*, pages 441–445, 2000.

[106] M. Ghoneima, Y. I. Ismail, M. M. Khellah, J. W. Tschanz, and V. De. Reducing the effective coupling capacitance in buses using threshold voltage adjustment techniques. *IEEE Transactions on Circuits and Systems I*, 53(9):1928–1933, Sept. 2006.

[107] M. Ghoneima and Y. I. Ismail. Utilizing the effect of relative delay on energy dissipation in low-power on-chip buses. *IEEE Transactions on Very Large Scale Integration (VLSI) Systems*, 12(12):1348–1359, Dec. 2004.

[108] Y. M. Lee and K. H. Park. Mesochronous bus for reducing peak I/O power dissipation. *IEE Electronics Letters*, 37(5):278–279, Mar. 2001.

[109] S. Tuuna, J. Isoaho, and H. Tenhunen. Skewing-based method for reduction of functional crosstalk and power supply noise caused by on-chip buses. *IET Computers & Digital Techniques*, in press.

[110] L.-R. Zheng and S. Tuuna. Power distribution modeling and integrity analysis. In R. Nair and D. Bennett, editors, *Power Integrity Analysis and Management for Integrated Circuits*, pages 221–258. Prentice Hall, Boston, MA, 2010.

[111] Y. Ogasahara, M. Hashimoto, and T. Onoye. Measurement and analysis of inductive coupling noise in 90 nm global interconnects. *IEEE Journal of Solid-State Circuits*, 43(3):718–728, Mar. 2008.

[112] Y. Massoud, S. Majors, J. Kawa, T. Bustami, D. MacMillen, and J. White. Managing on-chip inductive effects. *IEEE Transactions on Very Large Scale Integration (VLSI) Systems*, 10(6):789–798, Dec. 2002.

[113] P. Gupta and A. B. Kahng. Wire swizzling to reduce delay uncertainty due to capacitive coupling. In *Proc. Int. Conf. on VLSI Design*, pages 431–436, 2004.

[114] B. Victor and K. Keutzer. Bus encoding to prevent crosstalk delay. In *Proc. Int. Conf. on Computer Aided Design*, pages 57–63, 2001.

[115] M. Lampropoulos, B.M. Al-Hashimi, and P. Rosinger. Minimization of crosstalk noise, delay and power using a modified bus invert technique. In *Proc. Design, Automation and Test in Europe*, pages 1372–1373, 2004.

[116] S.-W. Tu, Y.-W. Chang, and J.-Y. Jou. RLC coupling-aware simulation and on-chip bus encoding for delay reduction. *IEEE Transactions on Computer-Aided Design of Integrated Circuits and Systems*, 25(10):2258–2264, Oct. 2006.

[117] R. R. Rao, H. S. Deogun, D. Blaauw, and D. Sylvester. Bus encoding for total power reduction using a leakage-aware buffer configuration. *IEEE Transactions on Very Large Scale Integration (VLSI) Systems*, 13(12):1376–1383, Dec. 2005.

[118] Y. Cao, P. Gupta, A.B. Kahng, D. Sylvester, and J. Yang. Design sensitivities to variability: extrapolations and assessments in nanometer VLSI. In *Proc. ASIC/SoC Conference*, pages 411–415, 2002.

[119] V. Mehrotra. *Modeling the effects of systematic process variation on circuit performance*. Ph.D. thesis, Massachusetts Institute of Technology, 2001.

[120] A. B. Kahng and K. Samadi. CMP fill synthesis: A survey of recent studies. *IEEE Transactions on Computer-Aided Design of Integrated Circuits and Systems*, 27(1):3–19, Jan. 2008.

[121] P. Yu, S. X. Shi, and D. Z. Pan. True process variation aware optical proximity correction with variational lithography modeling and model calibration. *SPIE Journal of Micro/Nanolithography, MEMS, and MOEMS*, 6(3):1–36, Sept. 2007.

[122] S. Tuuna, E. Nigussie, J. Isoaho, and H. Tenhunen. Analysis of delay variation in encoded on-chip bus signaling under process variation. In *Proc. 21st Int. Conf. on VLSI Design*, pages 228–234, 2008.

[123] M. A. El-Moursy and E. G. Friedman. Shielding effect of on-chip interconnect inductance. *IEEE Transactions on Very Large Scale Integration (VLSI) Systems*, 13(3):396–400, Mar. 2005.

[124] R. Arunachalam, F. Dartu, and L. T. Pileggi. CMOS gate delay models for general RLC loading. In *Proc. Int. Conf. on Computer Design*, pages 224–229, 1997.

[125] N. Delorme, M. Belleville, and J. Chilo. Inductance and capacitance analytic formulas for VLSI interconnects. *IEEE Electronics Letters*, 32(11):996–997, May 1996.

[126] M. E. Dean, T. E. Williams, and D. L. Dill. Efficient self-timing with level-encoded 2-phase dual rail (LEDR). In *Proc. Univ. of California/Santa Cruz Conf. on Advanced Research in VLSI*, pages 55–70, 1991.

[127] W. J. Bainbridge and S. B. Furber. Delay insensitive system-on-chip interconnect using 1-of-4 data encoding. In *Proc. 7th Int. Symp. on Asynchronous Circuits and Systems*, pages 118–126, 2001.

[128] A. Mitra, W. F. McLaughlin, and S. M. Nowick. Efficient asynchronous protocol converters for two-phase delay-insensitive global communication. In *Proc. 13th Int. Symp. on Asynchronous Circuits and Systems*, pages 186–195, 2007.

[129] W. Zhao, F. Liu, K. Agarwal, D. Acharyya, S. R. Nassif, K. J. Nowka, and Y. Cao. Rigorous extraction of process variations for 65-nm CMOS design. *IEEE Transactions on Semiconductor Manufacturing*, 22(1):196–203, Feb. 2009.

[130] W. Zhao and Y. Cao. New generation of predictive technology model for sub-45nm design exploration. In *Proc. Int. Symposium on Quality Electronic Design*, pages 585–590, 2006.

[131] D. Blaauw, K. Chopra, A. Srivastava, and L. Scheffer. Statistical timing analysis: From basic principles to state of the art. *IEEE Transactions on Computer-Aided Design of Integrated Circuits and Systems*, 27(4):589–607, Apr. 2008.

[132] A. Agarwal, D. Blaauw, V. Zolotov, S. Sundareswaran, M. Zhao, K. Gala, and R. Panda. Statistical delay computation considering spatial correlations. In *Proc. Asia and South Pacific Design Automation Conference*, pages 271–276, 2003.

[133] A. Singhee, S. Singhal, and R. A. Rutenbar. Practical, fast Monte Carlo statistical static timing analysis: Why and how. In *Proc. Int. Conf. on Computer-Aided Design*, pages 190–195, 2008.

[134] J. Jaffari and M. Anis. Practical Monte-Carlo based timing yield estimation of digital circuits. In *Proc. Int. Conf. on Design, Automation and Test in Europe*, pages 807–812, 2010.

[135] T. Wang and F. Yuan. A new current-mode incremental signaling scheme with applications to Gb/s parallel links. *IEEE Transactions on Circuits and Systems I*, 54(2):255–267, Feb. 2007.

[136] A. P. Jose, G. Patounakis, and K. L. Shepard. Pulsed current-mode signaling for nearly speed-of-light intrachip communication. *IEEE Journal of Solid-State Circuits*, 41(4):772–780, Apr. 2006.

[137] L. Zhang, J. M. Wilson, R. Bashirullah, L. Luo, J. Xu, and P. D. Franzon. A 32-Gb/s on-chip bus with driver pre-emphasis signaling. *IEEE Transactions on Very Large Scale Integration (VLSI) Systems*, 17(9):1267–1274, Sept. 2009.

[138] E. Nigussie, J. Plosila, S. Tuuna, J. Isoaho, and H. Tenhunen. Energy efficient semi-serial on-chip link through circuit optimizations and integration of signaling techniques. *IEEE Transactions on Very Large Scale Integration (VLSI) Systems*, in press.

[139] P. Heydari, S. Abbaspour, and M. Pedram. Interconnect energy dissipation in high-speed ULSI circuits. *IEEE Transactions on Circuits and Systems I*, 51(8):1501–1514, Aug. 2004.

[140] M. Alioto, G. Palumbo, and M. Poli. Energy consumption in RC tree circuits. *IEEE Transactions on Very Large Scale Integration (VLSI) Systems*, 14(5):452–461, May 2006.

[141] M. Alioto, G. Palumbo, and M. Poli. Analysis and modeling of energy consumption in RLC tree circuits. *IEEE Transactions on Very Large Scale Integration (VLSI) Systems*, 17(2):278–291, Feb. 2009.

[142] W. C. Athas, L. J. Svensson, J. G. Koller, N. Tzartzanis, and E. Y.-C. Chou. Low-power digital systems based on adiabatic-switching principles. *IEEE Transactions on Very Large Scale Integration (VLSI) Systems*, 2(4):398–407, Dec. 1994.

[143] S. Paul, A. M. Schlaffer, and J. A. Nossek. Optimal charging of capacitors. *IEEE Transactions on Circuits and Systems I*, 47(7):1009–1016, July 2000.

[144] K. Sundaresan and N. R. Mahapatra. An analysis of timing violations due to spatially distributed thermal effects in global wires. In *Proc. IEEE/ACM 44th Design Automation Conference*, pages 515–520, 2007.

[145] R. Bashirullah, W. Liu, and R.K. Cavin. Current-mode signaling in deep submicrometer global interconnects. *IEEE Transactions on Very Large Scale Integration (VLSI) Systems*, 11(3):406–417, June 2003.

[146] A.N. Irfansyah, T. Lehmann, and S. Nooshabadi. Energy delay optimization methodology for current-mode signaling for on-chip interconnects. In *Proc. IEEE Integrated Circuit Design and Technology Conf.*, pages 147–150, 2008.

[147] C. Kashyap and B.L. Krauter. A realizable driving point model for on-chip interconnect with inductance. In *Proc. Design Automation Conference*, pages 190–195, 2000.

[148] S. Tuuna, E. Nigussie, J. Isoaho, and H. Tenhunen. Modeling of energy dissipation in RLC current-mode signaling. *IEEE Transactions on Very Large Scale Integration (VLSI) Systems*, in press.

[149] J. A. Dobrowolski. *Microwave Network Design Using the Scattering Matrix*. Artech House, Norwood, MA, 2010.

[150] K. Nose and T. Sakurai. Analysis and future trend of short-circuit power. *IEEE Transactions on Computer-Aided Design of Integrated Circuits and Systems*, 19(9):1023–1030, Sept. 2000.

[151] A. Maheshwari and W. Burleson. Differential current-sensing for on-chip interconnects. *IEEE Transactions on Very Large Scale Integration (VLSI) Systems*, 12(12):1321–1329, Dec. 2004.

[152] G. Moon, M.E. Zaghloul, and R.W. Newcomb. An enhancement-mode MOS voltage-controlled linear resistor with large dynamic range. *IEEE Transactions on Circuits and Systems*, 37(10):1284–1288, Oct. 1990.

[153] R. Weerasekera, M. Grange, D. Pamunuwa, and H. Tenhunen. On signalling over through-silicon via (TSV) interconnects in 3-D integrated circuits. In *Proc. Conf. on Design, Automation and Test in Europe*, pages 1325–1328, 2010.

[154] K. Salah, H. Ragai, Y. Ismail, and A. E. Rouby. Equivalent lumped element models for various n-port through silicon vias networks. In *Proc. Asia and South Pacific Design Automation Conference*, pages 176–183, 2011.

[155] P. J. Burke. An RF circuit model for carbon nanotubes. *IEEE Transactions on Nanotechnology*, 2(1):55–58, Mar. 2003.

[156] A. Raychowdhury and K. Roy. Modeling of metallic carbon-nanotube interconnects for circuit simulations and a comparison with Cu interconnects for scaled technologies. *IEEE Transactions on Computer-Aided Design of Integrated Circuits and Systems*, 25(1):58–65, Jan. 2006.

Appendix A

Coefficients for Equations in Chapter 3

In the equations below, s_1, s_2 and s_3 are the roots of the third degree equation $s^3 + s^2 \frac{R_s R C_1 + L}{R_s L C_1} + s(\frac{1}{LC_1} + \frac{1}{LC_2} + \frac{R}{R_s L C_1}) + \frac{1}{R_s L C_1 C_2}$. It has been assumed in the derivation of the inverse Laplace transform that all roots are distinct.

Coefficients for Equation (3.12):

$$
\begin{aligned}
a_1 &= I_0 - \alpha_2 - \frac{\alpha_5}{\alpha_6} + \frac{\alpha_3(s_3 - s_1)}{s_2 - s_1} - \alpha_3 \\
a_2 &= \alpha_2 - \frac{\alpha_3(s_3 - s_1)}{s_2 - s_1} \\
a_3 &= \frac{\alpha_5}{\alpha_6} + \alpha_3 \\
a_4 &= \frac{-k}{R_s L C_1 s_1 s_2 s_3} \\
a_5 &= \frac{-a_4 s_3 - \alpha_1(s_3 - s_2)}{s_3 - s_1} \\
a_6 &= \alpha_1 \\
a_7 &= -a_4 + \frac{a_4 s_3 + \alpha_1(s_3 - s_2)}{s_3 - s_1} - \alpha_1 \\
a_8 &= -a_4 \\
a_9 &= \frac{a_4 s_3 - a_{10}(s_3 - s_2)}{s_3 - s_1} \\
a_{10} &= \frac{-a_4}{\alpha_4}(s_2 s_3 + s_1 s_3 - \frac{s_2 s_3^2}{s_3 - s_1} + \frac{s_1 s_2 s_3}{s_3 - s_1}) \\
a_{11} &= a_4 - a_9 - a_{10}
\end{aligned}
\tag{A.1}
$$

where

$$
\begin{aligned}
\alpha_1 &= \frac{a_4}{\alpha_4}\left(s_2 s_3 + s_1 s_3 - \frac{s_2 s_3^2}{s_3 - s_1} + \frac{s_1 s_2 s_3}{s_3 - s_1}\right) \\
\alpha_2 &= \frac{\frac{V_{02}}{L} + I_0(s_3 + s_2) - \frac{\alpha_5}{\alpha_6}(s_3 - s_1) - \frac{V_0}{L} + \frac{I_0}{R_s C_1}}{s_2 - s_1} \\
\alpha_3 &= \left(\frac{R_s L C_1}{v_i}\left(\frac{(s_3 - s_1)(s_2 s_3 - s_1 s_3)}{s_2 - s_1} - s_2 s_3 + s_1 s_2\right)\right)^{-1} \\
\alpha_4 &= \frac{s_2 s_3 (s_3 - s_2)}{s_3 - s_1} - \frac{s_1 s_2 (s_3 - s_2)}{s_3 - s_1} - s_1 s_3 + s_1 s_2 \\
\alpha_5 &= \frac{-V_0}{R_s L C_1} - I_0 s_2 s_3 + \frac{V_{02}(s_2 s_3 - s_1 s_3)}{L(s_2 - s_1)} \\
&\quad + \frac{I_0(s_3 + s_2)(s_2 s_3 - s_1 s_3)}{s_2 - s_1} - \frac{V_0(s_2 s_3 - s_1 s_3)}{L(s_2 - s_1)} \\
&\quad + \frac{I_0(s_2 s_3 - s_1 s_3)}{R_s C_1 (s_2 - s_1)} \\
\alpha_6 &= \frac{(s_3 - s_1)(s_2 s_3 - s_1 s_3)}{s_2 - s_1} - s_2 s_3 + s_1 s_2
\end{aligned}
\tag{A.2}
$$

Coefficients for Equation (3.13):

$$
\begin{aligned}
b_1 &= \beta_4 - \beta_2 - \frac{\beta_8}{\beta_7} - \frac{\beta_3(s_1 s_3 - s_1 s_2)}{s_2 s_3 - s_1 s_2} \\
b_2 &= \beta_2 + \beta_3 \\
b_3 &= \frac{\beta_8}{\beta_7} + \frac{\beta_3(s_1 s_3 - s_1 s_2)}{s_2 s_3 - s_1 s_2} - \beta_3 \\
b_4 &= \frac{-\beta_1(-s_3 + s_2)}{-s_3 + s_1} \\
b_5 &= \beta_1 \\
b_6 &= \frac{\beta_1(-s_3 + s_2)}{-s_3 + s_1} - \beta_1 \\
b_7 &= \frac{\beta_1(-s_3 + s_2)}{-s_3 + s_1} \\
b_8 &= -\beta_1 \\
b_9 &= -\frac{\beta_1(-s_3 + s_2)}{-s_3 + s_1} + \beta_1
\end{aligned}
\tag{A.3}
$$

where

$$
\begin{aligned}
\beta_1 &= \left(\frac{R_s C_1}{k}\left(s_1 s_3 - s_1 s_2 - \frac{(-s_3 + s_2)(s_2 s_3 - s_1 s_2)}{-s_3 + s_1}\right)\right)^{-1} \\
\beta_2 &= \frac{\beta_6 - \beta_4 s_2 s_3 + \beta_8 \beta_7^{-1}(s_2 s_3 - s_1 s_2)}{s_1 s_3 - s_2 s_3} \\
\beta_3 &= \left(\frac{R_s C_1}{v_i}\left(s_2 - s_3 - \frac{(s_1 s_3 - s_1 s_2)(s_1 - s_3)}{s_2 s_3 - s_1 s_2}\right)\right)^{-1} \\
\beta_4 &= V_{02} - V_0 + \frac{I_0 L}{R_s C_1} - \frac{R_s R C_1 I_0 + L I_0}{R_s C_1} \\
\beta_5 &= -\frac{V_0}{R_s C_1} - \frac{I_0}{C_1} - \frac{I_0}{C_2} - \frac{I_0 R}{R_s C_1} \\
\beta_6 &= -\frac{I_0}{R_s C_1 C_2} \\
\beta_7 &= s_3 - s_1 + \frac{(s_2 - s_1) s_2 s_3 - (s_2 - s_1) s_1 s_2}{s_1 s_3 - s_2 s_3} \\
\beta_8 &= \beta_5 + \beta_4(s_3 + s_2) - \frac{(s_2 - s_1)(\beta_6 - \beta_4 s_2 s_3)}{s_1 s_3 - s_2 s_3}
\end{aligned}
\tag{A.4}
$$

Coefficients for Equation (3.14):

$$
\begin{aligned}
&c_1 = \gamma_1 + \gamma_4 \\
&c_2 = -\gamma_1 - \gamma_2 - \gamma_3 - \tfrac{\gamma_4 s_3 + \gamma_5 (s_3 - s_2)}{s_3 - s_1} \\
&c_3 = \gamma_2 + \gamma_5 \\
&c_4 = \gamma_3 - \gamma_4 + \tfrac{\gamma_4 s_3 + \gamma_5 (s_3 - s_2)}{s_3 - s_1} - \gamma_5 \\
&c_5 = \tfrac{c_6 (s_2 s_3 + s_1 s_3 + s_1 s_2)}{s_1 s_2 s_3} \\
&c_6 = \tfrac{-k}{R_s L C_1 C_2 s_1 s_2 s_3} \\
&c_7 = -c_5 - \tfrac{c_6 - c_5 s_1 + c_9 (s_3 - s_1)}{s_1 - s_2} - c_9 \\
&c_8 = \tfrac{c_6 - c_5 s_1 + c_9 (s_3 - s_1)}{s_1 - s_2} \\
&c_9 = (\gamma_6 + \gamma_7)(\tfrac{(s_2 s_3 - s_1 s_3)(s_3 - s_1)}{s_1 - s_2} + s_2 s_3 - s_1 s_2)^{-1} \\
&c_{10} = \tfrac{-c_6 (s_2 s_3 + s_1 s_3 + s_1 s_2)}{s_1 s_2 s_3} \\
&c_{11} = -c_6 \\
&c_{12} = -c_{10} - c_{13} - c_{14} \\
&c_{13} = \tfrac{-c_6 - c_{10} s_1 + c_{14} (s_3 - s_1)}{s_1 - s_2} \\
&c_{14} = (\gamma_8 + \gamma_9)(\tfrac{(s_2 s_3 - s_1 s_3)(s_3 - s_1)}{s_1 - s_2} + s_2 s_3 - s_1 s_2)^{-1}
\end{aligned} \tag{A.5}
$$

where

$$
\begin{aligned}
\gamma_1 &= \tfrac{V_0}{R_s L C_1 C_2 s_1 s_2 s_3} \\
\gamma_2 &= \tfrac{\frac{I_0}{C_2} + \gamma_1 s_1 - \gamma_3 (s_3 - s_1)}{s_2 - s_1} \\
\gamma_3 &= \gamma_{10} \left(s_1 s_2 - s_2 s_3 - \tfrac{(s_3 - s_1)(s_1 s_3 - s_2 s_3)}{s_2 - s_1} \right)^{-1} \\
\gamma_4 &= \tfrac{-v_i}{R_s L C_1 C_2 s_1 s_2 s_3} \\
\gamma_5 &= \tfrac{\gamma_4}{\alpha_4} (s_2 s_3 + s_1 s_3 - \tfrac{s_2 s_3^2}{s_3 - s_1} + \tfrac{s_1 s_2 s_3}{s_3 - s_1}) \\
\gamma_6 &= c_6 \left(-s_3 - s_2 - s_1 - \tfrac{s_2 s_3}{s_1 - s_2} + \tfrac{s_1 s_3}{s_1 - s_2} \right) \\
\gamma_7 &= c_5 \left(s_1 s_3 + s_1 s_2 + \tfrac{s_1 s_2 s_3}{s_1 - s_2} - \tfrac{s_1^2 s_3}{s_1 - s_2} \right) \\
\gamma_8 &= -c_6 \left(-s_3 - s_2 - s_1 - \tfrac{s_2 s_3}{s_1 - s_2} + \tfrac{s_1 s_3}{s_1 - s_2} \right) \\
\gamma_9 &= c_{10} \left(s_1 s_3 + s_1 s_2 + \tfrac{s_1 s_2 s_3}{s_1 - s_2} - \tfrac{s_1^2 s_3}{s_1 - s_2} \right) \\
\gamma_{10} &= \tfrac{V_{02}}{C_2 L} - \tfrac{V_0}{C_2 L} + \tfrac{I_0}{R_s C_1 C_2} - \gamma_1 (s_1 s_3 + s_1 s_2) \\
&\quad - \tfrac{I_0 (s_1 s_3 - s_2 s_3)}{C_2 (s_2 - s_1)} - \tfrac{\gamma_1 s_1 (s_1 s_3 - s_2 s_3)}{s_2 - s_1}
\end{aligned} \tag{A.6}
$$

Appendix B

Coefficients for Equations in Chapter 4

$$n_3 = \frac{1}{7!t_r} r^3 c^4 h^7 + \frac{1}{6!t_r} C_L r^3 c^3 h^6 + \frac{2}{5!t_r} rlc^3 h^5 + \frac{2}{4!t_r} C_L rlc^2 h^4 \tag{B.1}$$

$$n_2 = \frac{1}{5!t_r} r^2 c^3 h^5 + \frac{1}{4!t_r} C_L r^2 c^2 h^4 + \frac{1}{3!t_r} lc^2 h^3 + \frac{1}{2!t_r} C_L lch^2 \tag{B.2}$$

$$n_1 = \frac{1}{3!t_r} rc^2 h^3 + \frac{1}{2!t_r} C_L rch^2 \tag{B.3}$$

$$n_0 = \frac{1}{t_r}(ch + C_L) \tag{B.4}$$

$$\begin{aligned} d_4 = &\frac{1}{8!t_r} r^4 c^4 h^8 + \frac{1}{t_r}(\frac{1}{7!} R_S r^3 c^4 + \frac{1}{7!} C_L r^4 c^3) h^7 \\ &+ (\frac{1}{6!} r^3 c^3 + \frac{1}{t_r}(\frac{3}{6!} r^2 lc^3 + \frac{1}{6!} C_L R_S r^3 c^3)) h^6 \\ &+ (\frac{1}{5!} R_S r^2 c^3 + \frac{1}{5!} C_L r^3 c^2 + \frac{1}{t_r}(\frac{3}{5!} C_L r^2 lc^2 \\ &+ \frac{2}{5!} R_S rlc^3 + \frac{1}{5!} L_S r^2 c^3)) h^5 + (\frac{1}{4!} C_L R_S r^2 c^2 \\ &+ \frac{2}{4!} rlc^2 + \frac{1}{t_r}(\frac{1}{4!} l^2 c^2 + \frac{1}{4!} C_L L_S r^2 c^2 \\ &+ \frac{2}{4!} C_L R_S rlc^2)) h^4 + (\frac{1}{3!} R_S lc^2 + \frac{2}{3!} C_L rlc \\ &+ \frac{1}{3!} L_S rc^2 + \frac{1}{t_r}(\frac{1}{3!} C_L l^2 c + \frac{1}{3!} L_S lc^2)) h^3 \\ &+ (\frac{1}{2!t_r} C_L L_S lc + \frac{1}{2!} C_L R_S lc + \frac{1}{2!} C_L L_S rc) h^2 \end{aligned} \tag{B.5}$$

$$
\begin{aligned}
d_3 = &\frac{1}{6!t_r}r^3c^3h^6 + \frac{1}{t_r}(\frac{1}{5!}R_Sr^2c^3 + \frac{1}{5!}C_Lr^3c^2)h^5 \\
&+ (\frac{1}{4!}r^2c^2 + \frac{1}{t_r}(\frac{2}{4!}rlc^2 + \frac{1}{4!}C_LR_Sr^2c^2))h^4 \\
&+ (\frac{1}{3!}C_Lr^2c + \frac{1}{3!}R_Src^2 + \frac{1}{t_r}(\frac{1}{3!}R_Slc^2 \\
&+ \frac{1}{3!}L_Src^2 + \frac{2}{3!}C_Lrlc))h^3 + (\frac{1}{2!}C_LR_Src \\
&+ \frac{1}{2!}lc + \frac{1}{t_r}(\frac{1}{2!}C_LR_Slc + \frac{1}{2!}C_LL_Src))h^2 \\
&+ (L_Sc + C_Ll)h + C_LL_S
\end{aligned} \tag{B.6}
$$

$$
\begin{aligned}
d_2 = &\frac{1}{4!t_r}r^2c^2h^4 + \frac{1}{t_r}(\frac{1}{3!}R_Src^2 + \frac{1}{3!}C_Lr^2c)h^3 \\
&+ (\frac{1}{2!}rc + \frac{1}{t_r}(\frac{1}{2!}C_LR_Src + \frac{1}{2!}lc))h^2 + (\frac{1}{t_r}(L_Sc \\
&+ C_Ll) + R_Sc + C_Lr)h + \frac{1}{t_r}C_LL_S + C_LR_S
\end{aligned} \tag{B.7}
$$

$$
d_1 = \frac{1}{2!t_r}rch^2 + \frac{1}{t_r}(C_Lr + R_Sc)h + \frac{1}{t_r}C_LR_S + 1 \tag{B.8}
$$

$$
d_0 = \frac{1}{t_r} \tag{B.9}
$$